ABSTRACT

Title of Dissertation: SEISMIC RESILIENCE-BASED DESIGN AND OPTIMIZATION: A DEEP LEARNING AND CYBER-PHYSICAL APPROACH

Jingzhe Wu, Doctor of Philosophy, 2018

Dissertation directed by: Associate Professor, Brian M. Phillips, Department of Civil and Environmental Engineering

With the growing acceptance and better understanding of the importance of uncertainties in seismic design, traditional design approaches with deterministic analysis are being replaced with more reliable approaches within a risk-based context. Recently, resilience has been increasingly studied as a comprehensive metric to assess the ability of a system to withstand and recover from disturbances with large uncertainties. For civil infrastructure systems susceptible to natural hazards, especially earthquakes as considered herein, seismic resilience could provide a measurement integrating both earthquake and post-earthquake performance. For structural engineers, improving infrastructure disaster resilience starts with the design of more resilient structures. This requires a quantitative approach to explicitly guild the design towards better resilience.

However, when attempting to quantify the seismic resilience of a structure, large uncertainties lead to large computational costs associated with risk-based

approaches. Additionally, the accuracy of numerical simulations under wide range of design scenarios is unknown. To address these challenges, this dissertation investigates the role of seismic resilience in structural design. This dissertation starts with a novel seismic protective device to improve structural resilience and follows with the development of a quantitative and efficient design, evaluation, and optimization framework for seismic resilience. This framework proposes metamodeling through deep neural networks for improved efficiency and cyber-physical systems for improved accuracy. Feedforward neural networks are adopted for fragility metamodeling, while online learning long-short term memory neural networks are developed for structural component metamodeling. Real-time hybrid simulation is used for the construction of cyber-physical systems. The proposed framework is demonstrated to have both improved accuracy and significantly reduced computational/experimental cost when compared to existing approaches. The applicability of the framework is illustrated through the optimization of structural systems for improved seismic resilience.

SEISMIC RESILIENCE-BASED DESIGN AND OPTIMIZATION: A DEEP LEARNING AND CYBER-PHYSICAL APPROACH

by

Jingzhe Wu

Dissertation submitted to the Faculty of the Graduate School of the
University of Maryland, College Park, in partial fulfillment
of the requirements for the degree of
Doctor of Philosophy
2018

Advisory Committee:
Professor Brian M. Phillips, Chair
Professor Bilal M. Ayyub
Professor Michelle (Shelby) Bensi
Professor M. Sherif Aggour
Professor Norman M. Wereley

ACKNOWLEDGEMENTS

I would like to send my sincere thanks to my advisor, Professor Brian M. Phillips, for his continuous guidance, advise, and support throughout my PhD studies. His sharing of academic insights and knowledge has inspired me in many ways. Under his guidance, I have improved my academic and professional skills, which will be valuable for my future career development and success. I am honored to have studied under his guidance and will always keep the experience and insights I gained for my future professional development.

I would also like to thank my committee members, Professor Bilal M. Ayyub, Professor Michelle (Shelby) Bensi, Professor M. Sherif Aggour, and Professor Norman M. Wereley, for their insights and advises for my research. All their supports are greatly appreciated.

In addition, I would like to offer my appreciation to my colleagues, Ruiyang Zhang and Ashkan Keivan, for their collaboration and help, as well as inspiring discussions on research. Acknowledgements to my friend Heng Liu, for a lot of interesting and inspiring discussions on deep learning algorithms. I would also like to thank my fellow graduate student Wei-Ting Lu, for his help on my experiments. I would like to extend my thanks to my fellow graduate students and friends, Sami Khan, Michael Whiteman, and Katie Russell, for their support and friendship.

Last but not least, I would like to thank my husband, Tianyi Luo, for his advice, support, understanding, respect and love during all these years, especially during the tough times in both research and life. Moreover, I am grateful to my family

for their understanding and continuous support on all the decisions I have made and always being there for me unconditionally.

TABLE OF CONTENTS

LIST OF TABLES

LIST OF FIGURES

LIST OF ABBREVIATIONS

BMJ	Buckling Mode Jump
BNC	Bayonet Neill–Concelman
BRB	Buckling Restrained Brace
CB	Conventional Brace
CD	Complete Damage
CDM	Central Difference Method
CNN	Convolutional Neural Networks
COC	Clipped-Optimal Control
CPS	Cyber-Physical System
CSM	Capacity Spectrum Method
DBF	Damped Braced Frames
DM	Damage Measure
DOF	Degree of Freedom
DS	Damage State
ED	Extensive Damage
EP	Elasto-Plastic
GA	Genetic Algorithms
GSS	Golden Section Search
HDLRB	High Damping Laminated Rubber Bearings
HIL	Hardware-in-the-Loop
IDA	Incremental Dynamic Analysis
IM	Intensity Measure
LHS	Latin Hypercube Sampling
LSTM	Long-Short Term Memory
LVDT	Linear Variable Differential Transformer
MD	Moderate Damage
MDOF	Multiple Degree of Freedom
MGSS	Modified Golden Section Search
MLE	Maximum Likelihood Estimator

MR	Magnetorheological
MRF	Moment Resisting Frames
NN	Neural Networks
ODBDCO	Over-Driven Back-Driven Clipped-Optimal Controller
PMMA	Poly(methyl methacrylate)
PSO	Particle Swarm Optimization
PWM	Paulse-Width Modulator
RBO	Reliability-based Optimization
RILD	Rate-Independent Linear Damping
RMSE	Root Mean Squared Error
RNN	Recurrent Neural Networks
RTHS	Real-Time Hybrid Simulation
SA	Simulated Annealing
SD	Slight Damage
SDOF	Single Degree of Freedom
SISO	Single-Input Single-Output
SMA	Shape Memory Alloy
VE	Visco-Elastic

CHAPTER 1 INTRODUCTION

1.1 Motivation

Earthquakes continue to expose vulnerabilities in civil structures. Significant loss of lives and property has been observed in past strong earthquake events over the world in the past few decades, such as Northridge earthquake in California (1994), Kobe earthquake in Japan (1995), Central-Western earthquake in India (2001), and Sichuan earthquake in China (2008). As a result, seismic design philosophy has been fundamentally evolving from the conventional strength/serviceability-based methods, to the recent performance/reliability-based methods with the inclusion of the large uncertainties in seismic demand/capacity of the structure within a risk-based context (Ghobarah 2001, Wen 2001). Under the performance/reliability-based design philosophy, structural design is able to integrate the consideration of seismic hazard uncertainties and seismic losses due to damages, while producing design with acceptable risk.

The consequences of structural and nonstructural damage due to earthquakes extend beyond the immediate event to the post-disaster recovery. Recently, the concept of resilience has drawn great attention in the design, assessment, maintenance, and rehabilitation of structures and infrastructure systems. Resilience is a broad multidimensional concept that was first introduced to ecology in 1973 (Holling 1973) and has extensively evolved in many engineering branches now (McAslan 2010, Gilbert 2016). Resilience is broadly defined as the ability of a system to absorb disturbance and recover its functionality. For civil structures and infrastructure systems subjected to seismic risks, seismic resilience provides a more

comprehensive approach to consider both the probabilistic seismic damage/losses and the ability to recover after an event.

A major ongoing effort in the research of seismic resilience focuses on infrastructure systems and communities, which requires the integration of multiple dimensions varying from technical and economic to social and organizational aspects. As a result, methods to quantitatively measure and improve the seismic resilience of infrastructure systems and communities still remain a grand challenge. Bruneau, Chang et al. (2003) presented a broad framework to define seismic resilience of communities and attempted to move from a qualitative conceptualization of seismic resilience towards a more comprehensive quantitative measure by integrating resilience properties including robustness, rapidity, resourcefulness, and redundancy to a unified framework. Their framework includes contexts of failure probabilities, failure consequences and recovery time, with four identified dimensions: technical, economic, social, and organizational. Chang and Shinozuka (2004) further refined the quantitative resilience measure with a case study of seismic mitigation of water system.

Resilience is a complex and community-scale concept, with multi-dimensional influencing factors. From structural engineering perspective, the first step to improve community resilience against seismic hazards is to develop more resilient infrastructure components. To achieve this contribution, an adequate quantitative measure of seismic resilience for each physical structure is necessary, especially to guide structural engineers in seismic design. For the seismic resilience of an individual structure, focus can be placed on structural variables and performance metrics. The technical and economic factors have fewer uncertainties at

the structural level. Individual structures with improved seismic resilience can then contribute to more resilient communities.

Since seismic resilience is calculated using loss probabilities, even for a single structure, its quantitative measure requires a considerable amount of rigorous analysis under at least a suite of earthquakes covering the potential frequency and magnitude range that the structure subjected to. This inherently invites challenges in both efficiency and accuracy of the needed seismic analyses. With the development of computational tools and better understanding of structural seismic behaviors, numerical simulation is advantageous for its cost-wise and time-wise efficiency. However, for structural components or systems those are highly nonlinear or not well understood, it can be difficult to develop/calibrate numerical models that capture their seismic behavior with adequate accuracy over the entire earthquake suite. This is especially true for some strongly rate-dependent or nonlinear damping devices, considering the wide range of frequency and magnitude of the earthquakes needed to be included in the analysis to quantify seismic resilience. In this case, experimental testing could provide improved accuracy when assessing structural seismic responses.

To integrate concepts of seismic resilience into seismic structural design, this dissertation first proposes a novel protective device to achieve more seismic-resilient structures. Next, a quantitative seismic resilience evaluation framework is proposed through the integration of cyber-physical systems, leveraging the efficiency of numerical simulation and neural networks and the accuracy of experimental testing. Furthermore, an optimization approach is developed based on the proposed evaluation framework. The resilience quantification and optimization frameworks are accompanied by a series of proof-of-concept studies. This dissertation provides

promising approaches from a structural engineering aspect to improve seismic resilience with demonstrated effectiveness and efficiency.

1.2 Proposed Work

To achieve more seismically resilient structures, effort from structural engineers can be made in two major aspects: mitigation of structural seismic vulnerability and reduction of the time needed for post-earthquake rehabilitation. The seismic vulnerability highly depends on the structural seismic performance, often indicated using metrics such as peak drifts, residual drifts, and peak accelerations. Available seismic loss estimation models, such as HAZUS (MRl 2003), are mainly built upon peak responses instead of residual deformations. However, seismic residual drifts could also contribute to seismic losses by rendering otherwise stable structures unstable, resulting in the complete loss of the structure from an economic view point (Erochko, Christopoulos et al. 2010, Ramirez and Miranda 2012). In this case, the performance-based design criteria provide damage state thresholds on residual drifts, with peak drift thresholds closely aligned with the HAZUS loss estimation model. Therefore, the performance-based damage state definition is used here as supplemental damage state criteria for the HAZUS loss estimation model.

This dissertation first proposes a novel passive seismic control approach targeting both peak and residual drift control for a more seismic resilient braced frame structure. A cost-effective passive damping brace design based on a buckling mode jump (BMJ) mechanism is proposed with damage-free and reusable features to reduce structural seismic response, providing continuous seismic damage control even during aftershocks and reducing post-earthquake repair. The proposed BMJ

bracing system demonstrated comparative reduction in maximum story drift and significant reduction in residual drift under a suite of 20 ground motions corresponding to 10%/50 years hazard level through nonlinear numerical simulation of a three-story steel braced structure, compared to conventional and buckling restrained braces (BRB). This devise has many tunable design parameters that set up an interesting optimization problem for later chapters.

Moving forward to a quantitative seismic resilience-based design, this dissertation proposes an efficient framework for quantitative seismic resilience evaluation. The approach is based on Incremental Dynamic Analysis (IDA) with improvements in simulation accuracy through cyber-physical system (CPS). The CPS is developed using the substructure real-time hybrid simulation (RTHS) technique, also known as hardware-in-the-loop (HIL) testing. The accuracy of seismic resilience evaluations is improved through the integration of physical specimens representing complex structural components. To reduce the number of experiments required, a modified Golden Section Search (MGSS) algorithm is proposed to seek out critical excitation intensities. The proposed seismic resilience evaluation framework is validated for a three-story steel moment frame structure with supplemental control provided by a MR damper. For the cyber-physical evaluation of the structural response, the MR damper is evaluated physically while the remainder of the structure is simulated numerically.

Furthermore, the proposed seismic resilience evaluation framework is adapted for structural design optimization. In traditional IDA analysis, a single structure is evaluated under multiple earthquake ground motions over a range of intensities. If combined with optimization, each candidate design would require new IDA analysis,

a computationally burdensome process. A deep neural network (NN) fragility metamodel is trained to replace the time-consuming IDA/MGSS-IDA process using simulation data sampled with Latin Hypercube Sampling (LHS) technique. Particle swarm optimization (PSO) algorithm is adopted to guide the exploration of candidate designs. The proposed NN based PSO approach, termed as NN-PSO, is verified on the proposed BMJ bracing system with its design variables as the optimization variables. The numerical study on the optimization of 9 design variables of the BMJ bracing system shows the strong capability of the proposed NN-PSO approach to enable seismic resilience optimization with high computational efficiency.

Lastly, the proposed NN-PSO approach is combined with cyber-physical testing to improve accuracy under component-level uncertainties with significantly reduced computational/experimental cost. A component metamodel is developed for critical structural components based on long-short term memory (LSTM) neural networks. This component metamodel is developed through an online learning process using RTHS tests. The physically modeled structural component is evaluated under realistic load and boundary conditions, from which an accurate metamodel can be developed. Only a limited number of experiments are required before sufficient accuracy is achieved, after which the NN-PSO approach can be applied computationally. This whole combined approach using NN-PSO and cyber-physical system through RTHS is termed as CPS-NN-PSO here. The potential of the combined CPS-NN-PSO approach for design optimization based on seismic resilience is demonstrated and validated for the structural retrofit design of a 6-story steel moment resisting frame and damped braced frame (MRF-DBF) building with inter-story isolation and supplemental damping.

Chapter 2 provides a detailed review of related literatures on seismic design philosophies, seismic resilience, cyber-physical system and real-time hybrid simulation, and structural optimization algorithms and deep neural networks.

Chapter 3 presents a passive bracing system based on a unique BMJ mechanism for more seismic resilient steel braced frame structures. The BMJ behavior is studied through finite element quasi-static analysis and an analytical model is derived for parametric study and design guidance. Its effectiveness on reduction of maximum and residual inter-story drift is numerically demonstrated for a qualitatively improved seismic resilience.

Chapter 4 proposed a cyber-physical seismic resilience evaluation framework through integrating RTHS. A MGSS-IDA algorithm is developed to improve IDA efficiency. Through a case study on a 3-story steel moment resisting frame, both numerical simulation and RTHS results are presented to demonstrate the improved efficiency and accuracy of the proposed framework.

Chapter 5 develops a seismic resilience optimization approach based on Chapter 4, NN fragility metamodeling, and PSO. Significant improvement of efficiency is achieved through a trained NN fragility metamodel in replacement of the computationally intensive IDA/MGSS-IDA process for fragility analysis. Both efficiency and accuracy of the proposed NN-PSO approach are demonstrated through a numerical case study on the optimization of the BMJ bracing system proposed in Chapter 3 with 9 design variables, which suggests great potential and broad applicability of the NN-PSO approach for efficient seismic resilience optimization.

Chapter 6 further integrates the NN-PSO approach with CPS through RTHS for improved accuracy under large uncertainties, with significantly reduced

computational/experimental cost using LSTM neural networks. The metamodel using LSTM neural networks is trained for the RTHS physical substructure through an online learning process. The LSTM component metamodel trained with RTHS is then combined with the NN-PSO approach, termed as CPS-NN-PSO approach. The efficiency and applicability of the CPS-NN-PSO approach is validated through a case study on the seismic resilience optimization for the structural retrofit design of a 6-story steel frame building with inter-story isolation.

CHAPTER 2 LITERATURE REVIEW

2.1 Seismic Design Philosophies

Traditional seismic design philosophies can be identified with main emphasis on capacity design under properly factored working/service/lateral loads, aiming at providing safety/serviceability through capacity targets (e.g. stress, strength, deformation, etc.). These philosophies include linear elastic design, limit/plastic/collapse design, serviceability limit states design and strength limit states design (Bertero, Bertero et al. 1996, Bertero 1996). A major limitation of these traditional seismic design philosophies include the lack of consideration on uncertainties, which naturally appears in seismic hazards (i.e. magnitude and frequency content) and structural seismic behavior (i.e. possible damage states). Such uncertainties are inherently carried over to the structural seismic demand/capacity and the resulting seismic loss for multiple damage states. It clearly indicates that the design solution obtained solely from a single deterministic analysis under the traditional capacity design is not fully reliable. With attempts to include the inherent seismic uncertainties, Sawyer (1964) introduced the comprehensive design philosophy through considering the probabilistic loss associated with various failure/limit states under possible disturbance intensities during the service life.

Further, with the recent advances in performance-based design philosophy, seismic design is able to be conducted to achieve explicit performance objectives (i.e. damage/functionality state related to displacement, acceleration, etc.) under considered level of seismic hazard (Ghobarah 2001). The seismic hazard level is commonly considered in terms of return period (i.e. probability of exceedance). In

that way, the inherent uncertainties can be explicitly considered with pre-selected acceptable risk levels. Also, seismic design can be conducted for multi-level design objectives (i.e. acceptable failure probability at specific performance objective under considered hazard level) with performance-based design (Bertero, Bertero et al. 1996, Bertero and Bertero 2000, Bertero and Bertero 2002). Such advantages of performance-based philosophy have led the recent trends in the state of practice and research (Krawinkler 1995, Fajfar 1999, Tassios 1999).

The uncertain nature of seismic hazard and structural seismic responses makes it particularly necessary to setup the seismic design problem in a risk-based context. The performance-based design formulates acceptable seismic risk through design hazard level with acceptable risks. With the well-established performance-based objectives and criteria, further integration of seismic risk can be achieved with reliability-based or risk-based design philosophies. Reliability-based design handles seismic risks through defining reliability index representing safety margin based on explicitly estimated failure probabilities under performance goals (Wen 2001, Phoon, Kulhawy et al. 2003, Zou, Wang et al. 2010). Risk-based design consists of a more straightforward design procedure by iteratively adjust designs to satisfy acceptable risk level, with seismic risks evaluated directly through failure probabilities regarding target performance objectives (Rojas, Foley et al. 2011, Lazar and Dolsek 2012).

However, the above mentioned seismic risk integrated design philosophies only considers failure probabilities of individual structures under potential events that lead to seismic losses. The recently developed seismic resilience concept can be considered as an extension on the base of these risk integrated design philosophies, with additional inclusion on multi-dimensional contexts both under event and after

event, and potential interconnections between infrastructure networks. The details of the seismic resilience concept are reviewed in Section 2.2.

2.2 Seismic Resilience

For civil infrastructures and systems, their resilience to hazards can be defined as the ability of social units to mitigate hazards (including effects of disasters at occurrence and future hazards), and recover to the level of pre-disaster functionality with minimized social disruption (Bruneau, Filiatrault et al. 2006). In the context of seismic hazard, Bruneau, Chang et al. (2003) proposed a conceptual framework to quantitatively measure seismic resilience of communities according to the definition mentioned above. Within their framework, resilience properties including robustness, rapidity, resourcefulness and redundancy can be integrated in four dimensions: technical, economic, social and organizational. A resilient system is then identified with reduced failure probabilities, reduced failure consequences and residue time to recovery (Bruneau and Reinhorn 2006). Although their proposed conceptual framework does not provide a unified resilience metric for different systems, it suggests a quantification of resilience based on quantitative performance criteria of each property.

In agreement with the conceptual framework discussed above, a lot of research has been conducted to refine or adjust it for specific problems of civil systems or infrastructures. Chang and Shinozuka (2004) proposed a refined quantitative seismic resilience metric and demonstrated on the measure of technical and economic dimensions on the case study of the Memphis water system. Cimellaro, Reinhorn et al. (2005) introduces quantification of seismic resilience through loss and

recovery function, with fragility functions and performance limit states considering uncertainties in earthquake intensity measures. Bruneau and Reinhorn (2007) integrated probability functions with fragilities and performance limit states for assessing seismic resilience of acute care facilities. Cimellaro, Reinhorn et al. (2010) further refined the quantification of disaster resilience in a dimensionless normalized term with respect to the area integration of functionality over the control time period. They also adopted nonlinear loss and recovery function that links the quantification of resilience with the fragility analysis and performance limit states. Tirca, Serban et al. (2015) also evaluated seismic resilience upon structural fragilities, and linked the performance-based design criteria with the limit states in the resilience framework. Ayyub (2014) further proposed a more detailed system resilience model under multi-hazard context, with the consideration of different failure types (e.g. brittle, ductile failure, etc.) and recovery conditions (e.g. recover to as good as new, recover to better to old, etc.), and aging effects.

Overall, for seismic resilience, a common graphical representation in the literature is illustrated in Figure 2.1 for a single event at a certain hazard level. By assuming the structure recovers to full functionality after the event, the resilience model adopted here follows the work of Bruneau, Chang et al. (2003) and Cimellaro, Reinhorn et al. (2010), considering single earthquake event. As the figure shows, seismic resilience is defined graphically as the normalized area of functionality $Q(t)$ over the time period from the time of occurrence of earthquake event to the time of recovery ($T_{OE} + T_{RE}$). In addition, the major analyses to measure seismic resilience can be identified as loss analysis and recovery analysis. The index of seismic

resilience R is given in Eq. (2.1), with the dimensionless measure of functionality $Q(t)$ as a function of time t given in Eq. (2.2):

$$R = \int_{T_{OE}}^{T_{OE}+T_{RE}} Q(t)dt \tag{2.1}$$

$$Q(t) = 1 - L(IM, T_{RE})\{H(t - T_{OE}) - H[t - (T_{OE} + T_{RE})]\} \cdot f_{Rec}(t, T_{OE}, T_{RE}) \tag{2.2}$$

where T_{OE} is the time of occurrence of an earthquake event E; T_{RE} is the recovery time from event E; $H(t)$ is Heaviside step function; $L(IM, T_{RE})$ is the loss estimation as a function of earthquake intensity measure IM and recovery time T_{RE}; $f_{Rec}(t, T_{OE}, T_{RE})$ is the recovery function.

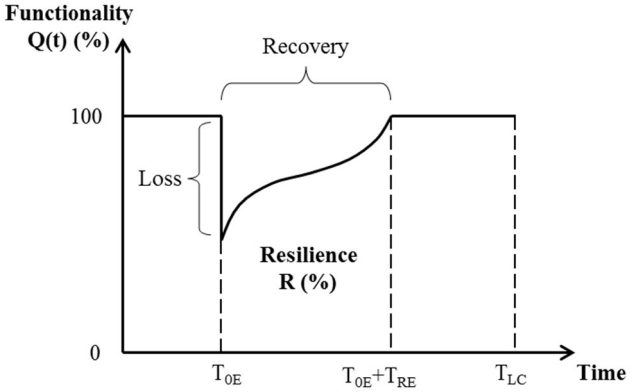

Figure 2.1 Schematic representation of seismic resilience

With the seismic resilience conceptually defined in quantitative terms in literatures, its four dimensions (robustness, rapidity, redundancy and resourcefulness) are identified accordingly (Cimellaro, Reinhorn et al. 2010, Tirca, Serban et al. 2015). As given in Eq. (2.3), robustness against seismic hazards is measured in terms of the residual functionality right after the earthquake event. Note that the residual functionality is obtained in a probabilistic term, with the loss $\tilde{L}$ defined in Eq. (2.3) as a random variable (a function of the mean m_L and standard deviation σ_L). As a result,

improving seismic robustness can be either reducing probabilistic seismic loss or narrowing the variability of seismic loss. As rapidity being identified as the slope of the recovery function curve, Eq. (2.4) gives an average estimation of rapidity over the recovery time period through the estimated loss L and total recovery time T_{RE}. In addition, seismic redundancy is identified as alternative structural lateral resistance elements or systems providing stability following the failure of any single elements. Resourcefulness, referring to the capability to better identify problems, prioritize and manage resources against hazards, is the most difficult dimension to quantify and address due to its large uncertainty from social and organizational aspects.

$$Robustness = R(t = T_{OE}) = 1 - \tilde{L}(m_L, \sigma_L) \tag{2.3}$$

$$Rapidity = \frac{L}{T_{RE}}, (\%/time) \tag{2.4}$$

2.2.1 Loss analysis

As discussed above, one of the major tasks to quantify seismic resilience is the estimation on seismic loss. With agreement in literatures, seismic loss is a probabilistic measure with large uncertainties and can be identified with respect to earthquake intensities and structural damage state probabilities (MRl 2003, Bruneau and Reinhorn 2007, Cimellaro, Reinhorn et al. 2010, Tirca, Serban et al. 2015). The total seismic loss is composed of direct losses that occur instantaneously during the event, and indirect losses with temporal dependencies. The direct and indirect losses can be further divided into economic losses and casualty losses.

Within direct losses, for direct economic losses, detailed categories identified include structural and nonstructural losses, building contents losses, business inventory and interruption losses, etc. For direct economic losses, a probabilistic

representation of the direct economic losses (L_{DE}) under a considered seismic event E (at certain intensity level or hazard level) can be generalized in Eq. (2.5) without considering time dependent depreciation of value as follows:

$$L_{DE}(E) = \sum_{i=1}^{n} r_{c,i} \cdot P_i \left\{ \bigcup_{i=1}^{n} \left(R_i \geq r_{lim,i} \right) \right\} \tag{2.5}$$

where $r_{c,i}$ is the rehabilitation cost ratio (commonly normalized with respect to the full replacement cost) of the infrastructure unit associated with the i damage state, detailed module can be in HAZUS (MRl 2003); P_i is the probability of exceeding a performance limit state i (when it exceeds a performance limit state i, it is considered as in damage state i); R_i is the performance measure of damage state i; $r_{lim,i}$ is the performance limit state criteria. Note that since the direct economic losses are normalized with respect to the building replacement cost, the functionality is accordingly quantified with respect to the building replacement cost here. For direct causality losses, it is commonly identified in terms of the ratio between the number of injured or dead and the total number of occupants (MRl 2003, Cimellaro, Reinhorn et al. 2010). Similarly, it can be tied with performance limit states of different building types with the casualty model provided by HAZUS (2003), and can therefore be considered in probabilistic terms under seismic hazards. It can be integrated into an unified total seismic loss estimation as a weighting factor for direct economic losses(Cimellaro, Reinhorn et al. 2010).

The indirect losses are the most difficult part for seismic loss quantification due to its inherently high complexity and time dependent nature. HAZUS (2003) provides a module for indirect losses estimation as reference, but it has a high demand on the input information complexity. The indirect economic losses, such as

business interruptions, can be even regional or national through business linkages, associated with much more than the damaged infrastructure. The linkages of civil infrastructural systems also contribute to the complexity of indirect economic losses, such as the functional linkage between utility infrastructures, transportation systems and manufacturing facilities. Therefore, the indirect economic losses are influenced by the functionality performance of a unit infrastructure, but not solely related to a single unit. In addition, its time dependent feature also contributes to its complexity in quantification. It surely affected by the recovery time of a unit infrastructure, but is also influenced by other units through their functional linkage. Similarly, the indirect casualty losses also show complexity in influence indicators and time dependency. For example, the indirect casualty loss of a hospital can be affected by the direct seismic damage to the building, and also by the seismic damage to functionally linked utility infrastructures and transportation systems, in terms of both damage extent and recovery time. As a result, the indirect losses need to be considered at the system or community level instead of the unit infrastructure level. However, the influence to indirect losses from the direct seismic damages at the unit infrastructure level should not be neglected and can be at least considered qualitatively.

2.2.2 Recovery analysis

The other major analysis needed for the quantitative measure of seismic resilience is the mathematical representation of the recovery behavior after the earthquake event. As illustrated in Figure 2.1, the resilience index is a time dependent metric that affected by both the recovery time and profile. Although a detailed and realistic seismic recovery model has a high demand on the input of information, there are applicable recovery models based on rational assumptions and simplifications in

literatures. For the estimation of recovery time, HAZUS (2003) provided rough estimation on the median recovery time per building type and damage state based on survey data and some rational assumptions. For the recovery profile, three simplified recovery functions of time t listed below and shown in Figure 2.2 are commonly adopted in literatures (Chang and Shinozuka 2004, Cimellaro, Reinhorn et al. 2010, Tirca, Serban et al. 2015): (1) linear (Eq. 2.6), (2) exponential (Eq. 2.7) and (3) trigonometric (Eq. 2.8).

$$f_{rec}(t) = a\left(\frac{t - T_{OE}}{T_{RE}}\right) + b \tag{2.6}$$

$$f_{rec}(t) = a \cdot \exp[-b\,(t - T_{OE})/T_{RE}] \tag{2.7}$$

$$f_{rec}(t) = a/2\,\{1 + \cos[\pi b\,(t - T_{OE})/T_{RE}]\} \tag{2.8}$$

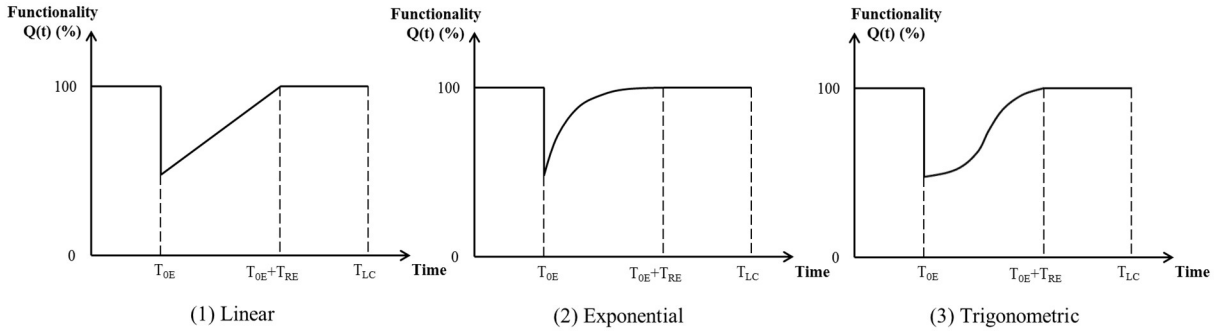

Figure 2.2 Schematic representation of recovery functions: (1) linear; (2) exponential; (3) trigonometric.

The coefficients a and b in these recovery functions can be determined by fitting with realistic recovery data regarding different conditions on the resourcefulness and redundancy of the system. The linear recovery function is the simplest form to use when no information on the post-disaster society response is available. The exponential recovery function can be adopted when the community is well-prepared to respond fast when the event occurs but the rapidity decreases

towards the complete of recovery. The trigonometric recovery function is suitable when the community initially responds slowly to the event due to lack of organization and/or resources but the rapidity grows over time with the incensement in organizational efforts and resources.

2.2.3 Fragility analysis

As discusses in the previous sections, the seismic resilience index is a probability-based metric measured through loss and recovery analysis and can be identified with the probabilities of exceeding different performance limit states. To estimate these probabilities, fragility curves are needed to determine the probability of exceeding considered performance limit states under the considered intensity or hazard level. To construct seismic fragility curve, lognormal distribution is commonly assumed for the conditional failure probability of a structure (Shinozuka, Feng et al. 2000, Porter, Kennedy et al. 2007, Porter 2015, Zentner, Gündel et al. 2017), due to its simple two-parameter formulation and suitability to the conditional distribution of seismic capacities and demands. The common two-parameter formulation of the lognormal cumulative distribution function used to define the seismic fragility function is shown in Eq. (2.9) as follows:

$$P(DS|IM = x) = \Phi\left(\frac{\ln(x/\theta)}{\beta}\right) \tag{2.9}$$

where $P(DS|IM = x)$ is the probability that a ground motion with intensity measure (e.g. peak ground acceleration or spectrum acceleration with a specified period and damping) $IM = x$ will fall in a damage state DS (i.e. exceed the corresponding limit state); $\Phi(\,)$ is the standard normal cumulative distribution function (CDF); θ is the median of the fragility function (the IM level with 50% probability of exceeding the

specific limit state); β is the logarithmic standard deviation. As it shows in this formulation, the determination of the fragility function requires the estimation of the two parameter $\ln(\theta)$ and β, namely, the moments of the lognormal distribution.

The moments of the lognormal fragility function can be analytically estimated through fitting lognormal distribution based on the structural seismic response (capacities and demands) obtained from either simplified nonlinear static analysis or complete nonlinear time history analysis. The nonlinear static analysis, such as capacity spectrum method (CSM) which derives capacity/pushover curve and response spectrum for structural response estimation, is widely adopted for its computational efficiency and ease for practical applications (Shinozuka, Feng et al. 2000, Shinozuka, Feng et al. 2000, MRl 2003). However, nonlinear time history analysis provides more reliable analytical results, especially when the structural response has rate-dependent feature that is not able to be captured by static push over analysis (e.g. structural response controlled by viscous or MR dampers).

The nonlinear time history analysis for fragility function estimation can be conducted in a conceptually straightforward way with Monte Carlo Simulation to converge to a deterministic solution. Although the Monte Carlo approach could approximate the fragility function with high accuracy, it usually requires large-size sampling and can be very computationally expensive when it comes to complex nonlinear structural model and multiple limit states. As a result, the Monte Carlo approach tends to be used with less computationally intensive models (e.g. Porter, Cornell et al. (2005). Here, one widely used approach to achieve fragility function estimation with better computational efficiency and adequate accuracy is Incremental dynamic analysis (IDA), which uses a suite of properly selected ground motions and

repeatedly scaled them to find the seismic capacities and demands associated with different limit states (Vamvatsikos and Cornell 2002, Mander, Dhakal et al. 2007, Tirca, Serban et al. 2015). In this study, the IDA approach is adopted and modified with further improved computational efficiency.

2.3 Cyber-Physical System and Real-Time Hybrid Simulation

Cyber-physical systems (CPS) are integrated physical and engineered systems with monitored, coordinated and controlled operations, coupling the computing in cyber world with the physical world through communications (Rajkumar, Lee et al. 2010). In civil engineering, applications of CPS can be found in hybrid simulation (Shing, Nakashima et al. 1996), structural health monitoring (Hackmann, Guo et al. 2014), model updating (Song and Dyke 2013), etc. Although cyber computing (e.g. numerical simulation) is appealing for its efficiency both in time and cost, applications of CPS could improve the performance of engineering analysis/design by leveraging the efficiency of cyber computing and the realism of physical behavior. CPS could be especially valuable when the behavior of the physical system is highly nonlinear or not well understood which may lead to obstacles or rise concerns in developing/calibrating accurate numerical models for simulation.

In this dissertation, for the seismic fragility analysis which requires analysis under a wide range of earthquake magnitude and frequency content, nonlinear numerical models calibrated to certain ranges or cases (e.g. rate-dependent models for dampers or other seismic control devices) may not be able to capture the actual behavior. In this case, as one of the applications of CPS, real-time hybrid simulation (RTHS), which is essentially a numerical simulation run in parallel with an

experiment and is executed in real time, is adopted here. The numerical and experimental partitions of the system are linked through sensors and actuators to create a loop of action and reaction that simulates the total system. RTHS provides a powerful tool to evaluate such rate-dependent component with combined efficiency from simulation and reliability from experiment (Carrion, Spencer et al. 2009, Zapateiro, Karimi et al. 2010). With the similar objective in improving reliability of seismic fragility analysis, Lin, Li et al. (2012) developed the NEES integrated seismic risk assessment framework with the inclusion of hybrid simulation. RTHS technique is adopted in this dissertation for better accuracy when performing fragility analysis and seismic resilience assessment.

Figure 2.3 shows a schematic representation of the RTHS loop, which consisted of three major components (numerical substructure, interaction loop and experimental substructure). Through the RTHS loop, a structural system can be divided into numerical substructure and experimental substructure, enabling paralleled numerical simulation and experimental testing connected by interface control in real time. The experimental substructure is usually a component that is highly nonlinear or difficult to model numerically, while the numerical substructure is usually the rest of the structural system that is able to be accurately simulated. The interface control synchronizes the changing boundary conditions (e.g. interface displacements or forces) under the input excitation, through controller, actuators and sensors.

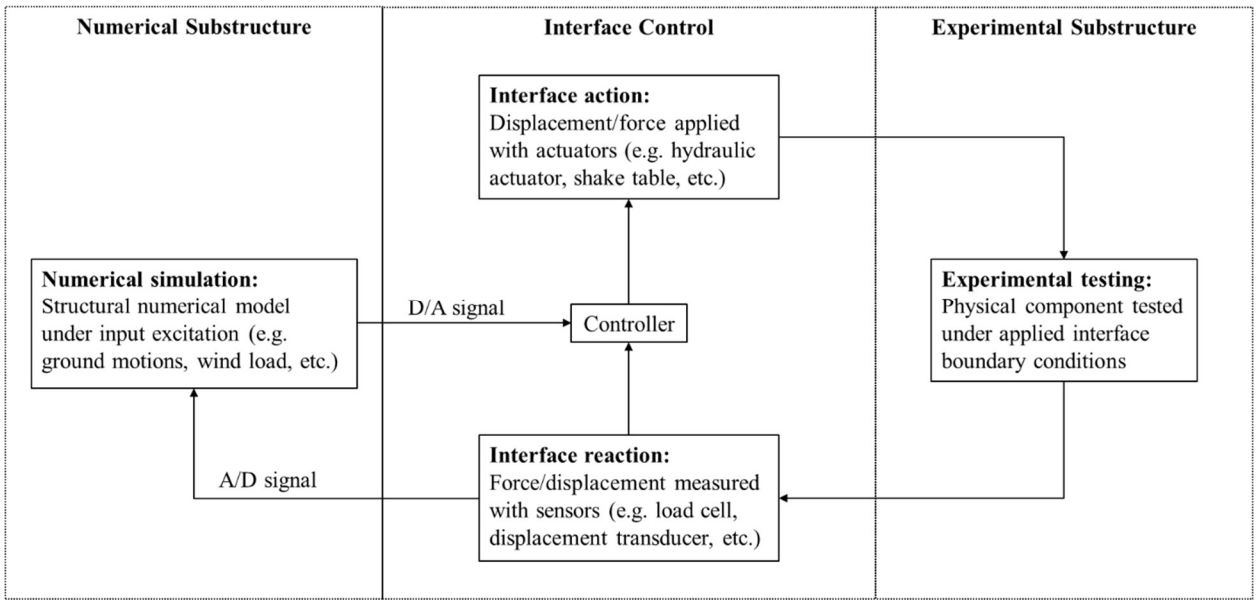

Figure 2.3 Schematic representation of RTHS loop

One of the major challenges of RTHS is the intrinsic demand of small and fixed sampling time step due to its real-time implementation. Since the experimental substructure is tested in real time, all the process for one RTHS loop cycle (i.e. numerical calculations, interface action application, interface reaction measurement and feedforward/feedback control process) need to be performed within a single time step (typically within 10 msec). In addition, the inevitable time delay from numerical calculations and interface data communications, and time lag from actuator dynamics, may cause numerical instability and errors without proper compensation (Horiuchi, Nakagawa et al. 1996). As a result, small numerical integration time step is necessary. Due to the high demand of small and fixed processing time step that is problematic for nonlinear numerical simulation, the numerical substructure is often simulated with linear numerical models with the nonlinearities only in the experimental substructure. However, nonlinear numerical simulation is necessary to capture the damage state information for the fragility analysis in seismic resilience evaluation. Here, a real-

time 2D platform for dynamic analysis of nonlinear steel frames under earthquake excitations (Castaneda Aguilar 2012, Castaneda, Gao et al. 2013) is adopted to enable the seismic fragility analysis within RTHS framework.

2.4 Structural Optimization for Automated Design

With the great improvement on computational power, considerable efforts on developing structural optimization techniques has been conducted throughout the past decades. Structural optimization techniques provide powerful tools in guiding structural design under an objective of interest. It enables an automated design process with optimal criteria and mathematical programming, which is especially valuable for complex design problems with discrete design variables. Automated design with optimization techniques has been of great interest for various structural design problems over decades (Vanderplaats and Sugimoto 1986, Chung, Meyer et al. 1990, Fragiadakis and Papadrakakis 2008, Sinković, Brozovič et al. 2016). The common structural optimization objective is to achieve a design optimum considering both structural performance (e.g. strength, deformation, etc.) and cost, which generally requires compromises in between. Early structural optimization started with optimizing size, shape, and topology of structural members or layout to reach an objective on least material weight and therefore minimized cost under design constraints (e.g. stress, strain, displacement, etc.) (Rozvany 1972, Prager and Rozvany 1977, Bendsøe and Kikuchi 1988). Later, the development of performance-based design initialized the exploration on structural optimization targeting multi-objective criteria optimal design under the inherent uncertainties of design scenarios (i.e. uncertain dynamic loads), which led to a lot of studies on the reliability-based

optimization (RBO) methodology (Enevoldsen and Sørensen 1994, Gasser and Schuëller 1997, Ganzerli, Pantelides et al. 2000, Aoues and Chateauneuf 2010, Valdebenito and Schuëller 2010). The recently developed seismic resilience concept shares the same inclusion of uncertainties with the reliability concept through their risk-based formulation. In addition, the formulation of seismic resilience naturally lumps the cost considerations in some extent, through both seismic loss and recovery time and profile. Some recent studies have attempted to use seismic resilience as an optimization objective for the rehabilitation of bridges (Frangopol and Bocchini 2011, Chandrasekaran and Banerjee 2015). In this dissertation, seismic resilience is applied as the objective of the optimization of seismic protective systems.

Optimization problems can be categorized into deterministic and non-deterministic. For deterministic problems which can be formulated with continuous variables or properties, gradient-based algorithms (e.g. linear and nonlinear programming) are generally used for the efficiency to converge to the global or approximately global optimal solution with pre-defined initial starting values of variables (Andradóttir 1998, Lin, Tsai et al. 2012). For non-deterministic problems that are generally associated with complex systems or discrete variables, heuristic algorithms are favored for their stochastic features, such as simulated annealing (SA), genetic algorithms (GA), particle swarm optimization (PSO), etc. (Saka 2007). Comparing to deterministic approaches, heuristic methods use probabilistic transition rules instead of deterministic ones (e.g. gradient-based search) to converge to the optimal solution in search space and therefore can be applied to complex non-deterministic problems without differentiable continuous variables. In addition, their

search starts with arbitrary initial conditions, avoiding the sensitivity to initial values and allowing possibilities to discover non-intuitive solutions.

The optimization on seismic resilience studied in this dissertation is a complex non-deterministic problem. Therefore, heuristic algorithms are the major considered options here. A limitation of the heuristic algorithms is that the their searched solution is not the rigorously demonstrated optimal solution but the approximation of the optimal solution in the defined search space, due to the discrete and complex nature of non-deterministic problems. However, heuristic approaches are robust and effective in finding solutions to non-deterministic problems, especially for complex problems with multiple discrete variables. In this dissertation, the converged solutions from heuristic algorithms are referred as the optimal solution. The base methodologies adopted for the optimization problem in this dissertation are reviewed in the following subsections.

2.4.1 Golden section search

The IDA approach adopted in this dissertation for seismic fragility analysis uses fixed increments of ground motion intensity between a predefined minimum and maximum. After evaluating the structure's response at each intensity, the threshold intensity to reach a particular damage state will be known. Based on the overall monotonic global trend of IDA curve, the golden section search (GSS) method is adopted herein to replace the enumeration over all intensities. The GSS is selected due to its simplicity and modified for the specific application to develop more efficient IDA process. GSS is a deterministic and non-stochastic algorithm for finding the minimum of an unconstrained objective function within a one-dimensional search

space with optimal solution known to exist (Vanderplaats and Sugimoto 1986). It successively narrows the search space by the golden ratio (Luenberger and Ye 1984) until the pre-defined convergence criteria (e.g. a tolerance on the reduction in search space) is met.

Figure 2.4 illustrates the GSS search space with intermediate evaluation points at an iteration step i. The search space at iteration i is $[a_i, b_i]$, with two intermediate evaluation points $x_{1,i}$ and $x_{2,i}$ defined with the golden ratio φ as given in Eq. (2.10). Such golden section division ensures that $L/L_2 = L_2/L_1$ as Figure 2.4 shows. By defining objective function as the error to searching target and assuming unimodal objective function within the search space, objective function value can be evaluated at $x_{1,i}$ and $x_{2,i}$. The one with smaller function value will be updated as the narrowed search space boundary in replacement of a_{i+1} or b_{i+1} for next integration step, and the other one will be one of the intermediate points of next iteration due to the golden section division. Therefore, only one function evaluation is needed at one iteration step, except for the initial step. Note that the optimal solution is always bracketed inside the narrowing search space for a strictly unimodal problem. Although IDA curve has overall monotonic properties, some weaving behavior that interrupt the overall monotonic behavior may appear due to nonlinear behavior of the structural system. Therefore, some modifications are made to the GSS algorithm and are discussed in Chapter 4.

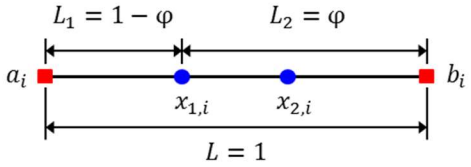

Figure 2.4 GSS search space with golden ratio divided intermediate points at iteration step i

$$\begin{gathered} x_{1,i} = a_i + (b_i - a_i)(1 - \varphi) \\ x_{1,i} = a_i + (b_i - a_i)\varphi \\ \varphi = 0.618 \end{gathered} \tag{2.10}$$

2.4.2 Particle swarm optimization

For the seismic resilience optimization problem associated with complex non-deterministic system behavior and multiple variables, the heuristic algorithm PSO is adopted in this dissertation. The PSO algorithm is inspired by the social behavior of animals (e.g. fish schooling, insect swarming and birds flocking) (Kennedy 2006, Saka 2007). It starts with a group of swarm particles with random positions (i.e. design candidates) in the multi-dimensional search space. By defining the objective function f (e.g. maximum integratory drift, maximum acceleration, etc.), the function value can be evaluated at each particle position and a global best position p_i^g of the locations within the group at the current step i can be determined. Comparing the objective function values of current particle positions x_i^k with that of previous particle positions, the so-far local best position p_i^k for the k-th particle can be determined. At each iteration step, the locations of the group of swarm particles will be updated towards global best position, but still with some extent of random exploration in the searching space, following Eqs. (2.11-12) give below:

$$x_{i+1}^k = x_i^k + v_{i+1}^k \tag{2.11}$$

$$v_{i+1}^k = w v_i^k + c_1 r_1 \left(p_i^k - x_i^k\right) + c_2 r_2 \left(p_i^g - x_i^k\right) \tag{2.12}$$

where x_i^k and v_i^k are the position and velocity of the k-th particle at iteration step i; w is the inertia weight of the particle that used to keep partial previous velocity and

contribute to the extent of exploration (Shi and Eberhart 1998); c_1 and c_2 are empirically defined acceleration coefficients representing the confidence level of the particle in representing the swarm group (Saka 2007); r_1 and r_2 are random numbers between 0 and 1. The positions of the swarm particles will be updated through iterations until the pre-defined convergence criterion (e.g. converging slope of objective function) is met. Constraints can be added to limit the searching space as needed.

The major challenge to employ the stochastic PSO algorithm for seismic resilience optimization problem in this study is the large computational demand, which comes from both the PSO properties (size of the swarm group and iterations needed for convergence) and the huge number of nonlinear time history analysis required by the seismic fragility analysis. Especially for complex systems that may not be accurately described by numerical models, the proposed seismic resilience evaluation and optimization within RTHS framework would provide more realistic and reliable base for optimization, yet numerous amount of substructure experiment needed makes the attempt almost impossible. Therefore, the potential to enable much more efficient and feasible PSO on seismic resilience within the RTHS framework through neural network learning techniques are explored in this dissertation.

2.4.3 Metamodeling and deep neural networks

Facing the challenge of high computational cost associated with optimization for complex systems, a common approach is metamodeling (Chambers and Mount-Campbell 2002). A metamodel is a closed-form function that empirically determined to map the inputs and outputs of a complex system, intended to condense the computationally intensive complex simulation/process. The most straightforward and

common technique to obtain a metamodel is through regression (e.g. least-squares regression) based on the empirical input-output data of the original complex simulation/process. However, regression approaches generally require assumptions on the functional relationship between independent/dependent variables of the problem, which could be problematic or misleading when the underlying functional relationships are unclear/unknown. In this case, neural networks methods are favorable due to its nonparametric feature and high tolerance to the problem complexity (Warner and Misra 1996, Razi and Athappilly 2005).

A neural network (NN) is a parallel and inter-connected network of massive basic computing elements (i.e. artificial neurons) inspired by the neurobiological processing mechanism of human brain (Hajela and Berke 1991, Papadrakakis, Lagaros et al. 1998). A NN is considered deep NN with multiple layers of neurons between the input and output layer. It can provide adaptive tools through learning from data for various applications of function approximation, pattern recognition and classification (Golden 1996, Mehrotra, Mohan et al. 1997). The powerful function approximation and pattern recognition ability of deep neural networks makes them particularly attractive in solving complex problems without clear underlying theory or explicit solutions, engineering design is one of such problems (Adeli and Hung 1994). Many efforts have been conducted on resolving structural engineering challenges with the help of neural network learning, such as rapid analysis for structural design and optimization (Hajela and Berke 1991, Kang and Yoon 1994, Rogers 1994, Papadrakakis, Lagaros et al. 1998, Gholizadeh 2015, Gholizadeh and Mohammadi 2016), and structural performance prediction (Gomes and Awruch 2004, Bucher and Most 2008, Mitropoulou and Papadrakakis 2011, Chatterjee, Sarkar et al. 2017).

A majority of these works are based on the simple yet effective backpropagation (BP) NN training method, which is based on a gradient descent optimization technique and is favorable for function approximation problems (Adeli 2001). Figure 2.5 provides a schematic diagram of a typical deep NN configuration of multi-layer feedforward NN with two hidden layers. As one of the supervised learning algorithm, BP algorithm optimizes the weight matrix $\boldsymbol{W}$ and bias vector $\boldsymbol{b}$ of the links connecting the neuron nodes based on the information from the input training data set, through iteratively minimizing the objective error function in terms of the sum of the squares of the errors between the actual outputs from the training set and the computed output vector from layer transfer function f, weight matrix $\boldsymbol{W}$ and bias vector $\boldsymbol{b}$. The learning process can be specified for particular problems in terms of the input and output data structure, training set division, layer configurations and transfer functions, etc. This dissertation adopts the BP NN training method for the problem on seismic resilience optimization and the detailed discussion is given in Chapter 5.

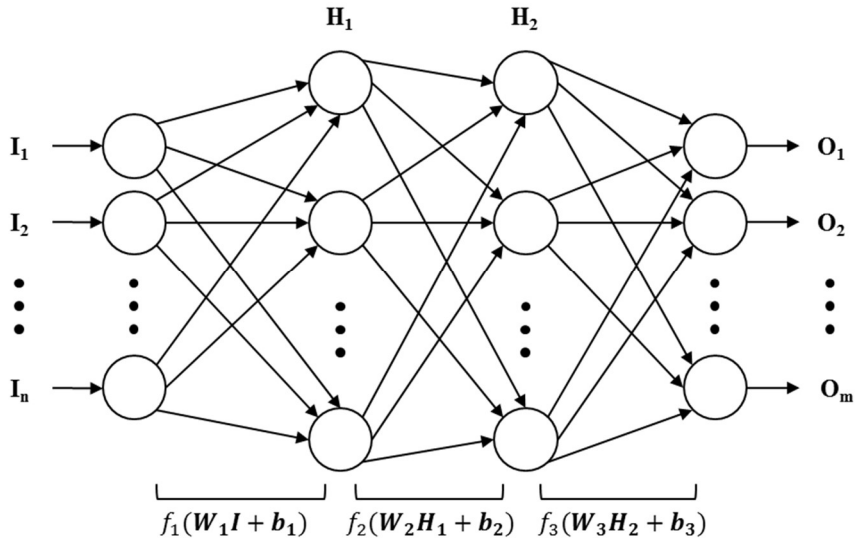

Figure 2.5 A schematic diagram of a typical multi-layer NN configuration with two hidden layers

In addition to the standard multi-layer feedforward NN configuration (Figure 2.5), another type of deep neural network, termed long-short term memory (LSTM) neural network, is also adopted in this dissertation for the specific learning tasks dealing with time history data of the RTHS substructure response (details discussed in Chapter 6). The standard feedforward neural networks rely on the assumption of independence between examples (i.e. data points), and therefore pose a limitation in learning sequential data with time dependency (Lipton, Berkowitz et al. 2015). This limitation can be overcome with recurrent neural networks (RNN), which is a connectionist model improved from feedforward NN with the inclusion of the information from adjacent time steps. As a result, RNN is able to handle sequential data with time dependencies, with the ability to capture dynamics and store information for later use. The structural time history responses can be considered as sequential data with time dependency. Several researches have adopted RNN to model the dynamics of MR damper for damper control using predicted time history response (Chang and Roschke 1998, Wang and Liao 2001, Wang and Liao 2004). However, RNN has difficulties in training and regularization due to its gradient vanishing/exploding problem during the BP process (Hochreiter 1998, Pascanu, Mikolov et al. 2013), and therefore tends to be limited in model size and complexity (Zaremba, Sutskever et al. 2014). This is because that the backpropagation of error exponentially depends on the size of the weights, which would be especially problematic when backpropagating errors across large time delays. The development of LSTM NN resolves this problem by enforcing constant error flow through an

improved recurrent network architecture with internal states of special units (Hochreiter and Schmidhuber 1997).

Figure 2.6 shows a typical LSTM layer architecture with four interacting internal layers. These internal layers are termed as forget gate, input gate, cell state, and output gate. The key component of a LSTM layer is the cell state, which provides the memory during training to store important information for later use. As it illustrated in Figure 2.6, with the memory provided by the cell state, the main flow of the error backpropagation only includes some linear operations and therefore enables a constant error flow and resolves the gradient vanishing/exploding problem during training. The update of cell state during training is controlled by the internal layers with secondary nonlinear networks referred as gates. Each of these internal layers are secondary neural networks with its own weight matrix $\boldsymbol{W}$ and bias vector $\boldsymbol{b}$. The forget gate decides what information to forget from the cell state, through a sigmoid activation layer σ. The resulting number f_t is between 0 and 1, for the pointwise multiplication to update the cell state at the previous time step (C_{t-1}) towards forgetting or keeping respectively. Given in Eq. (2.13), f_t is determined based on the input at current step x_t and the previous hidden state h_{t-1}. The input gate decides what information to store in the memory cell state at the current step, through a sigmoid layer and a tanh activation layer (converts values to be between -1 and 1). The sigmoid layer decides what information to keep for updating cell state with the resulted values i_t following Eq. (2.14), while the tanh layer generate a vector of candidate values $\tilde{C}_t$ following Eq. (2.15). The update of the cell state then follows Eq. (2.16). At final step, the output gate decides what information from the memory cell

state to be included in the output state h_t, through a sigmoid layer and a tanh layer as Eq. (2.17-2.18) presents.

$$f_t = \sigma(W_f[h_{t-1}, x_t] + b_i) \tag{2.13}$$

$$i_t = \sigma(W_i[h_{t-1}, x_t] + b_f) \tag{2.14}$$

$$\tilde{C}_t = tanh(W_C[h_{t-1}, x_t] + b_C) \tag{2.15}$$

$$C_t = f_t \cdot C_{t-1} + i_t \cdot \tilde{C}_t \tag{2.16}$$

$$o_t = \sigma(W_o[h_{t-1}, x_t] + b_o) \tag{2.17}$$

$$h_t = o_t \cdot \tanh(C_t) \tag{2.18}$$

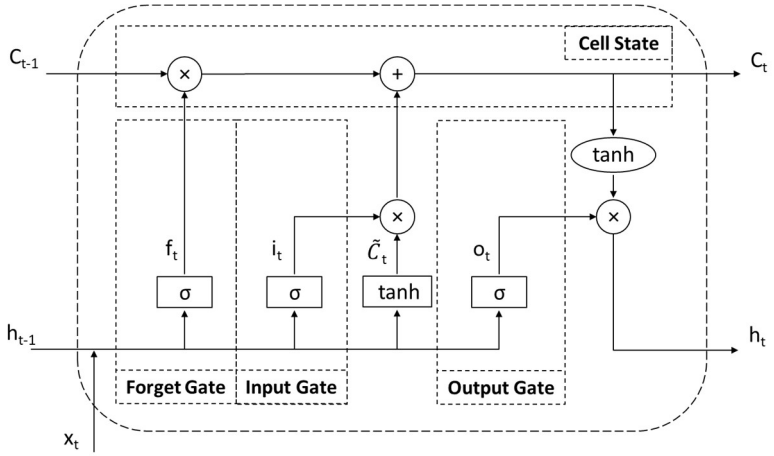

Figure 2.6 A typical LSTM layer architecture

CHAPTER 3 BRACING SYSTEM WITH BUCKLING MODE JUMP MECHANISM

Traditional civil structures with yielding systems can be subjected to damage and permanent deformation through major earthquakes, which may induce substantial seismic loss, including post-earthquake repair costs, business interruptions, casualties, etc. Such seismic vulnerability is closely related with performance-based structural design criteria. In this chapter, a novel capped column with an elastic buckling mode jump (BMJ) mechanism is introduced as an economical passive alternative for obtaining both flag-shaped hysteretic damping and self-centering features in seismic design with reusable feature. A simple analytical model for the mechanism is derived and verified with finite element model simulation results for a variety of capped column geometric configurations. Using the validated analytical model, a parametric study is conducted on the geometric properties to provide design guidance. A practical passive self-centering hysteretic damping brace design is also provided, based on a combination of multiple BMJ mechanisms. The seismic performance of a 3-story frame building under a suite of 20 earthquake ground motions with BMJ brace is compared with a buckling-restrained brace (BRB) frame system as well as a conventional brace (CB) frame system. The results demonstrate the potential of a brace system utilizing BMJ mechanisms to outperform BRB and CB by achieving acceptable inter-story drift response without sustaining residual drift, providing more seismic resilient design in terms of improved seismic robustness, redundancy during aftershocks and rapidity with easier repair.

3.1 Background

Conventional seismic design mitigates seismic response through the structural lateral load resisting system. Inelastic ductile behavior is introduced to provide energy dissipation, such as ductile moment-resisting frames, buckling-restrained bracing (BRB) systems, and ductile shear walls. These elasto-plastic (EP) type of passive control systems may be attractive with lower initial cost compared to utilizing active or semi-active control systems; however, such low post-yield stiffness may induce damage under repeated inelastic deformation and may experience significant residual deformations after a strong earthquake. This leads to a considerable increase in cost of post-earthquake repair or replacement of structural members and concerns of occupancy safety under aftershocks. Therefore, the performance-based seismic design approach has included and emphasized residual structural deformation as a fundamental design parameter (Pampanin, Christopoulos et al. 2003, Christopoulos and Pampanin 2004).

To address the residual deformation issue, significant effort has been taken to develop self-centering seismic resisting systems. Some of the previous research adopted pre-stressed tendons to introduce a self-centering feature to traditional yielding systems, including post-tensioned precast concrete walls (Kurama, Sause et al. 1999), post-tensioned connections for moment-resisting frames (Ricles, Sause et al. 2001, Christopoulos, Filiatrault et al. 2002), pre-stressed reinforced concrete columns for bridges (Mahin, Sakai et al. 2006), bracing systems with pre-tensioned tendons combined with energy dissipation from a friction, yielding , viscous or visco-elastic (VE) type of supplemental dampers (Christopoulos, Tremblay et al. 2008, Tremblay, Lacerte et al. 2008). Structures utilizing rocking type of behavior to

achieve seismic control also ensure self-centering behavior through pre-stressed tendons (Roh and Reinhorn 2010) and also need VE or friction dampers for introducing damping into the system (Azuhata, Midorikawa et al. 2008). Although self-centering behavior can be achieved with pre-stressed elements, such elements only provide the restoring force to achieve self-centering. Supplemental elements are required to provide the stiffness and damping for a complete self-centering structural member with energy dissipation. Thus, the design and detailing of this type of self-centering system is relatively complex. Some researchers have investigated shape memory alloys (SMA) for the purpose of obtaining self-centering behavior combined with energy dissipation for seismic resisting systems. SMA is a type of smart material that is able to return to its pre-deformed shape under the control of temperature or stress, which can provide the source of actuation for self-centering behavior. Dolce et al. (Dolce, Cardone et al. 2000) demonstrated that superelastic SMA-based passive seismic control devices are capable of self-centering behavior as well as considerable energy dissipation, also favorable fatigue resistance, durability, and reliability. Dolce et al. further performed shake table tests for the device installed in a braced frame and observed comparable drift reduction to traditional steel braces with the added benefit of self-centering (Dolce, Cardone et al. 2005). Yet, DesRoches et al. found that the damping potential of SMA in superelastic form is typically less than 7% equivalent viscous damping and excessive stain can degrade the damping and re-centering properties of SMA (DesRoches, McCormick et al. 2004). Later, Zhu and Zhang proposed a self-centering bracing system based on SMA but included friction component for extra damping and demonstrated an appealing seismic response of two braced frames compare to BRB braces (Zhu and Zhang 2007, Zhu and Zhang 2008).

However, main types of SMA contain titanium and therefore costly. The relatively high cost of SMA is still an obstacle to its wide application for the control of large scale civil structures.

The self-centering systems found in the literature possess a flag-shaped hysteresis loop for passive energy dissipation and response reduction. Recently, a new economical source of passive flag-shaped hysteresis damping was proposed through the special two-phase buckling behavior of a press-fit flat-ended cylindrical column (Dong and Lakes 2012, Dong and Lakes 2013). The flag-shaped energy dissipation comes from a shift in the elastic buckling mode of the column. Such unique post-buckling behavior is enabled by the tilting of the press-fit column flat-ends from full-area contact (i.e., primary buckling with fixed-fixed boundary) to edge contact (i.e., secondary buckling with nominal pined-pinned boundary) under compression. This behavior, denoted as buckling mode jump (BMJ) in this dissertation, was found to induce hysteretic damping with a negative slope in stiffness caused by geometric nonlinearity through small-scale experiments (Kalathur, Hoang et al. 2014). Polymethyl methacrylate (PMMA) material was used in these experiments and positive stiffness elements were paired the BMJ columns to achieve stable post-buckling behavior. Kalathur et al. (2014) also proposed a theoretical relationship to predict the second critical buckling load. With the proper design of the geometry of the column, material yielding can be avoided and only elastic buckling will occur within its working range, which brings damage-free and reusable feature. The mechanism was demonstrated for small-scale mechanical applications under very small deformations.

The combined damping and damage-free features of the BMJ mechanism are attractive for passive seismic design. However, significant developments are required to extend the benefits of the BMJ mechanism for civil structural applications. Large-scale devices capable of undergoing large deformation without yielding are needed to be compatible with the expected forces and displacements under seismic loads. Furthermore, an analytical study of the post-buckling behavior (after secondary buckling) and unloading behavior is needed for design and response simulation.

3.2 BMJ Mechanism of Capped Column

Moving away from the cylinder configuration investigated in (Dong and Lakes 2012, Dong and Lakes 2013, Kalathur, Hoang et al. 2014), a configuration consisted of a rectangular cross-section column with a relatively deep depth and end caps is proposed to achieve larger restoring forces, a larger flag-shaped loop, larger deformations without material yielding, and improved stability for applications in large-scale civil structures. A schematic representation of the column with two end caps is shown in Figure 3.1. A shift in the central line of capped column is introduced as an initial eccentricity e_0 to trigger the buckling and control the direction of column deflection under axial load. The material of the end caps and the column can be different; i.e., a harder material can be used for the end caps to resist indentation under concentrated stresses during BMJ behavior. The tapered connection between end cap and column body is also designed to reduce stress concentrations. The depth d is designed to be larger than the column width b_c to ensure a weak axis about the y-axis and that the buckling occurs in the x-z plane. As a result, the buckling behavior

of the proposed capped column can be considered as a 2D problem in the *x-z* plane of Figure 3.1.

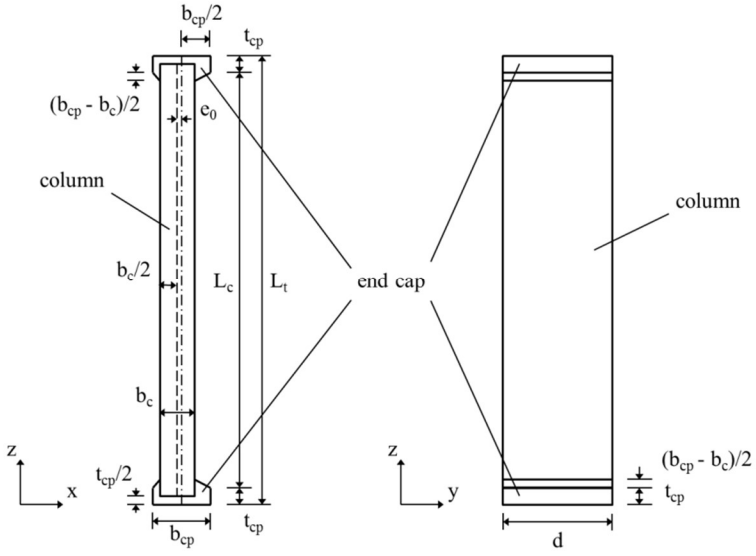

Figure 3.1 Schematic configuration of a capped column

3.2.1 BMJ behavior of capped column

To study the BMJ behavior of the proposed capped column, an example capped column is analyzed through numerical simulation. The geometric properties are summarized in Table 3.1. Quasi-static analysis with finite element program ANSYS Workbench 15.0 (ANSYS) is adopted in this study. Since buckling only occurs about the weak axis, the simulation is performed in 2D with plane stress elements. The material of the end caps and the column is assigned with structural steel and PMMA respectively and only linear elastic material constitutive law is used, as the BMJ behavior is geometrically controlled in elastic buckling behavior. The properties of the materials are given in Table 3.2, which shows that PMMA ensures a large modulus of resilience ($U_r = \sigma_y^2/(2E)$) compared to steel for larger elastic deformation capacity of the column, while structural steel guarantees a large

indentation hardness compared to PMMA for protection of the end cap from wear. Furthermore, the larger modulus and of end caps compared to column enables the end caps to behave nominally as rigid bodies. The PMMA also has lower self-weight compared to many civil engineering materials, which may introduce less additional weight to the structure it applied to and induce less initial deformation due to self-weight. To capture the BMJ phenomenon from the change of contact condition of the end cap surface under axial compression, the connections between the surface of end caps and the loading blocks are modeled as rough contacts. This assumption allows for the separation of the two contact surfaces in normal direction but no sliding in transverse direction. A pre-strain of 0.1% is applied to the capped column by the loading blocks to clamp the capped column in place. The pre-strain also brings the capped column slightly closer to its primary buckling load. For simplicity, the connections between end caps and column are modeled as bonded. The mesh size is controlled to be 5mm for the current geometry scale. The quasi-static analysis is analyzed using displacement control to capture one full loading-unloading cycle.

Table 3.1 Geometric properties of the sample capped column

L_t (m)	L_c (m)	b_c (mm)	b_{cp} (mm)	t_{cp} (mm)	d (mm)	e_0 (mm)
1	0.98	50	60	10	150	0.7

Table 3.2 Material properties of the capped column

Component	Material	E (MPa)	σ_y (MPa)	U_r (MPa)	ρ (g/cm^3)	Indentation hardness (MPa)
Column	PMMA	3100	120	2.32	1.19	170 – 190
End cap	Structural steel	200000	250	0.16	7.85	370 – 2070

The results (Figure 3.2 and 3) from the simulation suggest that the BMJ behavior through change of end contact condition is well captured in the quasi-static finite element analysis (the loading block is hidden in the full window for better view of the capped column deformation, but is presented in the zoom-in window for clear observation of the change of boundary condition). From Figure 3.2, the deforming behavior during a full loading-unloading cycle can be overall classified into: pre-buckling phase, post-primary-buckling phase in fixed-fixed mode, and post-secondary-buckling phase in pinned-pinned mode. The column maintains the initial shape in the pre-buckling phase (Figure 3.2 (a)), while for the post-buckling phases, it holds a fixed-fixed buckled shape before the tilting of end occurs and the capped column jumps into a pinned-pinned buckled shape. During the jump, the end cap and loading block contact suddenly changes from surface-to-surface to edge-to-surface. To clarify the condition for the onset of the jump in boundary condition, the maximum lateral sway of the capped column, which is located at the mid-span of the column, is plotted in Figure 3.3 for the entire loading-unloading cycle (the path of the loop is indicated with arrows along the path). The trigger point of BMJ is highlighted at (X: -14.1 mm, Y: -55.31 mm) in Figure 3.3, which indicates that the change of contact condition occurs approximately when the mid-span lateral sway (55.31 mm) just exceeds the distance between the column central line and the edge of the end cap ($b_{cp}/2 - e_0 + b_c/2 = 54.3$ mm). This BMJ trigger condition represents the point that the extreme fiber of the column at mid-span deflects beyond the edge of the end caps along *y*-axis as it shown in Figure 3.2 (b). This implies that the onset of BMJ from fixed-fixed mode to pinned-pinned mode, which related to the energy dissipation per cycle, can be controlled by adjusting the width of the end caps.

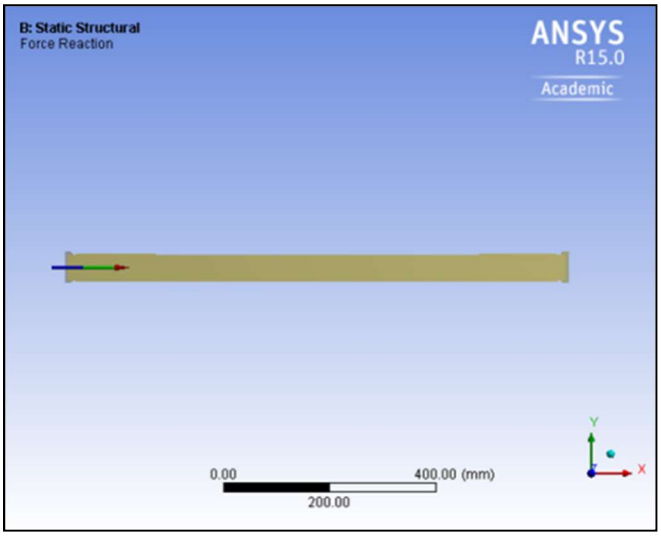
B: Static Structural
Force Reaction
ANSYS
R15.0
Academic
0.00
400.00 (mm)
200.00
Y
X

(a)

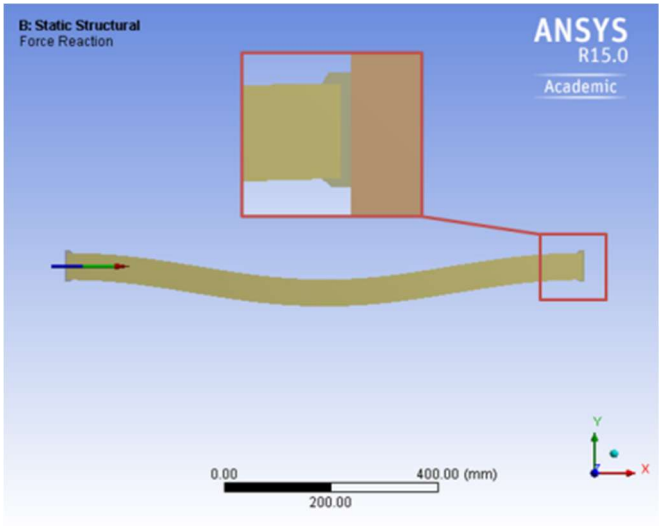
B: Static Structural
Force Reaction
ANSYS
R15.0
Academic
0.00
400.00 (mm)
200.00
Y
X

(b)

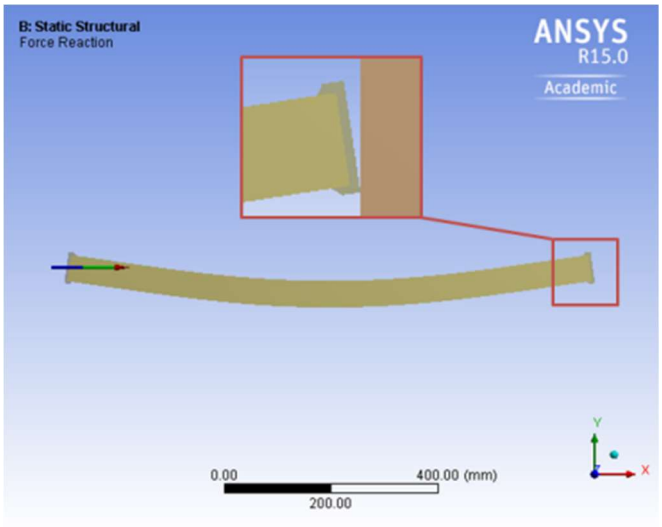
B: Static Structural
Force Reaction
ANSYS
R15.0
Academic
0.00
400.00 (mm)
200.00
Y
X

(c)

Figure 3.2 Deformed shape of the sample capped column at: (a) pre-buckling phase; (b) post-primary-buckling phase (fixed-fixed mode); (c) post-secondary-buckling phase (pinned-pinned mode).

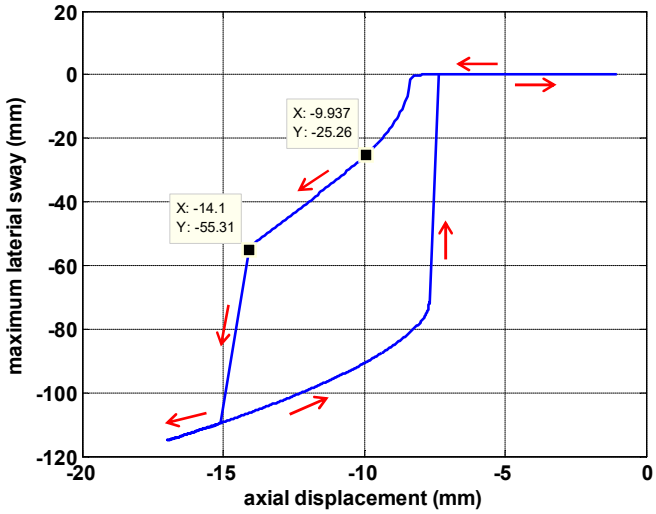

Figure 3.3 Axial displacement vs. mid-span lateral sway of the sample capped column

Figure 3.4 shows the axial force-displacement and extreme fiber stress-displacement behavior of the sample capped column under compression (the path of the loop is indicated with arrows along the path). The axial force-displacement relationship in Figure 3.4 (a) clearly shows a flag-shaped hysteresis loop. The energy dissipation results from the switch between the two different buckling modes. Looking at the post-primary-buckling region, two phases are present (path 2-3 and 3-4 in Figure 3.4 (a)), separating the post-primary-buckling phase into a stable and an unstable path, which is discussed further in Section 3.2.2. Considering the data point (X: -9.937 mm, Y: -25.26 mm) in Figure 3.3 and Point 3 (X: -9.937 mm, Y: -199.1 kN) in Figure 3.4(a), an assumption for the condition of transition Point 3 (post-primary-buckling change from stable to unstable path) can be made: the mid-span

lateral sway (25.26 mm in Figure 3.3) approximately exceeds half of the column width (25 mm), which means that internal axial force at the mid-span of the column extends beyond the section at the end of the column (not including caps). The assumptions on transition points are verified extensively in Section 3.2.3. The complete BMJ behavior of the capped column can be summarized in 6 phases based on Figure 3.4 (a) as follows:

(1) 1-2: pre-buckling linear phase;

(2) 2-3: post-primary-buckling fixed-fixed mode stable phase;

(3) 3-4: post-primary-buckling fixed-fixed mode unstable phase;

(4) 4-7: forward mode jump phase (fixed-fixed to pinned-pinned);

(5) 5-6: post-secondary-buckling pinned-pinned mode phase;

(6) 6-8: backward mode jump phase (pinned-pinned to fixed-fixed).

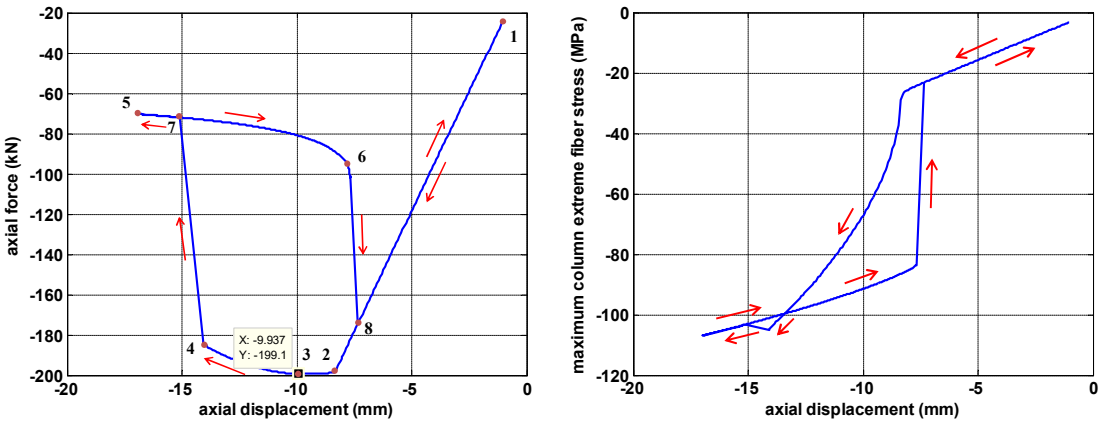

(a) (b)

Figure 3.4 Axial force-displacement and extreme fiber stress-displacement behavior of the sample capped column

During BMJ behavior, the maximum stress in the capped column must be monitored to ensure elastic material behavior and therefore a reusable feature can be

obtained. The BMJ mechanism is intended to supply elastic-only buckling to maintain the benefits of damage-free self-centering and hysteretic damping. Thus, the energy dissipation is generated from the geometric nonlinearity and the material yielding should be avoided, especially in the column itself. The maximum extreme fiber stress in the column is considered as a metric for maintaining elastic material behavior. The extreme fiber stress can be controlled through the design of the geometry of the capped column, which is discussed in the parametric study of Section 3.3. For the sample capped column, the column extreme fiber stress remains below the material yield strength ($\sigma_y = 120$ MPa) in the full loading-unloading cycle (Figure 3.4 (b)).

3.2.2 2D BMJ analytical model

From the numerical simulation of Section 3.2.1, the BMJ behavior is observed to be sensitive to the geometric properties of the capped column. Informed by the numerical simulations, a 2D analytical model is proposed to clarify the sensitivity of the BMJ behavior to geometric parameters, serve as a design aide, and supplement more complex finite element modeling for the simulation of structures under earthquake loading. The analytical model is derived corresponding to the 6 phases listed in Section 3.2.1 and is illustrated as follows:

(1) Pre-buckling linear phase

This phase follows the linear axial behavior of the column with no lateral sway. The equations for predicting axial force (P_1) and stress (σ_1) from axial displacement (d_1) in the pre-buckling linear phase (1) are:

$$P_1 = \frac{E_c A_c d_1}{L_c} \tag{3.1}$$

$$\sigma_1 = \frac{P_1}{A_c} \tag{3.2}$$

where E_c is the elastic modulus of the column and A_c is the cross-section area of the column (without end caps).

(2) Post-primary-buckling fixed-fixed mode stable phase

This phase starts from the initial elastic buckling of the column with fixed-fixed boundary conditions, which can be predicted by (Timoshenko and Gere 1961, Kalathur, Hoang et al. 2014):

$$P_{cr1} = \frac{\pi^2 E_c I_c}{L^2} \tag{3.3}$$

where I_c is the moment of inertia of the column section, $L = 0.5L_c$, and the axial displacement can be calculated using $d_{cr1} = P_{cr1}L_c/(E_c A_c)$. Based on symmetry, half of the column as shown in Figure 3.5 is used to represent the total column behavior. The rotational spring is considered to have infinite stiffness (no rotation) in this phase. The stable fixed-fixed mode post buckling behavior can then be solved with (Budiansky 1973, Kalathur, Hoang et al. 2014):

$$v_2(z) = \frac{v_{max}}{2}(1 - \cos(\frac{\pi z}{L})) \tag{3.4}$$

$$P_2 = P_{cr1}(1 + \frac{\pi^2(\frac{v_{max}}{2})^2}{8L^2}) \tag{3.5}$$

$$d_2 = 2\int_0^L \frac{1}{2}(\frac{dv_2}{dz})^2 dz + 2\frac{P_2 L}{E_c A_c} \tag{3.6}$$

$$\sigma_2 = \frac{E_c I_c \frac{d^2 v_2}{dz^2}\Big|_{z=0} \frac{b_c}{2}}{I_c} + \frac{P_2}{A_c} \tag{3.7}$$

where v_2 is the deflection function for BMJ Phase 2 of the half column shown in Figure 3.5, z is the axial coordinate, $v_{max} = v_2(L)$, P_2 is the axial force, and σ_2 is the

maximum extreme fiber stress (at $z = 0$) for BMJ Phase 2. From the assumptions made in Section 3.2.1, the BMJ Phase 2 ends when it reaches $v_{max} = b_c/2$. Therefore, the peak axial force that occurs at the end of BMJ Phase 2 (Point 3 in Figure 3.4 (a)), can be calculated as:

$$P_{peak} = P_{cr1}(1 + \frac{\pi^2(\frac{b_c}{4})^2}{8L^2}) \tag{3.8}$$

(3) Post-primary-buckling fixed-fixed mode unstable phase

This phase can be considered as a gradual transition from fixed-fixed mode to pinned-pinned mode. As it shows in Figure 3.5, the capped column is simplified using symmetry. Note that the boundary condition in this phase is a varying state between fully fixed and nominally pinned. The end cap is considered as a rigid bar due to the larger relative elastic modulus and smaller relative length. The boundary condition is modeled with a rotational spring connecting the rigid bar (end cap) to a roller support so that the end is free to move in the axial direction and also support an internal moment. The magnitude of the moment in the rotational spring is unknown. However, the trigger point of BMJ (Point 4 in Figure 3.4 (a)) can be predicted using an assumed trigger condition based on lateral sway ($v_{max} = l + b_c/2$, where $l = b_{cp}/2 - e_0$) of Section 2.1 combined with the assumption that the moment is small enough to ignored at the transition point from fixed-fixed to pinned-pinned boundary condition. The assumed trigger condition of lateral sway is based on when the axial stress on the cross-section area at the mid span moves out of the end cap area along in the z-axis projected area, which initiates the change of boundary condition and therefore the buckling mode jump behavior. The negligible small moment at the

transition point is assumed from that the contact area of the support end cap is decreasing towards a pinned-like condition when approaching the transition point, which suggests that the carried moment is approaching zero in the meanwhile.

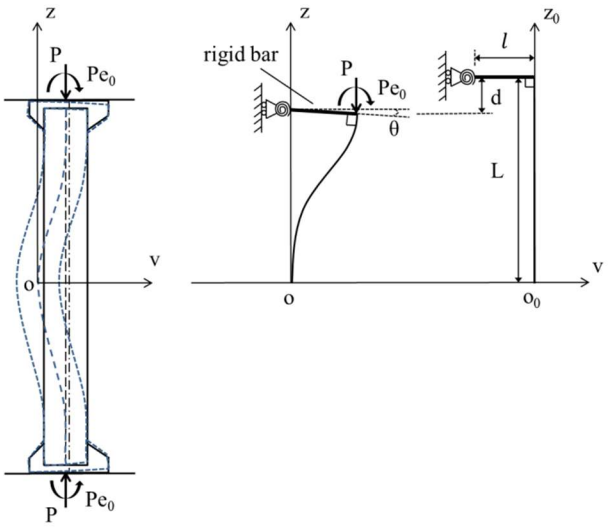

Figure 3.5 Idealized model for fixed-fixed mode buckling of capped column

Using the assumed lateral sway condition at the transition point (Point 4), the corresponding axial force and displacement can be derived. First, an assumption of the lateral deflection function is made. Since the buckled shape in this phase is between the buckled shapes under fully fixed and perfectly pinned boundary conditions, the deflection shape is considered as a combination of the buckled shapes under fixed-fixed and pinned-pinned boundary conditions. The Rayleigh-Ritz method is selected for this problem. The mixed buckled shape can be represented with two generalized degrees of freedom (DOF) a_1 and a_2. Two admissible functions $f_1(z)$ and $f_2(z)$ satisfying compatibility and essential boundary conditions are assigned the represent the deflection under changing mixed boundary conditions. The lateral deflection function of the capped half-column in BMJ Phase 3 can be written as:

$$v_3(z) = \sum_{i=1}^{2} a_i f_i \tag{3.9}$$

where:

$$f_1 = 1 - \cos(\frac{\pi z}{4L}) \tag{3.10}$$

$$f_2 = 1 - \cos(\frac{\pi z}{2L}) \tag{3.11}$$

Both f_1 and f_2 satisfy essential boundary conditions:

$$f_i(0) = 0,\ \frac{df_i}{dz}(0) = 0 \tag{3.12}$$

The unknown DOF a_1 and a_2 can be determined through the principle of stationary potential energy (Π_{p3}):

$$\frac{\partial \Pi_{p3}}{\partial a_i} = 0\,, \quad \text{for } i = 1, 2 \tag{3.13}$$

where Π_{p3} can be derived by assume the small rotation θ of the rigid end cap in this phase can be ignored:

$$\Pi_{p3} = \int_0^L \left(\frac{1}{2} E_c I_c (\frac{d^2 v_3}{dz^2})^2 + P_{cr2}(1 - \frac{1}{2}(\frac{dv_3}{dz})^2) \right) dz - P_{cr2} l \frac{dv_3}{dz}\Big|_{z=L} \tag{3.14}$$

where P_{cr2} is the axial force of the capped column at the BMJ trigger Point 4 (Figure 3.4 (a)). From Eq. (3.13), a_1 and a_2 can be solved as functions of P_{cr2} and the deflection function in terms of P_{cr2} can be obtained through Eq. (3.9). Then, based on the trigger condition assumptions made before, P_{cr2} can be solved using the moment equilibrium at $z = 0$:

$$-P_{cr2} \frac{b_c}{2} = E_c I_c \frac{d^2 v_3}{dz^2}\Big|_{z=0} \tag{3.15}$$

Then, with P_{cr2} known, the deflection function v_3 can be determined from Eq. (3.9) and (3.13) for the trigger point (Point 4) as well. The axial displacement and maximum extreme fiber stress σ_{cr2} of the column at Point 4 can also be solved with:

$$d_{cr2} = L_t - (2\int_0^L \frac{1}{2}\left(\frac{dv_3}{dz}\right)^2 dz - 2\frac{P_{cr2}L}{E_c A_c} + 2t_{cp}) \tag{3.16}$$

$$\sigma_{cr2} = \frac{E_c I_c \left.\frac{d^2 v_3}{dz^2}\right|_{z=0} \frac{b_c}{2}}{I_c} + \frac{P_{cr2}}{A_c} \tag{3.17}$$

Note that because the moment in the rotational spring is unknown in Phase 3, a linear relationship between axial force and displacement is assumed between Point 3 and Point 4 to describe the behavior of this phase (Figure 3.4 (a)).

(4) Forward mode jump phase

After the trigger point (Point 4), the buckling mode jumps with a change in boundary condition from fixed-fixed (surface contact) to pinned-pinned (edge contact). This transition would be nearly instantaneous in a physical specimen, resulting in a very sharp slope in the force-displacement relationship. The slope observed between Point 4 and 7 in Figure 3.4(a) is not as sharp as expected, due to the step size of the numerical simulation. For the analytical model, the forward mode jump phase is described by an instantaneous drop in stiffness.

(5) Post-secondary-buckling pinned-pinned mode phase

Similar as the BMJ Phase 3 (between Point 3-4 in Figure 3.4 (a)), this phase (between Point 5-6 in Figure 3.4 (a)) can be represented with the deflection function given in Eq. (3.9) ($v_5(z)$=$v_3(z)$). The reason is that the pinned-pinned mode of the capped column does not have a perfectly pinned boundary condition for the column at its joint with end caps as it shows in Figure 3.6. But the boundary condition at the

edge of end caps can be considered as fully pinned. So a difference from BMJ phase (3) is that the rotational spring is replaced with pinned connection between the rigid bar and the roller support in this phase (Figure 3.6). Because of the rigid connection between column end and end cap, there is still a small moment present at the center of the column end. Therefore, the buckled shape can be considered as a pinned-pinned dominated mixed buckling condition. Another difference from BMJ Phase (3) is that the rotation θ of the rigid end cap cannot be neglected anymore and the rigid end cap is forced to be a part of the buckled shape of the whole capped column (in phase (4), $L = 0.5L_t$ instead). This leads to a different calculation of potential energy (Π_{p5}) for BMJ phase (4):

$$\Pi_{p5} = \int_0^L \left(\frac{1}{2} E_c I_c \left(\frac{d^2 v_5}{dz^2} \right)^2 + P_5 \left(1 - \frac{1}{2} \left(\frac{dv_5}{dz} \right)^2 \right) \right) dz - P_5 l (1 - \frac{1}{2} (\frac{dv_5}{dz}\Big|_{z=L})^2) \frac{dv_5}{dz}\Big|_{z=L} \tag{3.18}$$

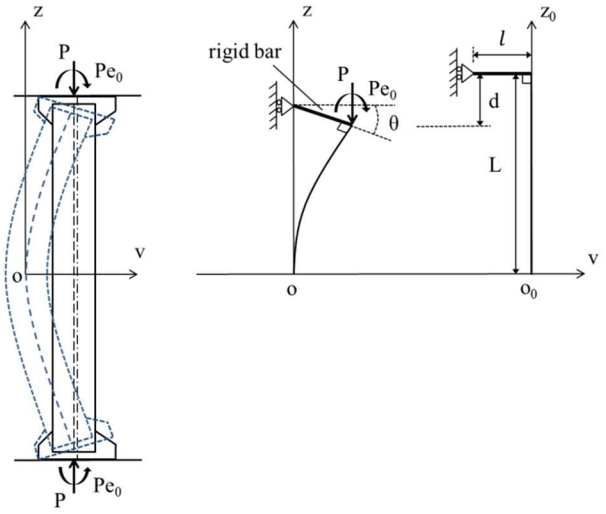

Figure 3.6 Idealized model for pinned-pinned mode buckling of capped column

The DOF a_1 and a_2 for BMJ Phase (4) can then be calculated with Eqs. (3.13) and (3.18) (replacing Π_{p3} with Π_{p5}) in terms of Phase (4) (between Point 4-7 in

Figure 3.4 (a)) axial force P_4. Based on that and the deflection function $v_5(z)$ can be obtained using Eq. (3.9). The relationship between column deflection the axial force can then be obtained as:

$$d_5 = L_t - (2\int_0^L \frac{1}{2}\left(\frac{dv_5}{dz}\right)^2 dz - 2\frac{P_5 L}{E_c A_c} + 2lsin(\frac{dv_5}{dz}\Big|_{z=L})) \tag{3.19}$$

Under known applied axial force or displacement, the maximum extreme stress can be solved similarly as Eq. (3.17):

$$\sigma_5 = \frac{E_c I_c \frac{d^2 v_5}{dz^2}\Big|_{z=0} \frac{b_c}{2}}{I_c} + \frac{P_5}{A_c} \tag{3.20}$$

With the analytical model derived above for Phase (5) (between Point 5-6 in Figure 3.4 (a)), the force-displacement relation can be predicted with a varying slope. The end of this phase is then defined at the point when the slope reaches 90 degrees (Point 6 in Figure 3.4 (a)).

(6) Backward mode jump phase

Similar as Phase (4), the backward mode jump phase (between Point 6-8 in Figure 3.4 (a)) is defined with a line of 90 degree slope, which starts from the end point of Phase (5) and ends when it returns to the linear Phase (1). This also corresponds to the 90 degree slope definition of the end point of Phase (5) in the analytical model.

3.2.3 Model verification

To verify the proposed analytical model, the model is developed with MATLAB R2014a (The MathWorks) and the predictions are compared with the results from quasi-static finite element simulations conducted using ANSYS for

capped columns with different geometry properties. The geometric properties are varied with the example capped column configuration in Section 3.2.1 serving as a baseline (properties listed in Table 3.1). Geometric variations are investigated using indices of slenderness (L_c/b_c), cap thickness ratio (t_{cp}/L_t), cap width ratio (b_{cp}/b_c), initial eccentricity ratio (e_0/L_t), depth ratio (d/b_c), and member size (L_t), by adjusting b_c, t_{cp}, b_{cp}, e_0, d, and L_t respectively. A comparison between analytical predictions and numerical simulation results are made for axial force, axial displacement, mid-span lateral sway, and maximum (mid-span) extreme fiber stress. Figure 3.7 and Figure 3.8 verified the analytical model with a good agreement between the analytical model prediction and numerical simulation result. The largest discrepancy is the prediction of the BMJ trigger point (Point 4 of Figure 3.4 (a)), likely due to that the assumption of negligible moment in the rotational spring (Figure 3.5) at this trigger point is not perfectly true; however, it is still a valid assumption for approximation based on the fairly good agreement between the analytical prediction and the numerical simulation. Overall, Figure 3.7 and 8 suggest that the analytical model is capable of capturing the full loading-unloading BMJ behavior based on the comparison with numerical simulation results.

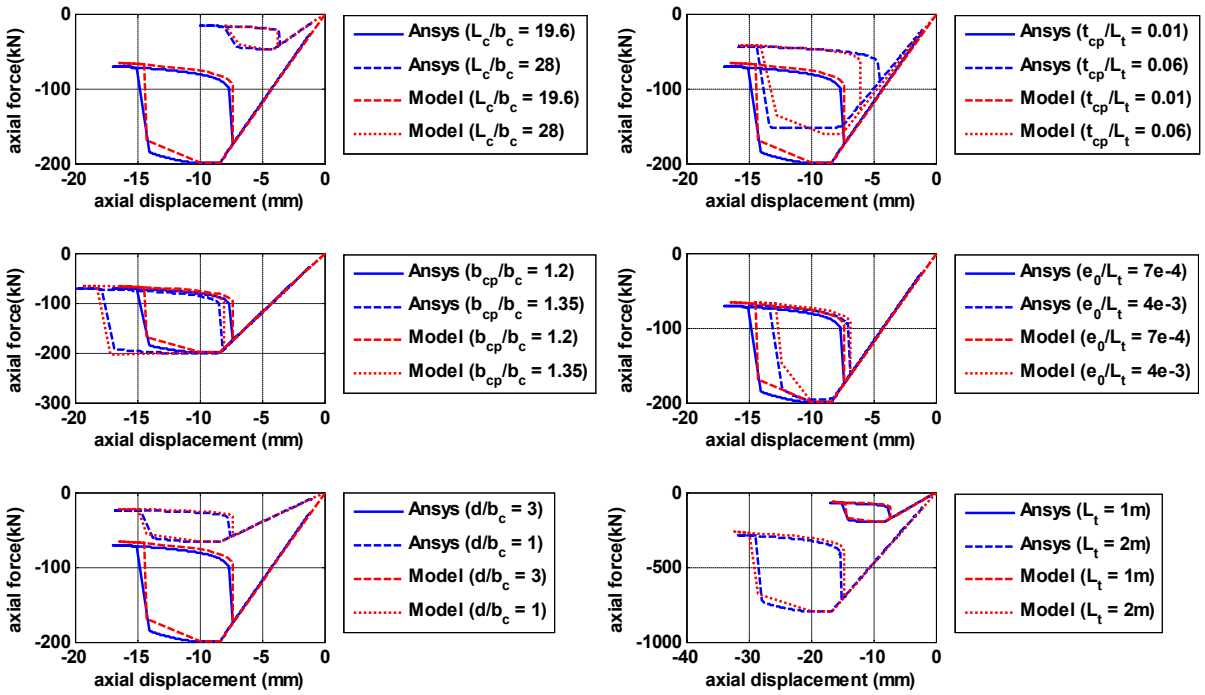

Figure 3.7 Axial force vs. axial displacement compared between analytical model prediction and ANSYS simulation results under varying geometric properties

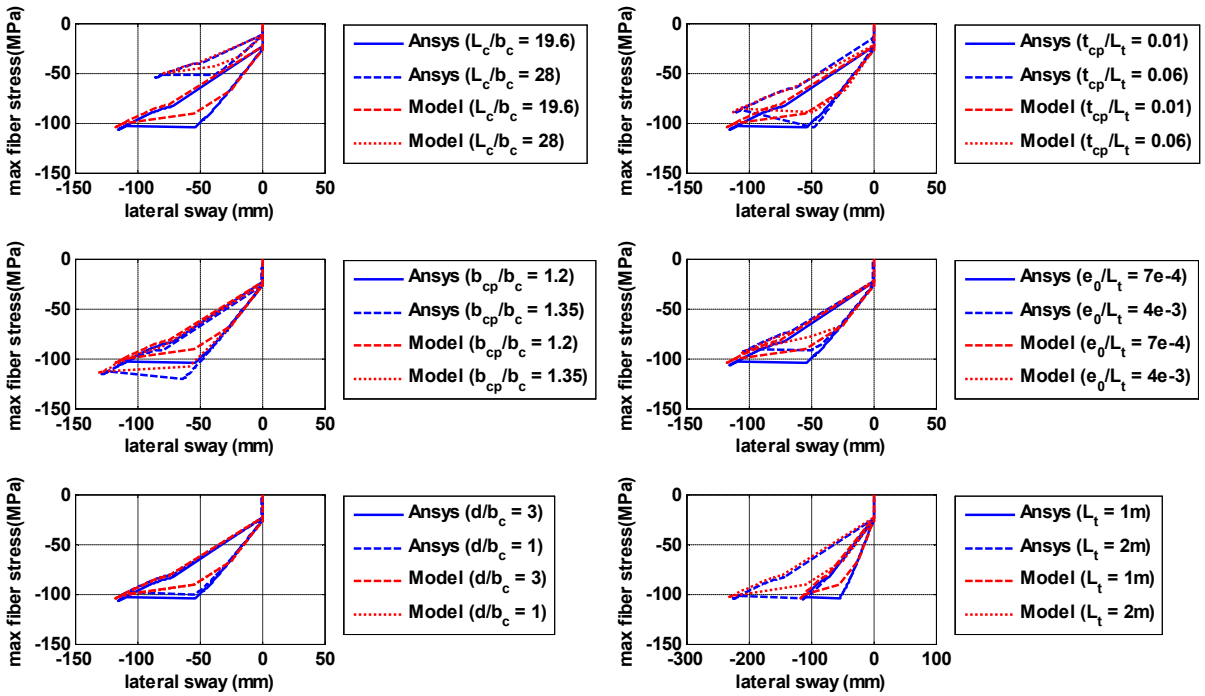

Figure 3.8 Mid-span lateral sway vs. maximum extreme fiber stress compared between analytical model prediction and ANSYS simulation results under varying geometric properties

3.3 Parametric Study

As it mentioned in Section 3.2.1, the BMJ behavior of the capped column can be controlled by the geometric properties. To clarify the influence of different geometric properties on the behavior, a parametric study is conducted in this section. Peak axial force (P_{max}), energy dissipation per cycle (E_d), axial deformation (normalized with respect to L_t) at BMJ trigger point, and material linear limit are considered as evaluation indices. The geometric properties that affect BMJ behavior investigated are slenderness, cap thickness ratio, cap width ratio, initial eccentricity ratio, depth ratio, and member size. The parametric study is performed by altering one geometric index at a time from the geometry of the example capped column used in Section 3.2.1. For each index, the varying geometric parameter is definedin Section 3.2.3. The results are displayed in Figs. 9-11.

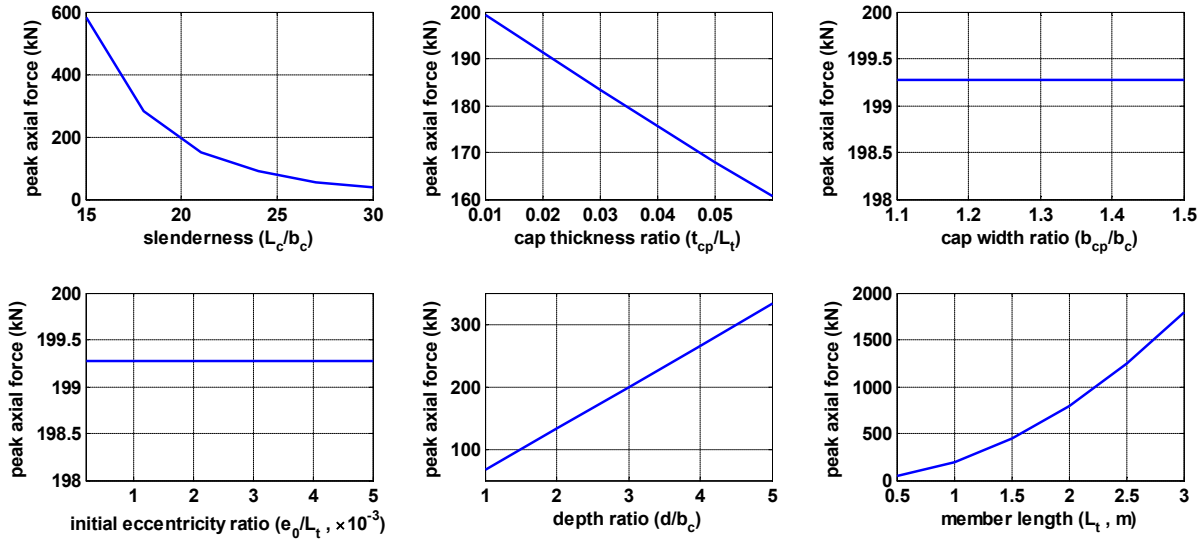

Figure 3.9 Effect of different geometric property on peak axial force

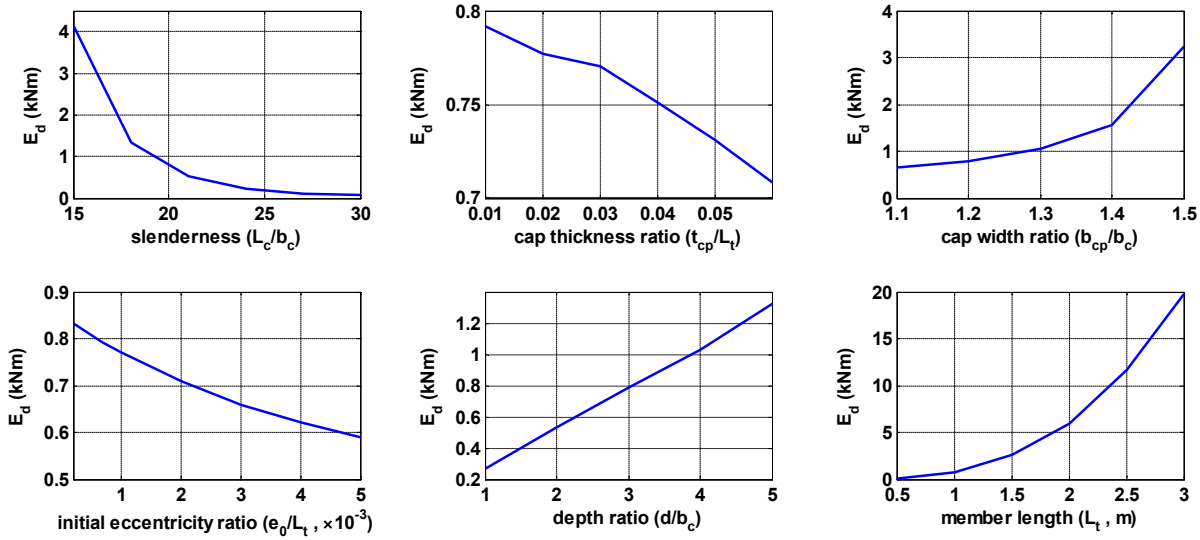

Figure 3.10 Effect of different geometric property on energy dissipation per cycle

The peak axial force, as shown in Figure 3.9, provides a beneficial feature for limiting the force transferred by the capped column if it is integrated into a structural system. The peak axial force of capped column can be increased with decreasing slenderness and cap thickness ratio and increasing depth ratio and member length.

The cap width ratio and initial eccentricity ratio do not affect the peak axial force. In terms of energy dissipation, Figure 3.10 suggests that to obtain more energy dissipation per cycle, the capped column can be designed with larger cap width ratio, depth ratio, or member length or with a lower slenderness, cap thickness ratio, or initial eccentricity ratio. The most efficient means to increase energy dissipation is to lower the slenderness.

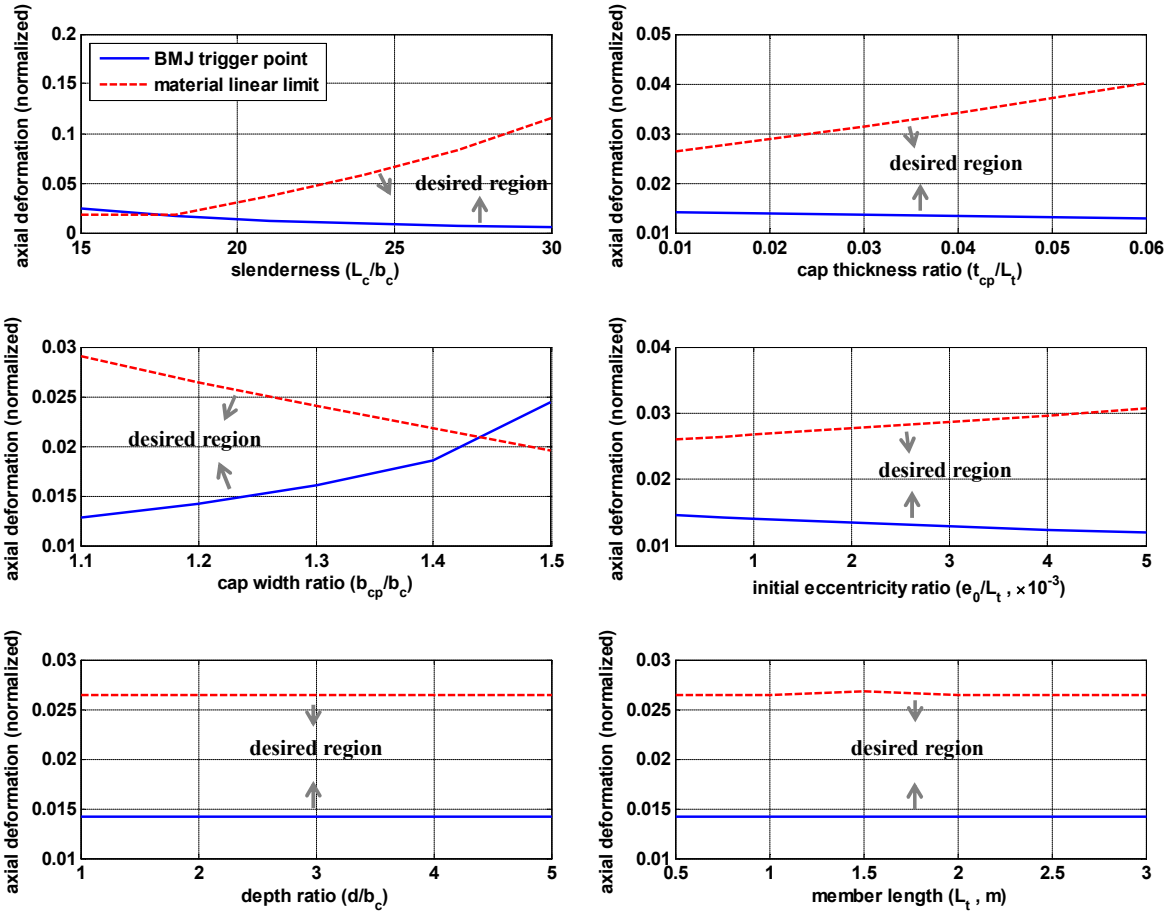

Figure 3.11 Effect of different geometric property on BMJ trigger point and material linear limit deformation

For the design of the capped column, it is important to ensure that the BMJ behavior is triggered in the targeted axial displacement working range and maintains linear material behavior at the same time. In that sense, Figure 3.11 provides a helpful

guidance for finding the desired region for the geometric design of the capped column. As it shows in Figure 3.11, the desired operational region is below the material yielding limit (to ensure elastic behavior) but above the BMJ trigger point line (to ensure that the BMJ mechanism occurs). Therefore, to ensure that the BMJ is triggered and to avoid material yielding, the slenderness needs to be at least larger than 18 and the cap width ratio cannot exceed 1.44 (for this particular base geometry). For more flexible displacement range after BMJ triggered, which is represented by the distance between the material linear limit and BMJ trigger line in Figure 3.11, the capped column can be designed with larger slenderness, cap thickness ratio, or initial eccentricity ratio, or with a smaller cap width ratio. The depth ratio and member length shows negligible effect on the desired region.

3.4 Seismic Performance of Frame Structure with BMJ Brace

As a potential application of the BMJ mechanism of the proposed capped column, a seismic bracing system is proposed in this section. The seismic performance of the BMJ brace system is numerically investigated in a 3-story steel frame structure which was originally used for a study of BRB frames (Sabelli 2001, Sabelli, Mahin et al. 2003). For the justification of the BMJ application, the seismic performance of the BMJ brace system is compared with the BRB system originally designed for the 3-story steel frame structure. Non-linear time history analysis is conducted with OpenSees (Frank McKenna) for numerical simulation. Twenty earthquake ground motions (LA01-20) developed with a variation of amplitude and frequency content by Somerville et al. (Somerville and Venture 1997) from fault-parallel and fault-normal orientations of 10 earthquake records are selected as ground

motion inputs. These earthquake ground motions correspond to a 10% chance of exceedance in a 50-year period and were also used in previous studies of the 3-story prototype structure considered (Zhu and Zhang 2007, Zhu and Zhang 2008).

The 3-story prototype structure is designed following FEMA building design criterion with a response factor of 8 and details can be found in (Sabelli 2001). For numerical simulation, only a single braced bay of the 3-story frame with additional gravity column members is modeled and analyzed as shown in Figure 3.12. The gravity column running through full height of the frame model is used to account for the contribution of the columns in the unbraced frame to the lateral stiffness of the structure with a moment of inertia of $4.23 \times 10^{-4}\ m^4$ and plastic modulus $4.75 \times 10^{-3}\ \mathrm{m}^3$ (Zhu and Zhang 2007). The seismic mass of each story in the single bay model is obtained by dividing the seismic mass of the story by the number of braced bays in each principal direction. Global P-Δ effects are considered based on the seismic mass. To account for the behavior of the gusset plates, all beam column connections are modeled as fixed except for the joints at the roof level (pinned). Beams and columns are modeled with nonlinear beam-column elements by considering nonlinear behavior in bending but linear behavior axially. Beams are then assumed to be inextensible by constraining the horizontal degree of freedoms into one at each floor. In other words, all nodes at the same story level are constrained in the horizontal direction (the direction of input ground motion) due to a rigid floor assumption. The frame is modeled as fixed at the base. The braces are modeled with pin-ended axial elements for both the BRB case and the BMJ case. The modal damping ratio in the first two modes is selected as 5 % using Rayleigh damping.

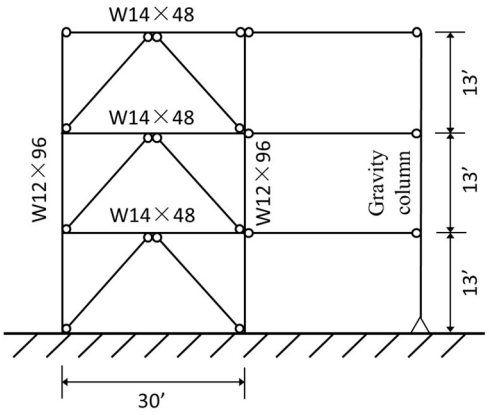

Figure 3.12 3-story braced frame model

For the bracing system, the main comparison of numerical simulation results is made between BMJ and BRB brace designs. An additional comparison to a conventional brace (CB) design is added using the results reported in (Sabelli 2001). For the BRB, the tension capacity and axial stiffness are listed in Table 3.3, and the compression capacity is assumed to be 1.1 times the tension capacity (Sabelli 2001, Sabelli, Mahin et al. 2003). The BRB is modeled with the SteelBRB element in OpenSees. For the BMJ brace, a schematic configuration is provided in Figure 3.13. The proposed design triggers BMJ behavior in both tension and compression using an inner and outer tube. The hollowed section of the inner and outer tube end enables relative back and forth displacement between the inner and outer end. Under brace compressive load, the inner and outer tube are unloaded, the capped column sets which are stabilized in place by the pre-stressed strands are further loaded in compression after closing their individual set gaps, and the pre-stressed strands are still stressed in tension until they are released with the loss of pre-strain. Under brace tensile load, the inner and outer tubes are loaded in tension, and the remainder of the components behaves as before.

To avoid either high forces or accelerations on the structure caused by high stiffness under minor excitations, or abrupt loss of brace stiffness after BMJ occurs, multiple sets of capped columns are used. Under such configuration, the stiffness can be gradually increased upon the increase in excitation. These sets of capped columns are placed inside the inner tube and are stabilized using 2 % pre-strain with corresponding sets of pre-stressed strands. Note that the end plates are always contacting the capped column end caps, but the pre-stressed strands will separate from the end plates when the pre-stress is released under compressive deformation of the capped columns. The strands are released before the BMJ behavior is triggered so that the pre-stressed strands will only affect (slightly increase) the axial stiffness within the 2 % pre-strain for each column set. Such behavior will be discussed later with simulation results. Each capped column set (i.e., all capped columns of similar length) should be placed evenly around the center of the device for the stability in the buckling phases. Different sets of capped columns can be placed with an offset in radian location so that the inner space can be more compact, avoiding interaction between the buckling deformations of different sets. Furthermore, the longer capped column sets will buckle first. Since the lateral sway of the longer capped column is larger than the shorter capped column due to its larger scale, this provides adequate room for the shorter capped column sets to buckle freely. The gaps enable the sets of capped columns to be triggered at different displacements. Thus, the restoring forces from the inner capped columns is only engaged when contact is made, creating a system of multiple triggered BMJ mechanisms. For the 3-story frame, 4 sets of capped columns, which are assigned with the same materials as mentioned in Section 3.2.1 and Table 3.2, are designed for the BMJ brace and the details are summarized in

Table 3.4. The BMJ brace analytical model is introduced to OpenSees simulation as an axial material model using Microsoft Visual C++ (Microsoft). Note that the axial force-displacement behavior in the derived analytical model is converted to the corresponding axial stress-strain behavior for the user developed axial material model, and all 6 BMJ phases are linearized to construct a multilinear material model for faster computation. The total BMJ brace behavior is modeled using a superposition of multiple axial brace elements with the multilinear material model of different settings corresponding to the different sizes of each column set.

Table 3.3 Properties of the BRBs in the numerical simulation

Story	Tensile strength (kN)	Axial stiffness (kN/m)
1st	520	1.030×10^5
2nd	872	1.651×10^5
3rd	1081	1.905×10^5

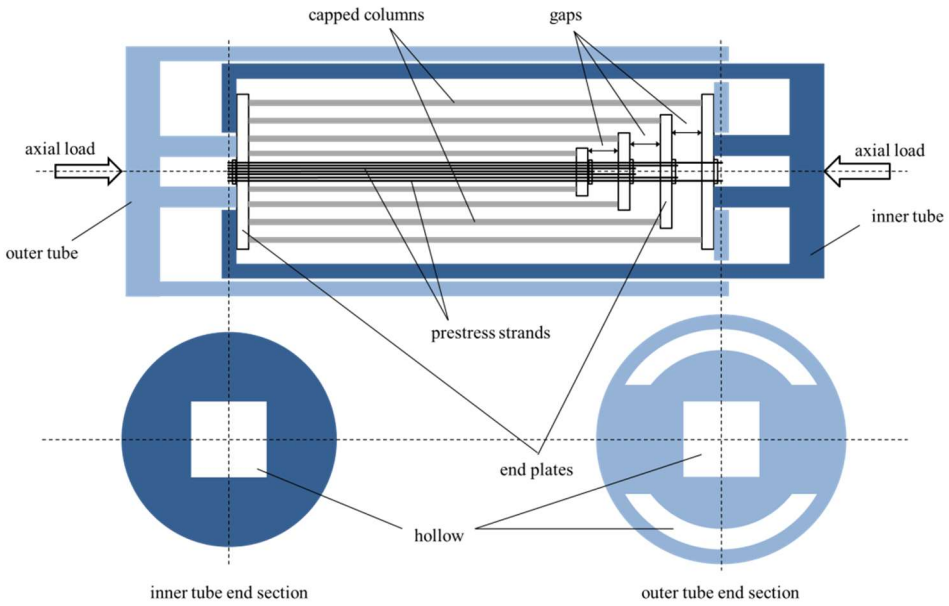

Figure 3.13 Schematic configuration of BMJ brace (not to scale)

The natural frequencies of the 3-story frame with BRB and BMJ brace are determined from the response of the frame under a band limit white noise. The

frequency content of the white noise is limited within 20 Hz and the noise power is determined by ensuring that the structure response is still linear. The first and second frequencies are 2.44 Hz and 6.25 Hz for the BRB frame and 1.95 Hz and 5.37 Hz for the BMJ braced frame. One thing to notice is that the pre-stressed strands add an additional stiffness onto the initial stiffness of the BMJ braces. As the pre-strain is released and the strands separate from the end caps, the brace stiffness will drop. Such influence on the initial stiffness of each column set can be observed in the brace behavior under earthquake excitation in terms of relatively steeper initial slopes compared to that after the pre-strain is released ($k_1 > k_2$, which is illustrated with a zoom-in window in the first subplot of Figure 3.16). Also, the stiffness considerably drops after primary buckling for each column set. Therefore, the natural frequencies of the BMJ frame are lower than the BRB case in the linear range from the results under white noise, and also expected to be lower than the BRB case after entering the nonlinear phase based on the observation of response period and brace stiffness (the overall slope in the force-displacement plots) under earthquake excitation from Figure 3.15 (a) and Figure 3.16.

Table 3.4 Details of BMJ brace at each story

Story	Capped column sets in BMJ brace											
	set 1 (outer) $b_c\backslash L_c = 25$ 2 columns			set 2 $b_c\backslash L_c = 22$ 2 columns			set 3 $b_c\backslash L_c = 20$ 2 columns			set 4 (inner) $b_c\backslash L_c = 20$ 4 columns		
	L_t (m)	d/b_c	Linear limit (mm)	L_t (m)	d/b_c	Linear limit (mm)	L_t (m)	d/b_c	Linear limit (mm)	L_t (m)	d/b_c	Linear limit (mm)
1st	1.68	3	123	1.668	4	70	1.65	5	48	1.63	10	47
2nd	1.53	3	112	1.518	4	64	1.5	5	43	1.48	10	43
3rd	1.43	3	105	1.418	4	60	1.4	5	40	1.38	10	40

The seismic response of the 3-story frame with CB, BRB, and BMJ braces under LA01-20 earthquake ground motions are summarized in Figure 3.14. Based on FEMA-356 (Council 2000), the allowable transient and permanent inter-story drift ratios for the life safety performance level are 2.5 % and 1.0 % respectively for steel moment resisting frames, and for the immediate occupancy performance level are 0.7 % and negligible respectively. The BMJ brace case demonstrates a comparable response in maximum drift ratio compared to the BRB case with maximum drift ratios from all LA01-20 excitations controlled below 2 % (satisfying allowable transient drift ratio for life safety performance level), which is considerably reduced from the CB case. For the 0.7 % allowable maximum drift ratio corresponding to the immediate occupancy performance level, the BMJ case satisfies the criteria for 5 ground motions, the BRB case satisfies the criteria for 15 ground motions, and the CB violates the criteria in all cases. A significant benefit from the self-centering feature of the BMJ brace is observed in the residual drift ratio comparison. There is negligible residual drift (maximum 0.0196 %) for the 3-story frame with BMJ brace under the earthquake suite, which satisfies allowable permanent drift ratio for both life safety performance level and immediate occupancy performance level. However, the residual drift criteria is greatly exceeded for the CB case and non-negligible (immediate occupancy performance level) for the BRB case, which implies potential permanent damage to structural members.

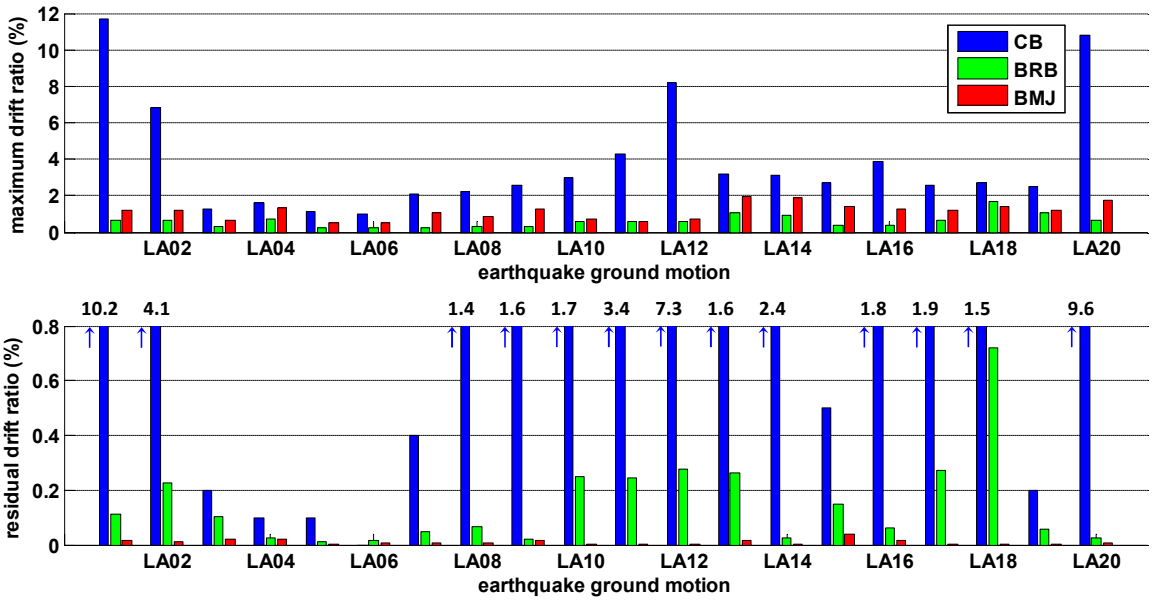

Figure 3.14 Seismic response of 3-story frame building with CB, BRB, and BMJ brace under earthquake ground motions LA01-20

The response of the 3-story frame with BRB and BMJ brace designs under the LA18 ground excitation (which produced the maximum residual drift for BRB frame) is investigated in detail in Figure 3.15 and 16. As it suggested in Figure 3.14, Figure 3.15 (a) demonstrates a similar maximum drift level between the BRB and BMJ frames with a noticeably more favorable residual drift in the BMJ frame. With the benefits on the mitigation on peak and residual drift response, it is worth noting that the BMJ frame shows a tradeoff on increased peak acceleration responses of each floor compared to the BRB frame in Figure 3.15 (b), which is expected with the improvement in deformation response. However, the overall level of floor absolute acceleration is still similar in the two cases. Furthermore, Figure 3.16 summarizes the axial force-displacement behavior of all 6 braces under LA18 earthquake input for both BRB and BMJ case. It can be seen that the BMJ behavior is triggered gradually through multiple sets of capped columns. The overall stiffness from the BMJ brace

system prevents excessive deformation, while the BMJ behavior provides some energy dissipation from each set. Note that the energy dissipation of BMJ brace is smaller than the BRB brace, which contributes to fewer BMJ simulation cases satisfying the 0.7 % allowable maximum drift ratio for immediate occupancy performance level. Such displacement performance may be improved with other sources of energy dissipation such as friction damping introduced to the BMJ brace, though the acceleration response may be increased in the meanwhile depending on the design of the system. In the case of the BRB, the energy comes from the yielding of the brace, contributing to the residual drift of the frame. Overall, the proposed BMJ brace is capable of achieving a desirable maximum drift performance as well as eliminating permanent drift. If the earthquakes were followed by an aftershock, the BMJ brace system would be best suited to mitigate further damage to the structure.

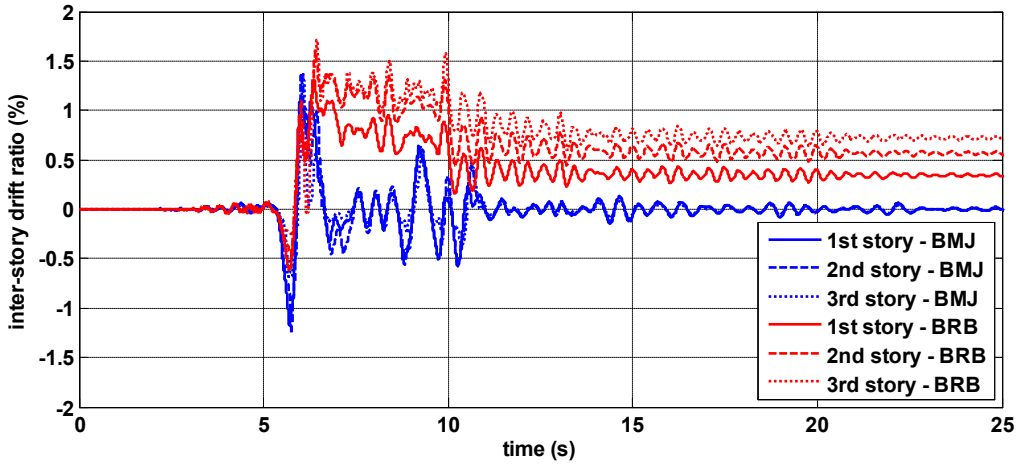

(a)

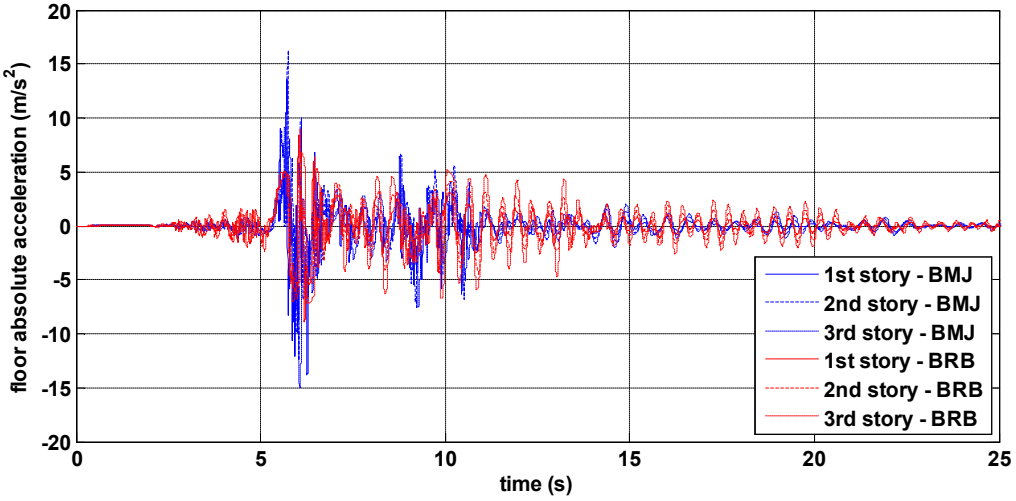

(b)

Figure 3.15 Response of 3-story frame building with BRB and BMJ brace under earthquake ground motion LA18: (a) inter-story drift ratio; (b) floor absolute acceleration.

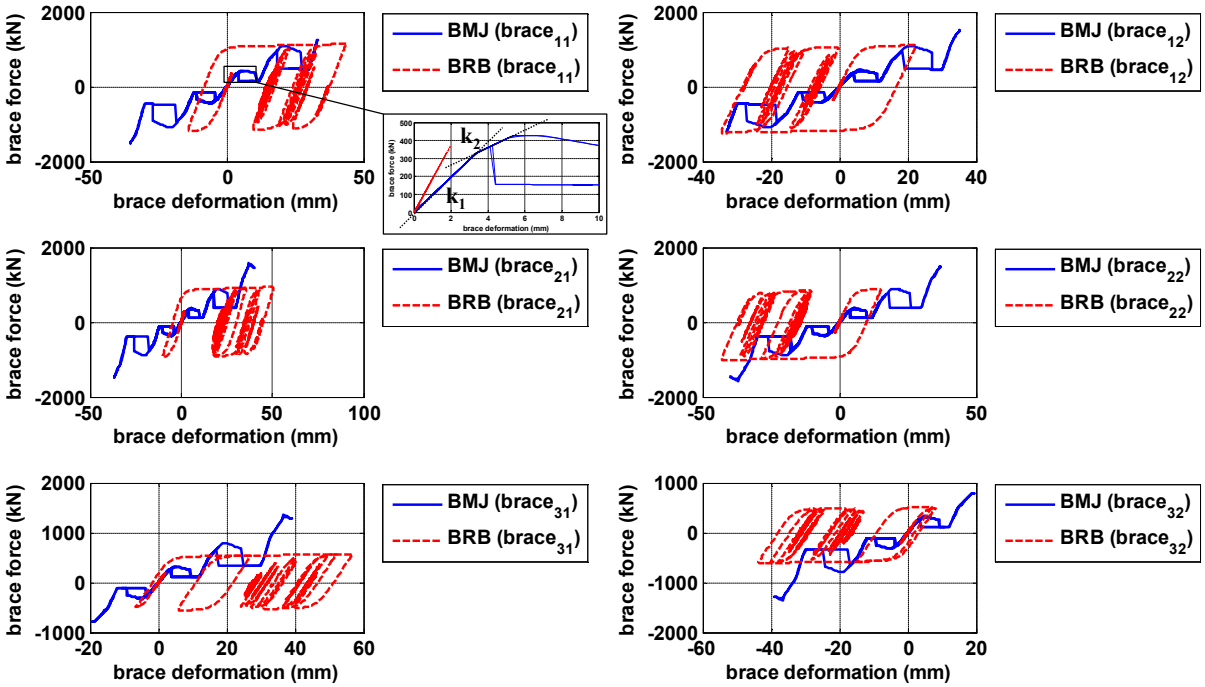

Figure 3.16 Axial force and deformation of BRB and BMJ braces under earthquake ground motion LA18 (brace$_{xy}$ stands for the y-th brace of x-th story)

3.5 Summary

A capped column design is proposed in this research to introduce the benefits of the buckling mode jump (BMJ) mechanism to civil infrastructure applications and especially proposed in a passive self-centering hysteretic damping brace design in this chapter. The BMJ behavior provides an alternative source of flag-shaped hysteresis damping with a self-centering feature. By allowing the end of the capped column to tilt, the boundary conditions change from fixed-fixed to a nominal pinned-pinned condition under increasing deformation. The change of buckling mode during the transition of boundary conditions generates the flag-shaped hysteresis loop without material yielding. An analytical model is proposed to characterize the BMJ behavior for the capped column geometry and function as guidance for design purposes. The analytical model is verified with numerical simulation results from the finite element software ANSYS. Parametric studies are also conducted to understand how geometric properties affect the BMJ performance and provide guidance for design. The indices investigated include the peak axial force, energy dissipation per cycle, axial displacement for triggering BMJ behavior, and limiting material to remain in the linear region.

Furthermore, a potential application for the BMJ behavior of the proposed capped column for civil structures is evaluated for a 3-story braced frame subject to earthquake loading. A schematic design of the BMJ brace incorporating multiple BMJ mechanisms is proposed in this chapter. The seismic performance of the 3-story braced frame is investigated under 20 earthquake ground motions for the case with BMJ brace, BRB, and CB. The BMJ braced frame demonstrates significant reduction in seismic peak drift responses from the CB case, and comparable reductions with the

BRB case. Moreover, the residual drift is non-negligible in the BRB case and severe in the CB case. On the other hand, the BMJ brace exhibits remarkable benefits with almost zero residual drift under all 20 earthquake excitations, though a minor tradeoff on acceleration responses is observed. The results demonstrate the great potential of the BMJ behavior of capped column as an economical alternative with its damage-free and reusable feature for achieving self-centering behavior along with flag-shaped damping. This could provide more seismic resilient design for steel braced structures, with reduced seismic vulnerability, redundant source of protection during aftershocks and less post-earthquake repair effort needed.

CHAPTER 4 CYBER-PHYSICAL STRUCTURAL SEISMIC RESILIENCE EVALUATION FRAMEWORK

In this chapter, a cyber-physical approach to the quantitative evaluation of structural seismic resilience is proposed. The cyber-physical system is developed using RTHS for partitioned numerical-experimental structural performance evaluation. The structural seismic resilience is assessed through fragility analysis based on IDA and loss/recovery functions. A modified golden section search algorithm, termed as MGSS-IDA, is developed to provide more efficient fragility analysis. The proposed framework is demonstrated through a case study on a nonlinear three-story steel moment frame as the numerical substructure with the seismic control device (MR damper) as the experimental substructure. The importance of incorporating cyber-physical system in seismic resilience evaluation is highlighted through comparison between full simulation and RTHS results. New control devices and algorithms to improve structural resilience can be developed, evaluated, and optimized through this framework.

4.1 Structural Seismic Resilience Quantification

Following the literature review in Chapter 2, the graphical quantification of seismic resilience is adopted here. For a structure under a seismic event at the considered design hazard level, the seismic resilience index R is quantified with Eq. (4.1) as follows:

$$R = \int_{T_{OE}}^{T_{OE}+T_{RE}} Q(t)dt \tag{4.1}$$

$$Q(t) = 1 - L(IM, T_{RE})\{H(t - T_{OE}) - H[t - (T_{OE} + T_{RE})]\} \cdot f_{Rec}(t, T_{OE}, T_{RE}) \tag{4.2}$$

where T_{OE} is the time of occurrence of an earthquake event E; T_{RE} is the recovery time from event E; $Q(t)$ is the dimensionless functionality measure of the structure and is defined with Eq. (4.2); $H(t)$ is Heaviside step function; $L(IM, T_{RE})$ is the loss estimation as a function of earthquake intensity measure IM at the considered design hazard level and recovery time T_{RE}; $f_{Rec}(t, T_{OE}, T_{RE})$ is the recovery function of time t.

As discussed in Section 2.2, the framework of seismic resilience includes properties of robustness, rapidity, redundancy, and resourcefulness, covering the dimensions on technical, economic, social, and organizational. From the aspect of structural engineering, it is directly related to the technical dimension and potentially interrelated to the other three dimensions. This study focuses on the seismic resilience in the technical dimension with influence on the economic dimension for quantitative evaluation. Relevant metrics include robustness and rapidity, using Eq. (2.3-2.4). Note that redundancy and resourcefulness are more closely related to organizational and social dimensions and are not considered in this quantitative study.

4.1.1 Loss and recovery function

As shown in Eqs. (4.1-4.2) and discussed in Chapter 2, the quantification of seismic resilience index R needs the definition of a loss function L and recovery function f_{Rec}. With the focus of this study on the development of the analysis framework, the loss estimation model provided in HAZUS (MRl 2003) is adopted and only the direct economic losses associated with the building itself (i.e. structural

and nonstructural losses) are considered for the technical and economic dimensions. As a result, the functionality Q(t) for a building considering seismic hazard is quantified as seismic loss in terms of building replacement cost in this research. In addition, this seismic loss is an expected value, due to that the loss estimation is based on median values considering a specific building structure type and occupancy class according to the HAZUS earthquake model. Note that the other loss categories can be further included according to the literatures mentioned in Section 2.2.1, with the availability of detailed information in addition to structural information (e.g., building occupancy and contents, business inventory, etc.). Also, more accurate loss estimation and recovery model can be used in replacement of the current adopted models on a case-by-case basis.

Based on HAZUS, the direct economic loss can be normalized with rehabilitation cost and represented with repair and replacement cost ratios RC with respect to specific damage states. Here, the normalized total loss L with respect to building replacement cost considered includes structural losses L_S and nonstructural losses L_{NS}. The nonstructural losses consist of drift-sensitive nonstructural losses L_{NSD} (e.g., partitions, ceiling, cladding, etc.) and acceleration-sensitive nonstructural losses L_{NSA} (e.g., mechanical equipment, utility system, etc.). Eqs. (4.3-4.6) give the adopted loss estimation model normalized by building replacement cost as follows:

$$L = \sum_{i}^{n} (L_{s,i} + L_{NSD,i} + L_{NSA,i}) \tag{4.3}$$

$$L_{s,i} = RC_{S,i} \cdot P_{S,i} \tag{4.4}$$

$$L_{NSD,i} = RC_{NSD,i} \cdot P_{NSD,i} \tag{4.5}$$

$$L_{NSA,i} = RC_{NSA,i} \cdot P_{NSA,i} \tag{4.6}$$

$$P_{S,i} = P_i\{R \geq r_{lim,S,i}\} - P_{i+1}\{R \geq r_{lim,S,i+1}\} \tag{4.7}$$

$$P_{NSD,i} = P_i\{R \geq r_{lim,NSD,i}\} - P_{i+1}\{R \geq r_{lim,NSD,i+1}\} \tag{4.8}$$

$$P_{NSA,i} = P_i\{R \geq r_{lim,NSA,i}\} - P_{i+1}\{R \geq r_{lim,NSA,i+1}\} \tag{4.9}$$

where n is the number of damage state considered; $L_{s,i}$, $L_{NSD,i}$, and $L_{NSA,i}$ are the structural loss, drift-sensitive nonstructural loss, and acceleration-sensitive nonstructural loss at damage state i respectively; $RC_{S,i}$, $RC_{NSD,i}$, and $RC_{NSA,i}$ are the cost ratio with respect to the building replacement cost at damage state i for structural, drift-sensitive nonstructural, and acceleration-sensitive nonstructural loss respectively; $P_{S,i}$, $P_{NSD,i}$, and $P_{NSA,i}$ are the probability of being in the damage state i for structural (defined in Eq. (4.7-4.9)), drift-sensitive nonstructural components, and acceleration sensitive nonstructural components; note that HAZUS defines cost ratios for being in a damage state instead of exceeding a limit state, and therefore lead to slightly different formulation from the general formulation in Eq. (2.5); R is the specified structural drift/acceleration response; $r_{lim,S,i}$, $r_{lim,NS\ ,i}$ and $r_{lim,NSA,i}$ are the performance criteria of limit state i in terms of drift/acceleration for structural, drift-sensitive nonstructural and acceleration-sensitive nonstructural loss respectively.

By assuming a well-prepared community, an exponential recovery function proposed by Kafali and Grigoriu (2005) is adopted here and is given in Eq. (4.10). For the recovery time at different damage states, HAZUS developed an estimation model considering two major parts: the construction/clean-up time and the time needed for financing, permits, and design. Considering these major base components

in estimating recovery time, the structural damage states are assumed to dominate the recovery time estimation in this study.

To employ the HAZUS recovery time estimation per damage state in the probabilistic resilience frame, a probabilistic formulation (Eq. (4.11)) similar as the loss estimation model (Eq. (4.3-4.6)) is proposed in this study to estimate the probabilistic recovery time T_{RE}, based on the probabilities of exceeding each structural limit state ($P_{S,i}$) and the loss of function time (LOF_i) at damage state i. LOF_i can be estimated using the model provided by HAZUS (Eq. (4.12)), which is based on the building construction and clean up time (BCT_i) and the construction time modifier (MOD_i) at damage state i for different building types. Median estimates of BCT_i (judgmentally derived based on ATC-13, Table 9.11) is given in HAZUS with the consideration on the time needed for project tasks (e.g. decision-making, financing, inspection, etc.) in addition to construction. MOD_i is derived judgmentally in HAZUS to account for the options to help the functional recovery (e.g. rent alternative space, use spare industrial capacity elsewhere, etc.) depending on the building occupancy type. Note that in this research, the functional recovery is quantified through the recovery of expected seismic loss over time for the specific building structure type and occupancy class considered. More realistic heavy step (i.e. binary) recovery function/profile can be used instead following Eq. (2.2), if detailed loss and recovery information of the specific single building is available.

$$f_{rec}(t, T_{OE}, T_{RE}) = \exp(-(t - T_{OE})\ln(200)/T_{RE}) \tag{4.10}$$

$$T_{RE} = \sum_{i}^{n} LOF_i \cdot P_{S,i} \tag{4.11}$$

$$LOF_i = BCT_i \cdot MOD_i \tag{4.12}$$

4.1.2 Fragility function

To obtain the damage state probabilities for loss and recovery analysis, fragility curves need to be derived for both structural and nonstructural damage states. As discussed in Section 2.2.3, the widely used lognormal distribution function ($\Phi()$) is adopted to define the seismic fragility function of a damage state DS and is given in Eq. (4.13) for an intensity measure (IM) of x at considered design hazard level, where DS is defined by structural response exceeding the corresponding limit state ($R_i \geq r_{lim,i}$). The lognormal fragility function can be derived with estimation on its moment, logarithmic median and standard deviation ($\ln(\theta)$ and β). The estimation on the moments of the lognormal distribution is performed based on the structural response data collected through the commonly used IDA approach in this dissertation.

$$P(DS|IM = x) = \Phi\left(\frac{\ln(x/\theta)}{\beta}\right) \tag{4.13}$$

Based on the IDA curves under a selected suite of ground motions, the IMs that exceed each limit state indicating respective DS can be obtained. Based on the IM data of each DS, the moments of the lognormal distribution are estimated using the maximum likelihood method in this dissertation. The adopted maximum likelihood estimator (MLE) finds the moments of the lognormal distribution that maximize the likelihood of producing the observed data, following Eq. (4.14-15) (Baker 2015, Porter 2015).

$$Likelihood = \prod_{i=1}^{n} \Phi\left(\frac{\ln\left(IM_{DS,i}/\theta\right)}{\beta}\right) \tag{4.14}$$

$$\{\hat{\theta}, \hat{\beta}\} = \arg_{\theta,\beta} \max(likelihood) \quad (4.15)$$

where n is the number of ground motions; $IM_{DS,i}$ is the intensity measure that causes the specific DS under ground motion i; $\prod_{i=1}^{n}( )$ denotes the product of the values inside the bracket from 1 to n; $\arg\max( )$ denotes the argument of the maxima.

4.1.3 Building damage states

According to HAZUS, the building damage states considered for loss estimation are defined in four categories for structural or drift-/acceleration-sensitive nonstructural damage: slight (SD), moderate (MD), extensive (ED), and complete (CD). The four damage states has different structural response threshold on the limit states for structural or drift-/acceleration-sensitive nonstructural damage of different building types and can be found in HAZUS (MRl 2003). The structural damage states defined by HAZUS are using peak inter-story drift (δ_{max}) as the damage measure (DM). However, the seismic losses under earthquakes with intermediate intensities are often dominated by the losses due to residual inter-story drifts, especially for ductile buildings (Ramirez and Miranda 2012). Additionally, seismic residual drifts may lead to a complete loss of the structure (Erochko, Christopoulos et al. 2010, Ramirez and Miranda 2012). Therefore, only using peak structural response as the damage measure may lead to underestimations of seismic losses (e.g. excessive inter-story residual drift may lead to loss of building functionality and cost on full/partial demolition).

As a result, this study includes peak residual inter-story drift ($\delta_{max,res}$) as additional damage measure for the ED and CD structural damage states (assuming to be potentially influenced more by residual inter-story drift) in addition to the HAZUS

damage states thresholds defined on δ_{max}. The performance-based design under the considered design seismic hazard level (e.g. 2%/50-year or 10%/50-year) gives recommended values corresponding to building performance levels for both $\delta_{res,max}$ and δ_{max}. Considering that the building functionality and damage states are strongly related to the performance levels, the δ_{max} and $\delta_{res,max}$ criteria on life safety and collapse prevention limit states from ASCE/SEI 41-13 (Engineers and Institute 2014) is adopted in parallel and combined with the δ_{max} threshold from HAZUS in defining structural performance limit states for the intermediate structural damage states (i.e. structural MD and ED). Note that the threshold being exceeded first during IDA will be the governing criteria of the corresponding limit state. A diagram illustrating the combined structural limit states thresholds and the limit states thresholds adopted for nonstructural damage states defined by HAZUS is given in Figure 4.1.

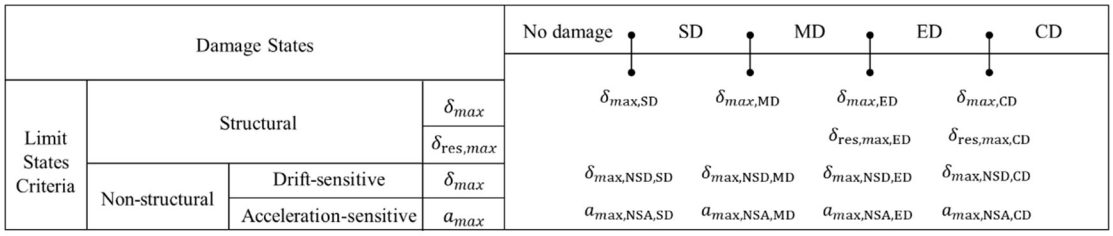

Figure 4.1 Building damage states and corresponding limit states criteria

4.1.4 Uncertainties

The sources of uncertainties in fragility analysis can be categorized into aleatoric and epistemic uncertainties (Der Kiureghian and Ditlevsen 2009). The aleatoric uncertainties are from the inherent randomness of the problem, which is essentially irreducible, while the epistemic uncertainties are due to lack of knowledge (e.g. analysis assumptions, model simplification, limitation in supporting database, etc.), which can be reduced with improvement in knowledge base. As mentioned in

Section 4.1.2, the moments of the lognormal distribution can be estimated using MLE based on the observed data from IDA. The obtained estimated logarithmic standard deviation $\hat{\beta}$ captures the record-to-record variability, which is considered as an aleatoric uncertainty. For the epistemic uncertainties, modeling uncertainties are considered, including that from structural model ($\beta_{M,SM}$) and the estimated structural response threshold of damage states ($\beta_{M,DS}$).

It is adopted here that $\beta_{M,SM} = 0.2$, which is suggested by Ellingwood et al. (2007). The values of $\beta_{M,DS}$ for different types of damage state (i.e. structural and drift-/acceleration-sensitive nonstructural DS) follow the suggestions of HAZUS (MRl 2003) in this dissertation. Note that if more case-specified model uncertainties are needed, it can be determined through Monte Carlo simulations considering a distribution of various model parameter values. All the uncertainties are combined using the mean estimates approach (Liel, Haselton et al. 2009, Benjamin and Cornell 1975), which keeps the median $\hat{\theta}$ estimated from the analysis under aleatoric uncertainty as the median θ of the lognormal distribution, and combines the additional epistemic uncertainties with the aleatoric uncertainty (estimated as $\hat{\beta}$) as the logarithmic standard deviation β in Eq. (4.10). Here, the combination of the considered uncertainties follows Eq. (4.13).

$$\beta = \sqrt{\hat{\beta}^{\,2} + {\beta_{M,SM}}^{2} + {\beta_{M,DS}}^{2}} \tag{4.13}$$

4.2 Structural Seismic Resilience Cyber-Physical Evaluation Framework

The proposed cyber-physical framework for quantitative evaluation of structural seismic resilience is discussed in this section. RTHS is adopted to create the

cyber-physical system. A schematic diagram showing the methodology steps of the proposed framework is given in Figure 4.2. As discussed in Section 4.1, the main steps include fragility analysis, loss analysis, and recovery analysis. The fragility analysis is conducted using MLE based on the incremental dynamic analysis (IDA) results on intensity measure (IM) at different limit states, providing the estimated probabilities of structural (S) or drift-/acceleration-sensitive nonstructural (NSD/NSA) damage states (DS). Here, a cyber-physical system is integrated for the IDA process through RTHS approach, allowing more realistic and accurate capture of complex system response that may not be able to be accurately modeled numerically. Detailed implementation of the proposed framework is demonstrated through a case study in Section 4.3.

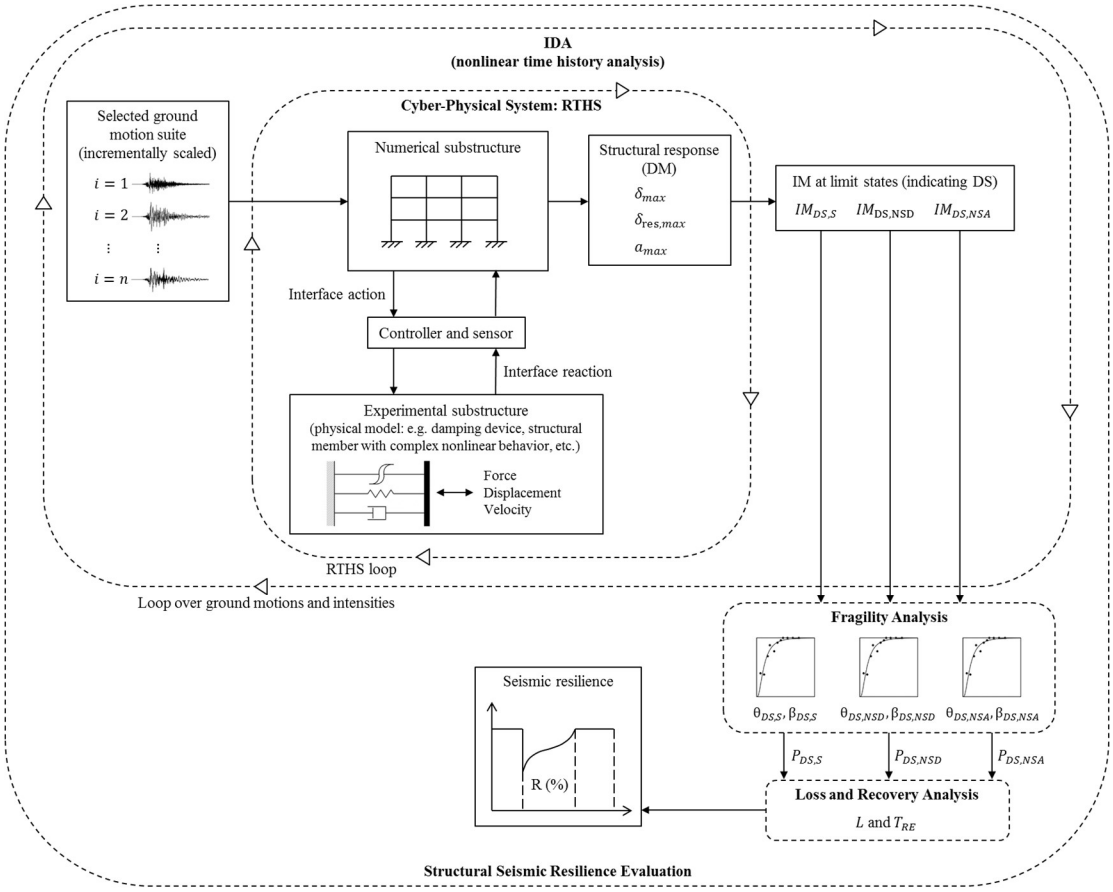

Figure 4.2 Schematic diagram of structural seismic resilience cyber-physical evaluation framework using IDA

4.3 RTHS Case Study

It may not be possible to accurately represent structures with nonlinear rate-dependent components by purely numerical models, especially when it comes to the wide frequency and magnitude range under IDA analysis. Therefore, a structure with magnetorheological (MR) dampers is considered here as a case study to demonstrate the implementation of the proposed structural seismic resilience cyber-physical evaluation framework.

4.3.1 Structural model and IDA-RTHS setup

A 3-story steel moment frame designed for the SAC Phase II Steel Project (Krawinkler 2000) representing a typical low-rise building in Los Angeles, California, is adopted as the numerical substructure with additional MR dampers as experimental substructure providing energy dissipation in this case study. Due to the symmetry in two principal direction of the frame, only half of the structure is taken for numerical modeling. The structural model including one moment-resisting perimeter frame with an additional column representing the interior gravity frames in their weak axis. The original structural model is shown in Figure 4.3. The structural fundamental natural frequency is 1.0065 Hz. The MR dampers are added as a retrofit option here, intended to improve energy dissipation and therefore reduce structural seismic responses/demands. The MR dampers are assumed to be installed through bracing between the base and either the first or the third story. The brace is assumed to be rigid and the MR damper force is directly modeled as an applied nodal force.

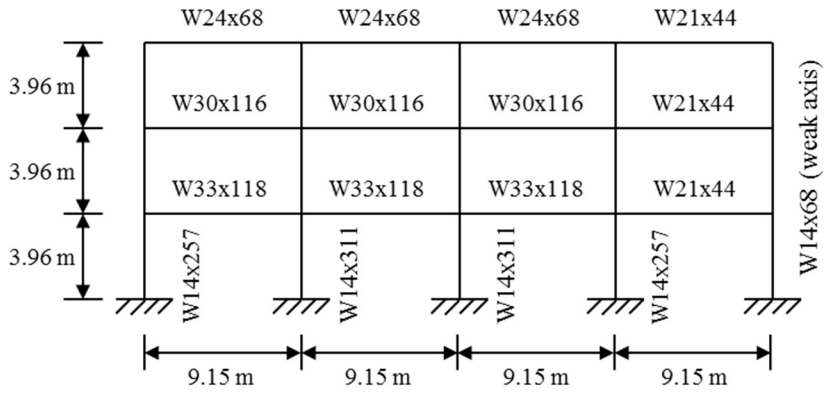

Figure 4.3 Structural model of a 3-story steel moment frame with additional MR dampers

For the implementation of the HAZUS loss estimation model, the low-rise 3-story steel moment frame (building type: S1L) is assumed to be occupied for professional/technical/business service (occupancy class: COM4). The corresponding limit state thresholds combined from HAZUS and performance-based criteria for steel moment frame are given in Figure 4.4, where the inter-story drifts (e.g. δ_{max}) are represented in the form of inter-story drift ratios (the ratio between the drift and the story height h, e.g. $\theta_{max} = \frac{\delta_{max}}{h}$) and the acceleration response are represented with respect to the gravity acceleration g.

Damage States				No damage	SD	MD	ED	CD
Limit States Criteria	Structural		θ_{max}	0.6%	1.2%	3%	8%	
			$\theta_{res,max}$			1%	5%	
	Non-structural	Drift-sensitive	θ_{max}	0.4%	0.8%	2.5%	5%	
		Acceleration-sensitive	a_{max}	$0.3g$	$0.6g$	$1.2g$	$2.4g$	

Figure 4.4 Damage states thresholds for the 3-story steel moment frame

To allow the nonlinear time history analysis to be conducted in real time within the RTHS framework, a real-time nonlinear 2D dynamic analysis platform under MATLAB/Simulink environment termed RT-Frame2D is adopted (Castaneda

Aguilar 2012, Castaneda, Gao et al. 2013) to model the numerical substructure. The aforementioned 3-story steel moment frame is modeled with nonlinear beam-column elements in RT-Frame2D with the explicit unconditionally-stable CR integration scheme (Chen and Ricles 2008). A 1000 Hz sampling frequency is selected for the numerical integration. Concentrated plasticity model is adopted for the nonlinear beam-column elements in RT-Frame2D, assuming that the yielding occurs at the element ends. A bilinear moment-curvature hysteresis material model with kinematic hardening and a post yielding ratio of 2.5% is applied. Note that the P-Delta effect is not included, but will be considered in future studies. The element properties including linear flexural rigidity (EI), axial rigidity (EA), shear rigidity (GA) and yield curvature κ are given in Table 4.1. Mass is assigned with 4.78×10^5 kg and 5.17×10^5 kg distributed over the beam elements for the first/second and third floor respectively. Rayleigh damping is assigned with 5% for the first mode with directly defined Rayleigh damping coefficients ($\alpha = 0.4977, \beta = 1.7186 \times 10^{-4}$). The structural model has a total of 60 degrees of freedom (DOF), with each node of 3 DOF (i.e. horizontal, vertical and rotational DOF). With the rigid floor assumption and the fixed base boundary condition, the model for nonlinear time history analysis is reduced to 36 DOF.

Table 4.1 Element properties of the structural model

Member section	W14×257	W14×311	W14×68	W33×118	W30×116	W24×68	W21×44
EI ($N\cdot m^2$)	2.83×10^8	3.60×10^8	1.01×10^7	4.91×10^8	4.10×10^8	1.52×10^8	7.02×10^7
EA (N)	9.75×10^9	1.18×10^{10}	2.58×10^9	1.00×10^{10}	1.00×10^{10}	1.00×10^{10}	1.00×10^{10}
GA (N)	8.90×10^{15}	8.90×10^{15}	8.90×10^{15}	8.90×10^{15}	8.90×10^{15}	8.90×10^{15}	8.90×10^{15}
κ (m^{-1})	9.24×10^{-3}	8.98×10^{-3}	1.97×10^{-2}	4.46×10^{-3}	4.87×10^{-3}	6.14×10^{-3}	7.18×10^{-3}

The IDA-RTHS process requires iteratively scaling the input excitation which is sequentially selected from the adopted ground motion suite. Such process is more efficient with an automatic platform, in particular when integrating experimental testing. Here, a hardware-in-the-loop (HIL) testing tool, AutomationDesk, is used to realize the automatic IDA-RTHS. The RTHS framework including ControlDesk software and MATLAB functions is embedded into AutomationDesk through Python scripts. The overall flowchart of the automatic IDA-RTHS process under AutomationDesk environment is illustrated in Figure 4.5.

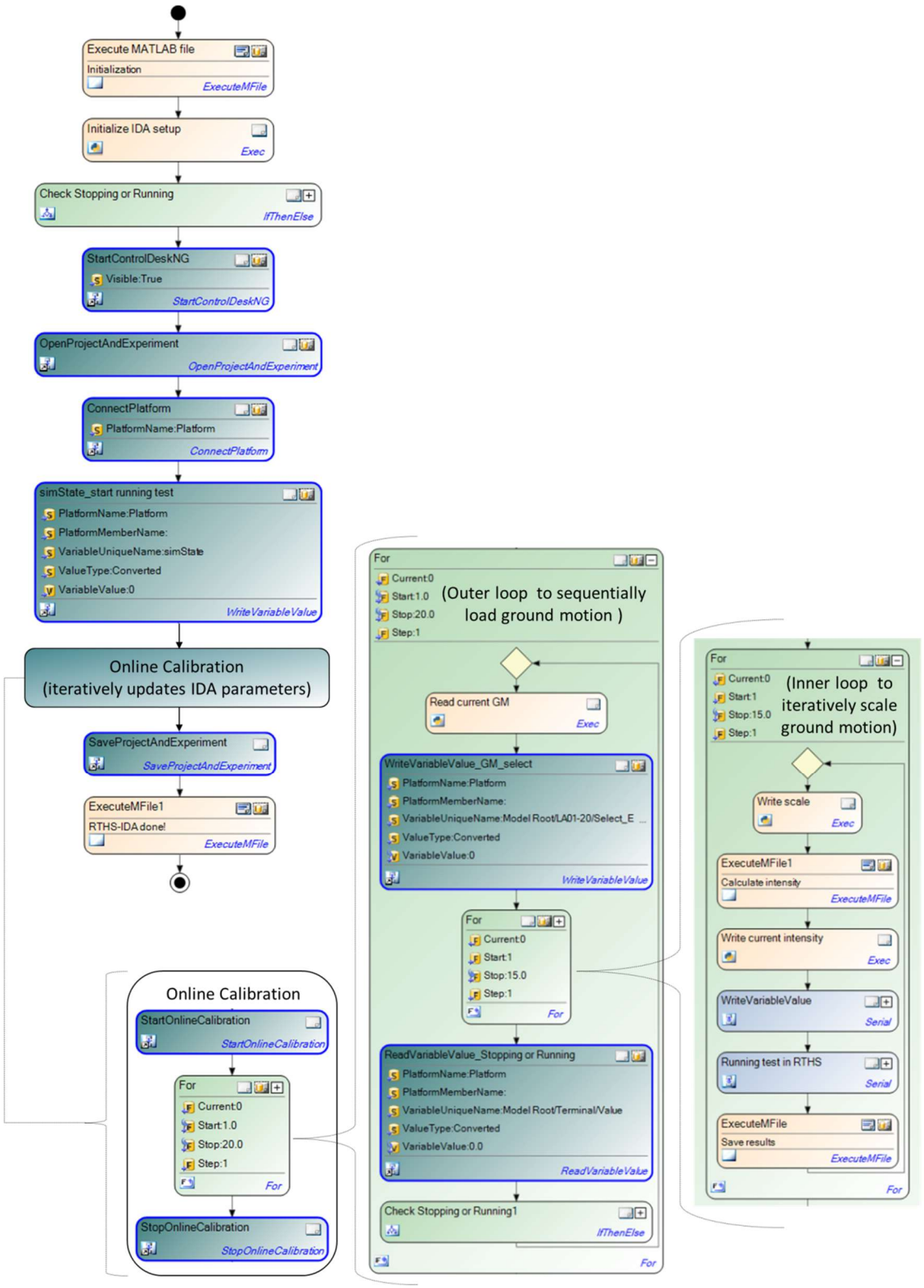

Figure 4.5 Automatic IDA-RTHS process under AutomationDesk environment

The detailed RTHS framework and setup is illustrated in Figure 4.6. It consists of a dSPACE DS1103 Controller Board, a windows-based host PC with ControlDesk software, an MTS servo-hydraulic test system, and a second-generation large-scale MR damper manufactured by the Lord Corporation. The dSPACE controller board paired with ControlDesk provides real-time control (i.e., control on MTS actuator and MR damper current following the command from numerical model) and data acquisition, and is fully programmable under MATLAB/Simulink environment and therefore compatible with the RT-Frame2D platform. The dSPACE board has 8 16-bit D/A channels and 20 16-bit A/D channels to provide interface action control and reaction sensing between numerical and experimental substructures.

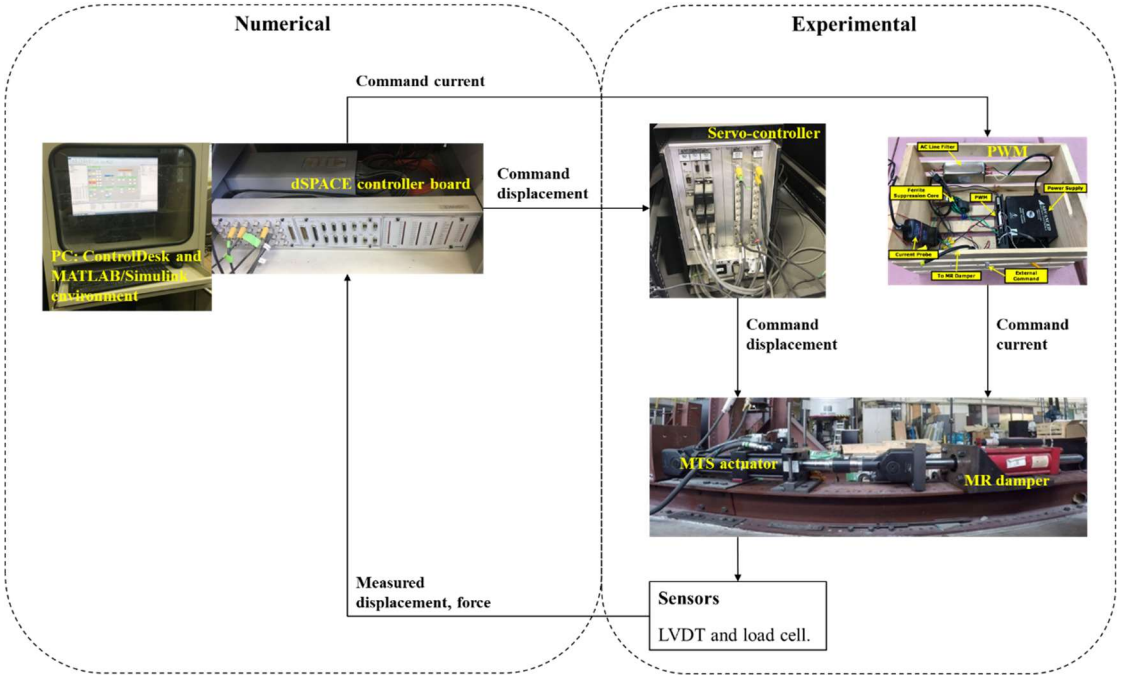

Figure 4.6 RTHS framework and setup

The servo-hydraulic test system includes an MTS actuator with displacement feedback through an internal LVDT, a hydraulic power supply (60 gpm, 227 lpm), a

hydraulic service manifold (50 gpm, 189 lpm), a 4-channel servo-control system with FlexTest 60 controller, and MTS test software. The MTS actuator provides a maximum force of 245 kN with a stroke of ±12.7 cm. The MR damper has a capacity of 200 kN and stroke of ±33 cm. The semi-active control of the MR damper is applied using a pulse-width modulator (PWM). Figure 4.7 shows a photo of the PWM, which consists of an Advance Motion Controls model PS2x300W unregulated 80 VDC power supply, an Advance Motion Controls model 30A8 analog servo-drive to measure the current in the closed-loop circuit for feedback control, an AC line filter to reduce the noise contamination from PWM to nearby equipment though AC supply, and a ferrite suppression core to attenuate the noise from PWM switching. The MR damper is connected to the MTS actuator through a steel plate using a large threaded rod and four high strength bolts. A load cell is installed to measure the restoring force of the MR damper. The current in the MR damper circuit is measured using a Tektronix model A622 current probe. The MTS actuator and MR damper are mounted on steel angles fixed on I-beams tied down to the strong floor.

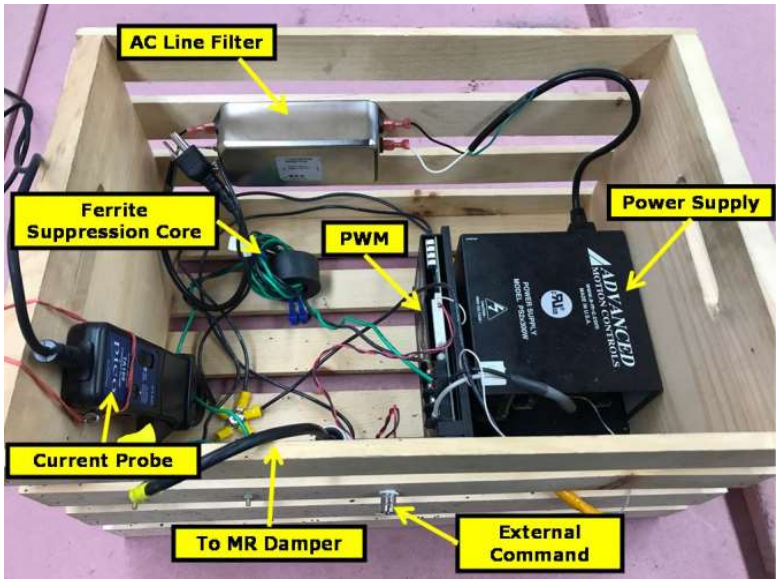

Figure 4.7 PWM for current excitation of MR damper

The signals are communicated through BNC cables connecting the MTS controller (conditioning LVDT and load cell) and dSPACE controller in analog format. The analog signals from the LVDT and the load cell are filtered by an analog low-pass filter with a cutoff frequency of 500 Hz before sending to the dSPACE controller. The dSPACE controller samples the analog signal from experimental substructure to digital signal for the numerical substructure, and converts the command digital signal from numerical substructure into analog signal before sending to experimental substructure.

4.3.2 MR damper model and semi-active control

The large-scale MR damper can be implemented in three modes: passive-off (P-off) with 0 Amps input current, passive-on (P-on) with 2.5 Amps input current, and semi-active with variable input current. For comparison with the results from the RTHS framework, the MR damper (i.e., the experimental substructure) is also modeled with a numerical model under MATLAB/Simulink environment to provide feedback force to the numerical substructure. The MR damper is modeled numerically using a high-fidelity phenomenological model proposed by Spencer Jr, Dyke et al. (1997) which is based on a Bouc-Wen hysteretic model, shown in Figure 4.8. This model outputs the damper restoring force F with a given input displacement x and velocity $\dot{x}$. The model parameters are fitted through sine wave tests with different amplitudes/frequencies (Phillips and Spencer Jr 2012), under the two passive scenarios of the MR damper with two levels of applied current: passive-off (0 Amps) and passive-on (2.5 Amps). According to Phillips and Spencer Jr (2012), the

large-scale 200 kN MR damper restoring force can be approximates by solving Eq. (4.14-21) based on force equilibriums and the Bouc-Wen hysteretic model (Baber and Wen 1981) with the fitted parameters given in Table 4.2, where i_c is the applied current. Note that the MR damper model works well for passive control, but loses accuracy under variable current for semi-active control.

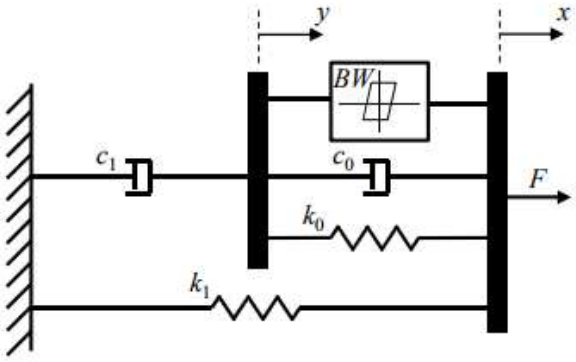

Figure 4.8 Phenomenological model of the MR damper

$$F = \alpha z + c_0(\dot{x} - \dot{y}) + k_0(x - y) + k_1(x - x_0) \tag{4.14}$$

$$c_1\dot{y} = \alpha z + k_0(x - y) + c_0(\dot{x} - \dot{y}) \tag{4.15}$$

$$\dot{z} = -\gamma|\dot{x} - \dot{y}|z|z|^{n-1} - \beta(\dot{x} - \dot{y})|z|^n + A(\dot{x} - \dot{y}) \tag{4.16}$$

$$\alpha = \alpha_b + (\alpha_a - \alpha_b)\, e^{-\alpha_c i_c} \tag{4.17}$$

$$c_0 = c_{0,b} + \left(c_{0,a} - c_{0,b}\right) e^{-c_{0,c} i_c} \tag{4.18}$$

$$c_1 = c_{1,b} + \left(c_{1,a} - c_{1,b}\right) e^{-c_{1,c} i_c} \tag{4.19}$$

$$\beta = \beta_b + (\beta_a - \beta_b)\, e^{-\beta_c i_c} \tag{4.20}$$

$$\gamma = \gamma_b + (\gamma_a - \gamma_b)\, e^{-\gamma_c i_c} \tag{4.21}$$

Table 4.2 Model parameters of the large-scale 200 kN MR Damper

Parameter	Value	Parameter	Value	Parameter	Value
$c_{0,a}$	0.08 kN·s/mm	α_a	0.20 kN/mm	k_0	0.0 kN/mm
$c_{0,b}$	0.32 kN·s/mm	α_b	0.30 kN/mm	k_1	0.0 kN/mm

$c_{0,c}$	1.5 A^{-1}	α_c	1.0 A^{-1}	x_0	0.0 mm
$c_{1,a}$	3.0 kN·s/mm	β_a, γ_a	0.050 mm^{-2}	A	300
$c_{1,b}$	15.0 kN·s/mm	β_b, γ_b	0.002 mm^{-2}	n	2
$c_{1,c}$	2.0 A^{-1}	β_c, γ_c	5.2 A^{-1}		

The MR damper semi-active control is achieved through a primary and a secondary controller. The primary controller calculates a desired damping force for the MR damper based on a structural control law. The secondary controller adjusts the command current sent to the MR damper to achieve the desired force.

Here, a casual model providing rate-independent linear damping (RILD) proposed by Keivan, Phillips et al. (2017) is adopted as the primary controller to determine the desired force for the damper. RILD is proportional to displacement (though out of phase) and therefore provides displacement-proportional damping. It is beneficial for low-frequency structures with large displacement response (e.g. base-isolated structures). As a result, it is selected for the nonlinear structure here, considering the reduction in structural natural frequency and increase in displacement response after initial yielding occurs. A major benefit of the RILD is its similar control performance over displacement and velocity response and substantially improvement in reducing acceleration response for low-frequency structures compared to other damping types. However, the RILD force is proportional to displacement advanced in phase $\pi/2$ radians, a noncausal operation. To implement RILD in real time, the causal realization proposed by Keivan, Phillips et al. (2017) is adopted here.

This casual realization is achieved with a first-order all-pass filter. RILD can be represented in frequency domain with Eq. (4.22), where k is the stiffness between

the two DOFs that the damping component connects, η is the ratio between the loss and storage modulus (i.e. loss factor), ω is the radial frequency and $X(\omega)$ is the relative displacement in frequency domain. The damping force can be further broke down following Eq. (4.23-24). $H_{TF}(\omega)$ represents a transfer function and is taken as a target filter for causal realization of the damping force F_D. This target filter gives a unit magnitude with $\pi/2$ radians phase advance for all positive frequencies, which makes it a non-causal problem. With the first-order all-pass filter given in Eq. (4.25), $H_{TF}(\omega)$ can be approximated over a specified frequency range. As Figure 4.9 shows, the first-order all-pass filter $H_{AP}(\omega)$ keeps the same magnitude as the target filter $H_{TF}(\omega)$, while approximates the phase of $H_{TF}(\omega)$ at/around a specified filter design frequency ω_f. As a result, the causal approximation of the RILD force can be calculated following Eq. (4.26)

$$F_D = \eta k i sign(\omega)\, X(\omega) \tag{4.22}$$

$$F_D = \eta k H_{TF}(\omega) X(\omega) \tag{4.23}$$

$$H_{TF}(\omega) = i sign(\omega) \tag{4.24}$$

$$H_{AP}(\omega) = \frac{i\omega - \omega_f}{i\omega + \omega_f} \tag{4.25}$$

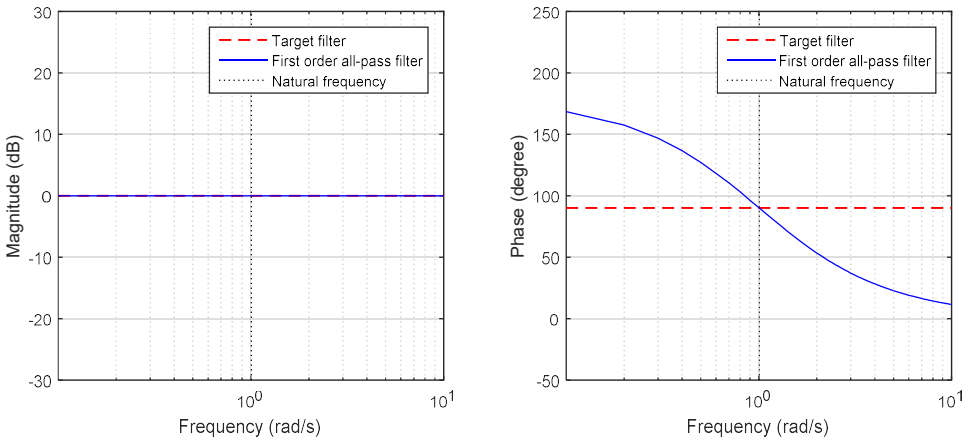

Figure 4.9 Magnitude and phase of the target and all-pass filters

$$F_{D,causual} = \eta k \frac{i\omega - \omega_f}{i\omega + \omega_f} X(\omega) \tag{4.26}$$

The causal approximation of the RILD force (Eq. (4.26)) is taken as the primary controller to provide the desired force for the MR damper. The loss factor η and filter frequency ω_f are the two controller design variables, which controls the magnitude of the hysteresis force and the skew of the hysteresis respectively. Here, ω_f is selected to be the fundamental natural frequency of the structure for the demonstrative case study, due to its best match between the causal approximation (Eq. (4.26)) and the target non-causal RILD (Eq. (4.22)) under linear structural responses. However, the selection of ω_f is not straightforward when structural behaves nonlinearly or under significant forced vibration away from its fundamental natural frequency. Eq. (4.26) provides hysteresis with a positive skew when the structural response first frequency exceeds ω_f, while a negative skew when the structural response frequency is below ω_f. Therefore, the optimization on the controller design variables is considered for optimization in Chapter 6.

In addition, the displacement input to the primary controller above is first filtered using a 2-pole Butterworth high-pass filter with a cutoff frequency of 0.1 Hz. This filter eliminates the influence of residual drifts on the calculation of the control force (Eq. (4.26)). The phase shift caused by the high-pass filter is then compensated by reducing ω_f of the primary controller by 20%, achieving the overall phase lead of $\pi/2$ radians.

The secondary controller is to control the MR damper input current to achieve the desired force approximated by the primary controller. An over-driven back-driven clipped-optimal controller (ODBDCO) developed by Phillips, Jiang et al. (2010) is selected here for its accurate tracking performance. It is built upon a clipped-optimal control (COC) algorithm (Dyke, Spencer Jr et al. 1996) with an over-driven back-driven concept to achieve faster matching of the desired control force. The over-driven back-driven matching is realized through varying the input current to the MR damper between 0 Amps to 2.5 Amps (to avoid overheating of the MR damper coils) with a feedback loop. When the matching error in force is greater, more current is applied. A rate limiter is added to prevent oscillations in the MR damper force from rapidly changing current.

4.3.3 Actuator identification and control

For the actuator control, the dynamics of the servo-hydraulic actuator with the large-scale MR damper specimen are identified through the system response under a 0-30Hz band-limited white noise input, with both passive-off (0 Amps) and passive-on (2.5 Amps) damper condition. System identification is performed with a nonparametric technique MFDID (Kim, Spencer Jr et al. 2005) by fitting the experimental data to a single-input single-output (SISO) model and then obtaining its

poles and zeros. An averaged transfer function from the two fitted results (passive-on and passive-off cases) is taken for approximation of the actuator with MR damper under semi-active control (0-2.5 Amps). Eq. (4.27) gives the obtained average transfer function, and Figure 4.10 shows its approximation performance over the desired frequency range (0-10 Hz).

$$G_{xu} = \frac{1.526 \times 10^5}{(s^2 + 10.38)(s^2 + 202.6s + 1.416 \times 10^4)} \tag{4.27}$$

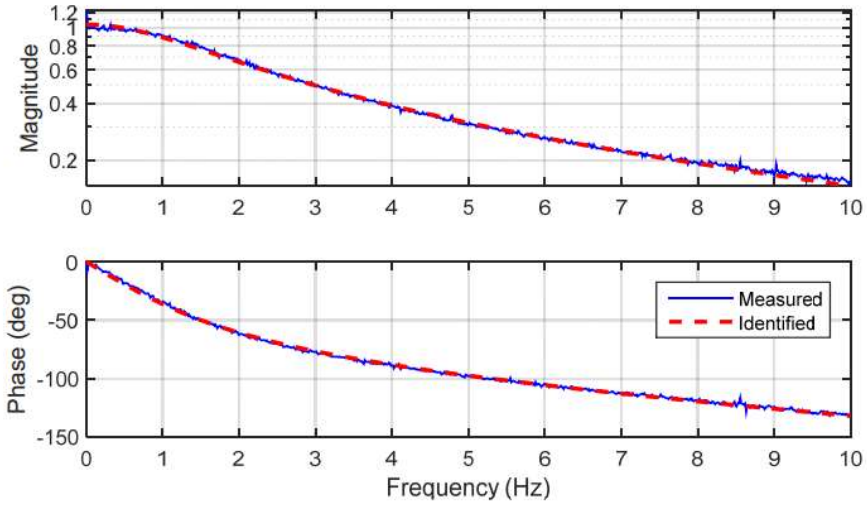

Figure 4.10 Measured and identified transfer function of the actuator with MR damper under semi-active control

With the identified actuator transfer function, a model-based feedforward controller (Phillips, Takada et al. 2014), based on inversing the identified substructure transfer function (Eq. (4.27)) to cancel the substructure dynamics, is implemented with favorable tracking performance. For the identified model (Eq. (4.27)) with 3 poles and no zeros, direct inversion requires the calculation of displacement, velocity, acceleration, and jerk (derivative of acceleration). Here, the high-order derivatives are estimated using the central difference method (CDM) with linear acceleration extrapolation (Phillips 2012). The obtained feedforward controller for the actuator

model is given in Eq. (4.28), where x_i is the desired displacement from numerical integration at time step i, and $u_{FF,i}$ is the actuator command sent to the servo-controller to achieve the desired displacement.

$$u_{FF,i} = 6.4004 \times 10^4 x_i - 1.8589 \times 10^5 x_{i-1} + 1.7999 \times 10^5 x_{i-2} - 5.8102 \times 10^4 x_{i-3} \quad (4.28)$$

4.3.4 Selection of earthquake records

For the IDA process, a suite of ground motions need for the design seismic hazard level. According to ASCE/SEI 7-10 (ASCE 2010) standard, a minimum of 7 ground motions compatible with the geotechnical profile and earthquake intensity at the building location need to be considered. In this case study, a suite of 20 ground motions (LA01-20), developed with a variation of amplitude and frequency content by Somerville (1997) from fault-parallel and fault-normal orientations of 10 earthquake records, is selected. They are corresponding to a seismic hazard level with 10% probability of exceedance in 50 years for Los Angeles, California. For the considered 3-story steel moment frame in this case study, the IM is selected as the 5% damped spectral acceleration at the first mode period ($Sa(T_1, 5\%)$) of the structure, which is suitable for first mode dominated structures (e.g. low- to mid-rise buildings) (Vamvatsikos and Cornell 2002). Following ASCE/SEI 7-10 (ASCE 2010), the mean spectrum of the selected ground motion suite overall matches the design spectrum of the building around its natural period T_1 ($0.2T_1 - 1.5T_1$). Figure 4.11 shows the 5% damped spectral accelerations ($Sa(T_1, 5\%)$) of LA01-20 ground motions with their mean spectrum compared to the design spectrum for the seismic hazard level at probability of exceedance 10%/50 years at LA. The design spectrum is obtained

based on the ground motion parameters from the unified hazard tool (v 4.1.1) of USGS (USGS 2014), under the assumption of site class D. The natural period T_n of the 3-story steel moment frame is 0.9935 s. The corresponding design spectral acceleration obtained from the design spectrum is $0.7251g$ for the design hazard level of 10% probability of exceedance in 50 years, where the gravity acceleration $g = 9.81\, m/s^2$.

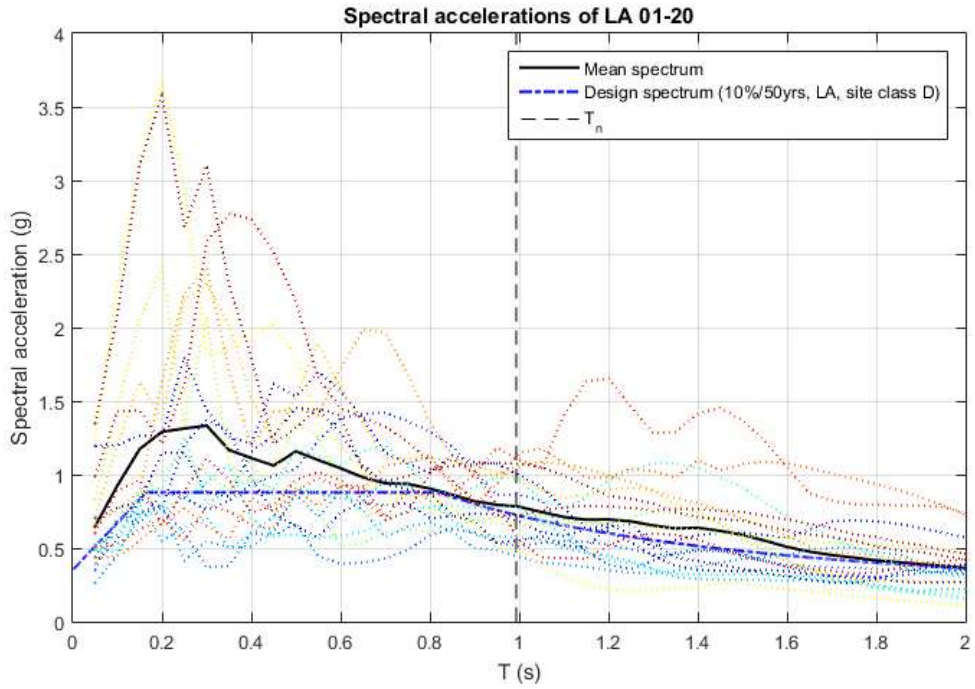

Figure 4.11 LA01-20 spectrum accelerations and design spectrum at LA (site class D)

4.3.5 Actuator limit and MLE for a truncated distribution

Figure 4.12 shows the achievable MTS actuator capacity bounded by the servo-valve limit, MR damper rating, and supply limit. Based on the MTS actuator capacity limit, it has a varying velocity limit regarding varying level of actuator force. For safety concerns, the input displacement to the actuator is scaled down from full scale as needed for the initial test to stay below the velocity limit when integrating

RTHS into the IDA process (discussed in Section 4.2). The MR damper reaction force is then scaled up with a pre-defined gain factor before feedback to the full-scale numerical substructure. The amount of displacement and force scaling depends on the configuration of the structure and will be discussed for each case. An additional velocity safety limiter is also added to attenuate the command displacement sent to the servo-controller to zero when actuator velocity limit is exceeded. The same setting is applied to the full numerical model to keep consistency for comparison purpose.

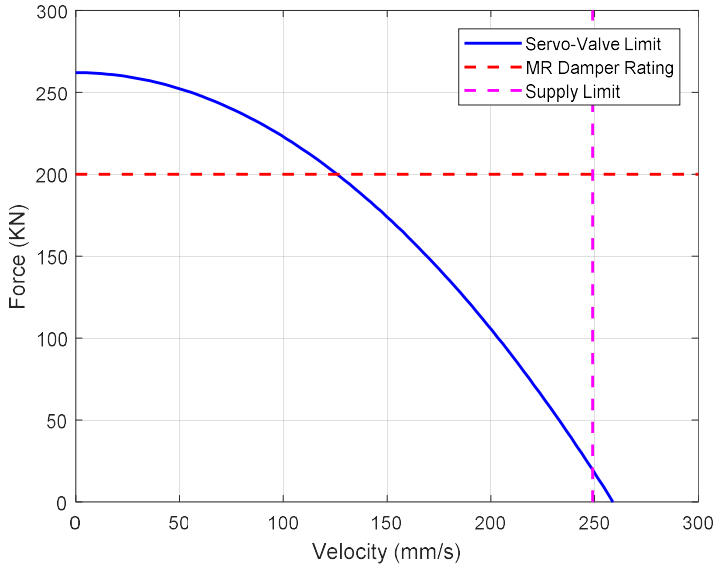

Figure 4.12 MTS actuator capacity limit

Due to this actuator velocity limitation, the maximum scaling of ground motions may still be limited even with the downscale of MR damper inputs. As a result, the damage states (especially the complete damage states) may not be reached for all input ground motions. Note that this may not be a problem for experimental laboratories with higher actuator/damper capacities. Here, to ensure full damage states (total of 12 DS) are reached for all ground motions, it requires back and forth

trial runs to determine all the scaling, which is a non-efficient process and may lead to excessive down scaling of the input displacement that may be problematic for actuator control under vary low intensity/response levels. Here, the MLE discussed in Section 4.1.2 is adapted with a switch to a truncated distribution function when the damage states are not all reached for all ground motions. The truncated distribution function is defined through normalizing the probability density function with the truncated cumulative probability density to ensure it integrates to unity. The corresponding likelihood function for the truncated distribution is given in Eq. (4.29), where m is the number of ground motions that reaches the specific DS and IM_{trunc} is the maximum intensity measure of the scaled ground motions in the IDA process. Then, the moments of the lognormal distribution can then be estimated through maximizing the likelihood function following Eq. (4.11). With the above discussed truncated MLE, a good approximation of the cumulative probability densities can be obtained based on the observed IDA data.

$$Likelihood_{trunc} = \prod_{i=1}^{m} \left[\Phi\left(\frac{\ln\left(IM_{DS,i}/\theta\right)}{\beta}\right) \Big/ \int_0^{IM_{trunc}} \Phi\left(\frac{\ln(x/\theta)}{\beta}\right) dx \right] \quad (4.29)$$

4.3.6 Seismic resilience evaluation

Following Section 4.3.1-4.3.5, the seismic resilience evaluation framework introduced in Section 4.1-4.2 is initially implemented on the 3-story steel moment frame with additional damping from MR damper (applied between base and first floor) and the results are presented herein for both the framework with RTHS integrated and the full numerical model. For the primary controller, the two controller design variables, loss factor η and filter frequency ω_f, is selected to be 0.6 and the fundamental natural frequency (1.0065 Hz) of the linear structure. As discussed in

Section 4.3.5, the input displacement/velocity is scaled down to 5% of the full scale to ensure equipment safety. Then, the gain factor of MR damper force before feedback to the numerical substructure is set as 30 for its adequate reduction on structural response under unscaled intensities of the ground motions.

The comparison between RTHS integrated results and that from full numerical model are conducted for the case with MR damper in passive-off and semi-active mode. A step size of 0.2 intensity scale is selected here for the incremental intensity scale of the IDA process, which is observed with adequate capture of the structural behavior variance over the considered intensity range. The IDA process is scaled up to three times intensity of the original earthquake record for the initial test. For the epistemic uncertainties in the estimated structural response threshold of damage states $\beta_{M,DS}$, it is taken as 0.4 for structural system, 0.5 for drift-sensitive nonstructural components and 0.6 for acceleration-sensitive nonstructural components as per HAZUS loss estimation model (MRl 2003).

Figure 4.13 shows the IDA curves obtained for the case with MR damper in passive-off mode, from RTHS integrated framework and simulation of full numerical model. Disagreement is observed between the results from RTHS integrated framework and that from full numerical model, especially at higher intensities with larger responses. It suggests that the MR damper numerical model may represent the actual response of the physical MR damper with relatively less accuracy at large response magnitudes, where the structure behaves with more nonlinearity and may be outside of the displacement/frequency range from which the MR damper phenomenological model was calibrated. Similar discrepancy can be found between

RTHS integrated framework and full numerical model for the case with MR damper in semi-active mode as well (Figure 4.14).

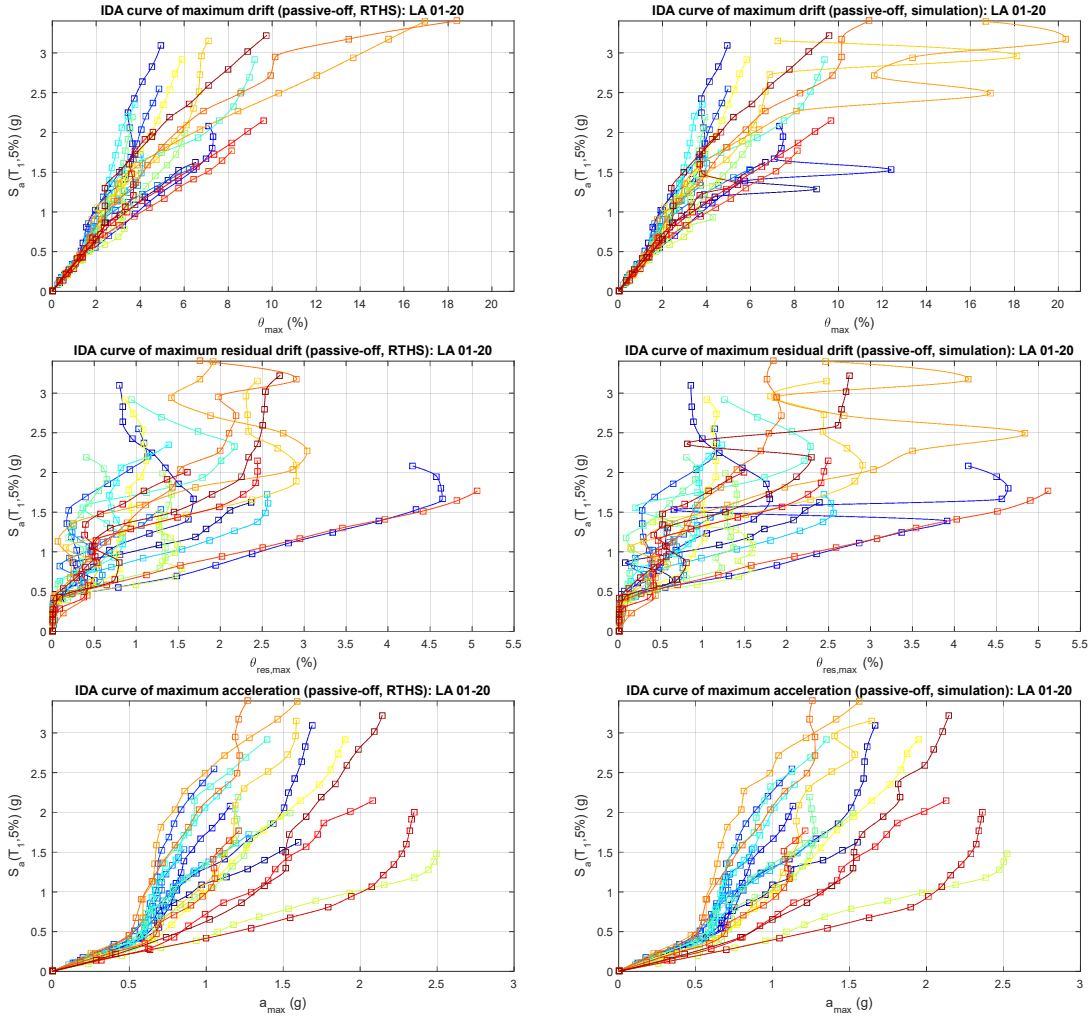

Figure 4.13 IDA curves (top: θ_{max}, middle: $\theta_{res,max}$, bottom: a_{max}) from RTHS integrated framework (left) and simulation of full numerical model (right), for the case with MR damper in passive-off mode

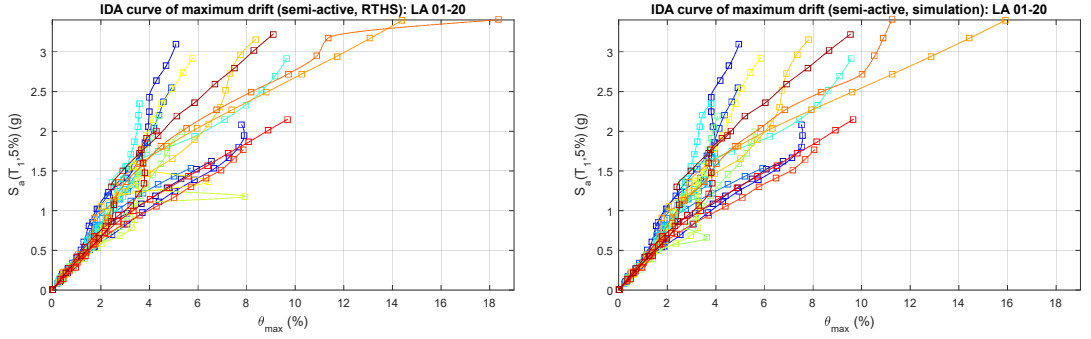

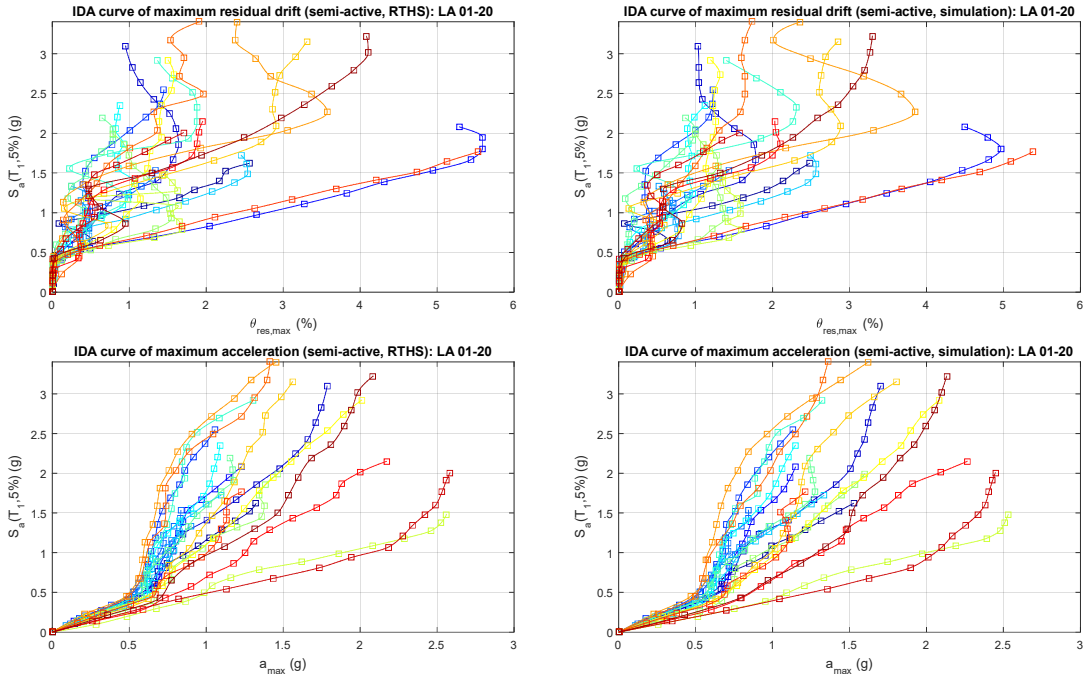

Figure 4.14 IDA curves (top: θ_{max}, middle: $\theta_{res,max}$, bottom: a_{max}) from RTHS integrated framework (left) and simulation of full numerical model (right), for the case with MR damper in semi-active mode

Based on the obtained IDA curves, the intensity measures (5% damped spectral acceleration S_a) at the thresholds (limit states) of the damage states defined in Figure 4.4 can be found through interpolation and used for the construction fragility curves. Note that for structural damage states with limit states defined with both peak inter-story drift and peak residual inter-story drift, the one with lower damage measure value governs. For this initial IDA test with scaling up to three times intensity of the original ground motions, some higher damage states (ED, CD) are not reached in all 20 ground motions. For CD of acceleration-sensitive nonstructural components, the structure under only one ground motion reaches the CD limit states. As a result, CD of acceleration-sensitive nonstructural components is excluded for the fragility and resilience evaluation due to lack of samples collected in that damage state.

To construct fragility curves based on the intensity measures at limit states obtained from the IDA curves, MLE is used to estimate the moments of the lognormal distribution as discussed in Section 4.1.2. For the damage states with the structure under partial of the 20 ground motion reaches, the truncated likelihood function (Eq. (4.29)) is adopted instead of the original likelihood function (4.11). Figure 4.15 shows two examples on the MLE approximation of CD fragility curve based on the partial observed data (out of 20 ground motions, 6 reached structural CD and 12 reached drift-sensitive nonstructural CD), which demonstrates adequate approximations based on the observed data.

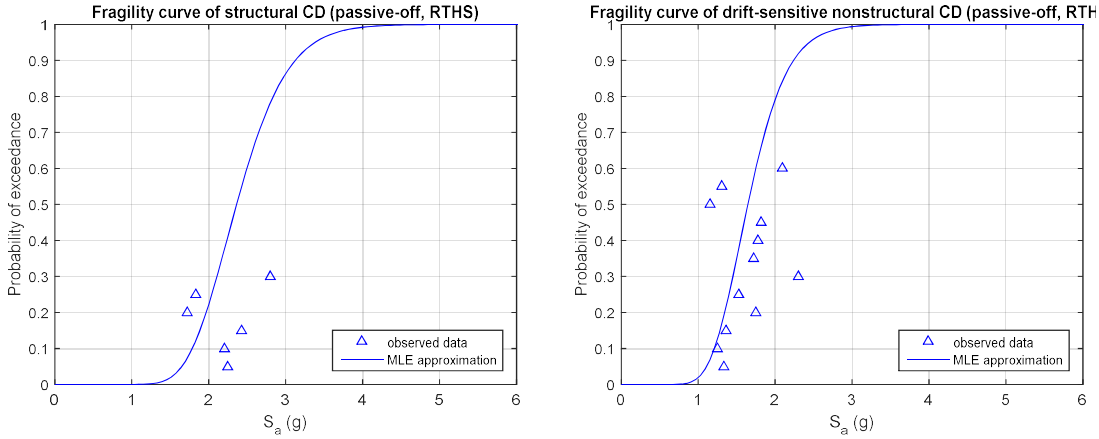

Figure 4.15 MLE on truncated distributions on structural CD (left) and drift-sensitive nonstructural CD (right) for the case with MR damper in passive-off mode using RTHS integrated framework

Figures 4.16-4.18 summarize the MLE estimated fragility curves of different damage states based on the IDA results from both RTHS integrated framework and simulation with full numerical model, for the case with MR damper in passive-off and semi-active modes. It can be seen that the full numerical model has a good representation of the actual system behavior at damage states with smaller responses, while relatively less accurate at more severe damage states with larger responses and

more nonlinearities in the system. The reduction in accuracy is observed for the structural CD and acceleration-sensitive nonstructural ED. Note that acceleration-sensitive nonstructural CD is omitted in the construction of fragility curves due to lack of sufficient samples.

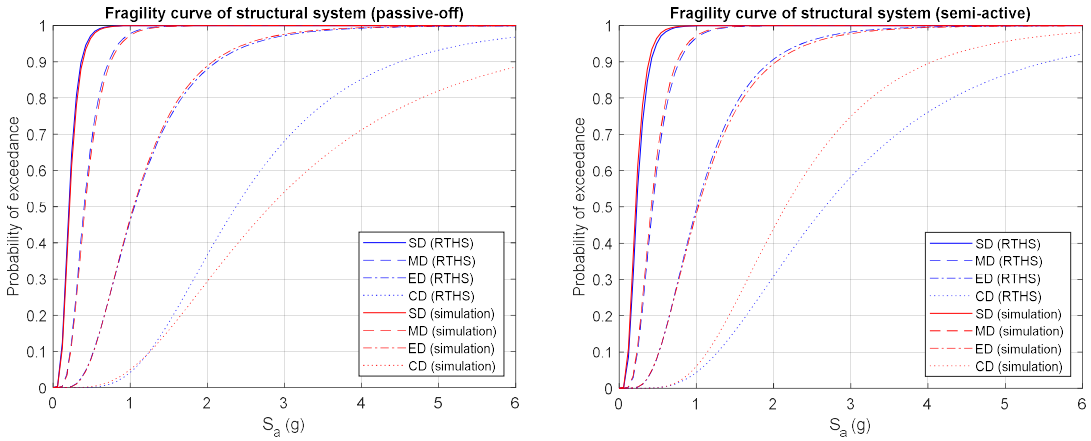

Figure 4.16 Fragility curves of structural damage states for the case with MR damper in passive-off mode (left) and semi-active mode (right)

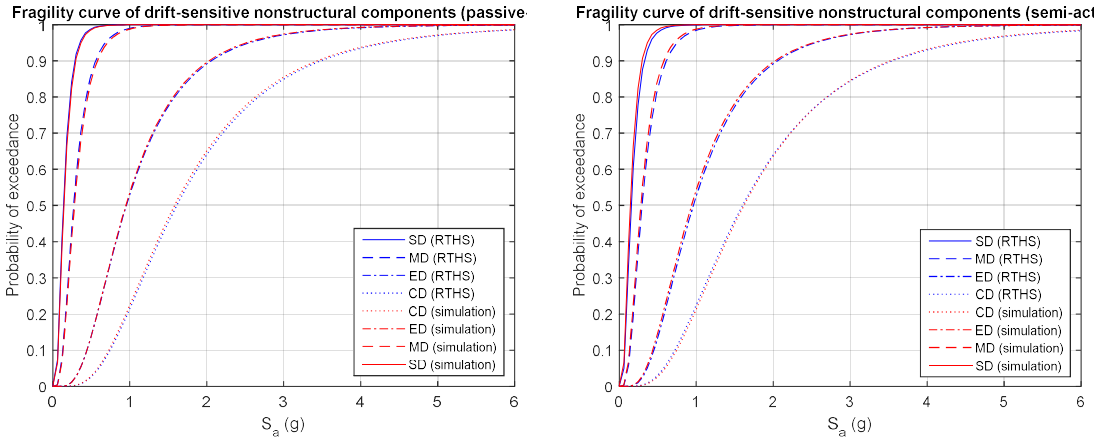

Figure 4.17 Fragility curves of drift-sensitive nonstructural damage states for the case with MR damper in passive-off mode (left) and semi-active mode (right)

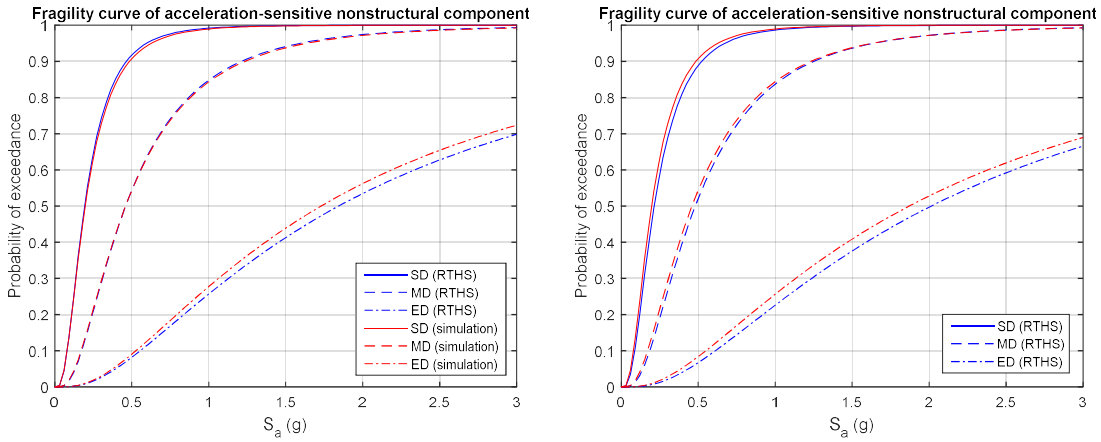

Figure 4.18 Fragility curves of acceleration-sensitive nonstructural damage states (CD excluded due to insufficient observed data) for the case with MR damper in passive-off mode (left) and semi-active mode (right)

With the constructed fragility curves, the probabilities of exceeding different limit states (i.e. damage states probabilities) at the design spectral acceleration under considered seismic hazard level (probability of exceedance of 10%/50 years) are estimated. The seismic loss and recovery function are then determined following Section 4.1.1 using Eqs. 4.3-4.9. At last, the resilience index and graph are generated with Eq. (4.1-4.2). Figure 4.19 shows the seismic resilience graphic comparison between the evaluations conducted with the RTHS integrated framework and full numerical model, for the cases with MR damper in passive-off and semi-active modes. The full numerical model provides underestimation on the structural seismic resilience in both passive-off and semi-active cases.

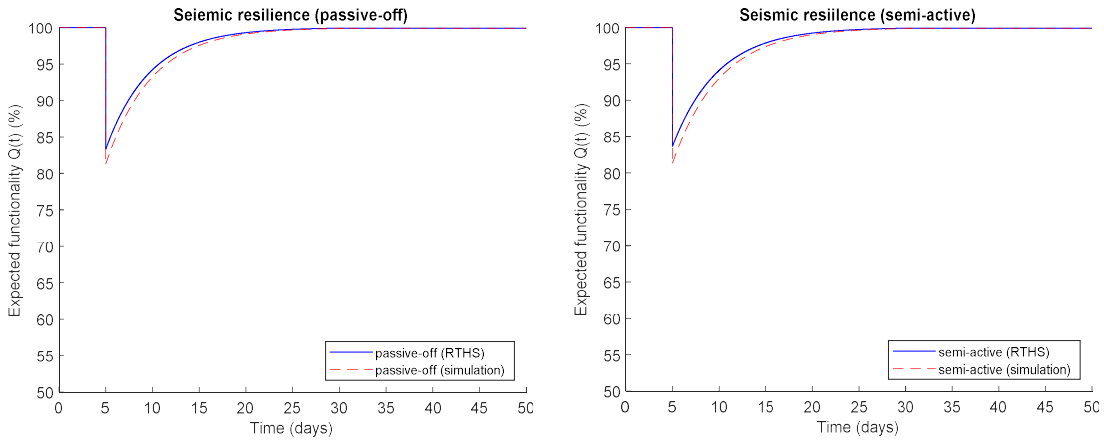

Figure 4.19 Seismic resilience of the case with MR damper in passive-off mode (left) and semi-active mode (right): comparison between results from RTHS integrated framework and simulation with full numerical model

Table 4.3 summarizes the detailed results from the seismic resilience evaluation, where the uncontrolled case evaluated with full numerical modal is also included for comparison. The uncontrolled case here stands for the moment frame structure without supplemental control using MR damper. It can be seen that the largest discrepancy between the evaluation results from simulation with full numerical model and the RTHS integrated framework is 2.34% in seismic loss, 1 day in recovery time and 0.47% in resilience index. Although the difference in resilience index and recovery time is not obvious, the seismic loss estimation based on simulation results possess largest percentage errors of 14% comparing to the RTHS results. Considering the larger discrepancy observed at higher intensities and larger responses, such error may increase when nonstructural acceleration-sensitive CD damage state is included and when under a higher hazard level (e.g. 2%/50 years probability of exceedance). In other words, although the adopted MR damper numerical model performed with reasonable accuracy under the current hazard level, its accuracy may decrease under higher ground motion intensities with conditions that

are out of the model calibration range (i.e. range of displacement and velocity). The results discussed above suggest that the evaluation accuracy could be improved with the RTHS integrated framework, especially for newly developed structural component or damping devices without available/reliable numerical models.

Table 4.3 Seismic resilience evaluation results for the 3-story moment frame with additional MR damper under 10%/50 years hazard level

Case	Uncontrolled	Passive-off (simulation)	Passive-off (RTHS)	Semi-active (simulation)	Semi-active (RTHS)
Seismic loss (L)	20.84%	18.75%	16.70%	18.69%	16.35%
Recovery time (T_{RE})	31 days	26 days	25 days	27 days	26 days
Seismic resilience index (R)	96.09%	96.48%	96.86%	96.49%	96.93%

Comparing to the uncontrolled case, passive-off (RTHS) case illustrates 4.14% and 6 days reduction in seismic loss and recovery time respectively, providing a 0.77% improvement in seismic resilience. Semi-active (RTHS) case provides 4.49% and 5 days reduction in seismic loss and recovery time respectively, resulting in a 0.84% incensement in seismic resilience. The semi-active cases shows almost negligible improvement from the passive-off case, which reveals that the initially selected MR damper control parameters may not be optimal under the seismic resilience evaluation, though they provide adequate improvement in structural response control under the ground motions at original intensities. Also, this could be due to that the current moment frame structure design may not be favorable for semi-active control application. Figure 4.20 presents the comparison of seismic resilience graph between uncontrolled, passive-off and semi-active cases, from which the same

conclusion can be draw. Therefore, an optimization process may be needed when designing for the much complex scenarios to integrate seismic resilience concept. Such optimization process will be explored and discussed in Chapter 5.

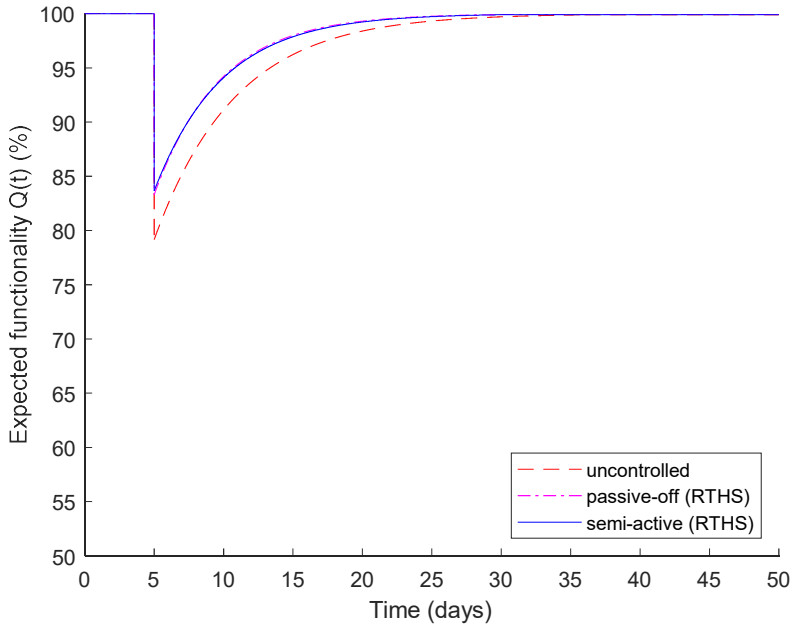

Figure 4.20 Seismic resilience comparison between uncontrolled (simulation), passive-off (RTHS) and semi-active (RTHS) cases

4.4 MGSS-IDA for Fragility Analysis with Improved Efficiency

A major drawback appeared in the IDA based resilience evaluation process discussed in previous sections is the large computational effort (large number of nonlinear time history analysis) needed to collect the IM levels corresponding to interested limit states. This is exacerbated by the RTHS integrated framework due to the experimental tests required for each analysis. In this section, a modified golden section search algorithm (MGSS) for more efficient IDA is developed to improve

computational efficiency for the fragility analysis, applicable for either the implementation with full numerical model and the RTHS integrated framework.

4.4.1 MGSS-IDA algorithm

As introduced in Section 2.4.1, the golden section searched (GSS) algorithm provides a simple and computational efficient way to approach the optimal solution within a unimodal and one-dimensional search space $[a_i, b_i]$. Figure 4.21 illustrates the basic iteration of the GSS from iteration step i to step $i+1$, with two evaluation at initial step but only one new evaluation at following steps by overlapping one of the intermediate points from previous step. Such overlapping is achieved through the section division with the golden ratio $\varphi = 0.618$. Here, the search space refers to the IDA curve and the optimal solution represents the lowest IM level that triggers the limit state of interest. The search space of the IDA curve is one-dimensional and a globally monotonic pattern, however, can exhibit locally non-monotonic behavior. This local weaving pattern is caused by kinematic hardening, which can be observed in Figures 4.12-4.13. Because IDA curves are not necessarily unimodal, they differ from the problem that GSS is designed to solve. Therefore, some modification is introduced to the traditional GSS to better tackle the problem in this study.

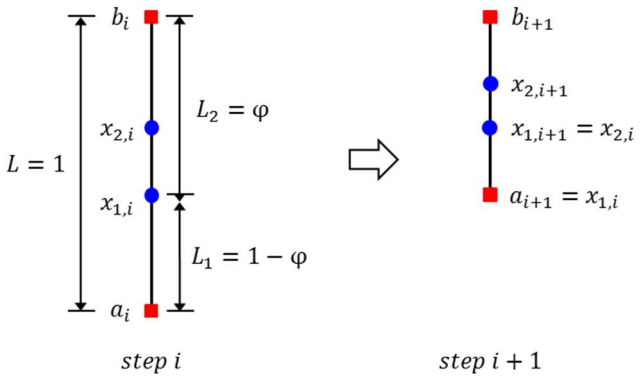

Figure 4.21 Basic GSS iteration

For the MGSS-IDA algorithm proposed here, the search space is a portion of the IDA curve with end points that include the IM that reaches the damage state (DS) of interest as indicated by the damage measure (DM). Through the MGSS algorithm, the search space will be iteratively reduced. The IM value can then be interpolated from the search space similarly as that of the IDA process. The MGSS-IDA objective function (Eq. 4.30) to minimize for a given DS is defined in terms of the range in IM of the evaluated intermediate section at each step i. In the meanwhile, the error in DM at the two end points ($x_{1,i}$ and $x_{2,i}$ shown in Figure 4.21) at each step i (Eqs. 4.31-32) is also recorded. Additionally, with the goal of enclosing the target IM between the two end points $x_{1,i}$ and $x_{2,i}$, the convergence criteria of the MGSS-IDA is defined with constraints and objective function, in terms of $err_{x_{1,i}} \leq 0$, $err_{x_{2,i}} \geq 0$ and $f_{obj} < f_{tol}$, where f_{tol} is the tolerance in the increment of IM from $x_{1,i}$ to $x_{2,i}$. With the multiple criteria for convergence, most of the converged sections actually possess much smaller f_{obj} value than the pre-defined f_{tol} value. Considering that the traditional IDA is conducted with 0.2 intensity scale in this study, f_{tol} is taken as 0.25 intensity scale here for faster convergence with an overall similar level of increment for interpolation.

$$f_{obj} = \left| IM_{x_{1,i}} - IM_{x_{2,i}} \right| \tag{4.30}$$

$$err_{x_{1,i}} = DM_{x_{1,i}} - DM_{DS} \tag{4.31}$$

$$err_{x_{2,i}} = DM_{x_{2,i}} - DM_{DS} \tag{4.32}$$

Unlike the traditional GSS algorithm narrowing the search space by updating one of the boundary points (a and b) with the intermediate point (x_1 or x_2) having larger objective function value, the proposed MGSS-IDA updates the search space

conditionally. The boundary updating procedure can be summarized for 4 different conditions as follows:

(1) When $err_{x_{1,i}} \leq 0$ and $err_{x_{2,i}} \leq 0$, $a_{i+1} = x_{1,i}$;

(2) When $err_{x_{1,i}} \leq 0$ and $err_{x_{2,i}} \geq 0$, $b_{i+1} = x_{2,i}$;

(3) When $err_{x_{1,i}} > 0$ and $err_{x_{2,i}} < 0$, $b_{i+1} = x_{2,i}$;

(4) When $err_{x_{1,i}} \geq 0$ and $err_{x_{2,i}} \geq 0$, $b_{i+1} = x_{2,i}$.

One thing to note is that MGSS-IDA narrows the search space predominately by updating the higher boundary, rather than updating nearest boundary with the intermediate point the having larger objective function value as with the traditional GSS. This modification is to conservatively approach the lowest IM that reaches the considered DS by keeping the lower portion of the search space and avoid being misled by local weaving of the IDA curve. Another point to note is condition (3), which is the case capturing the local hardening portion of the IDA curve. In this case, the larger IM level is paired with the smaller DM level, and the lowest IM level reaching the considered DS is actually located within section $[a_i, x_{1,i}]$ which is below the intermediate section $[x_{1,i}, x_{2,i}]$. Here, the boundary is narrowed by updating $b_{i+1} = x_{2,i}$ for condition (3), for keeping the efficiency of the traditional GSS by reusing $x_{1,i}$ as $x_{2,i+1}$.

MGSS-IDA conditions can be further explained with Figure 4.22 when there is clear local weaving behavior. This local weaving behavior suggests successive segments of softening and hardening, which is caused by the acceleration/deceleration of DM accumulation rate that may momentarily stop/reverse the DM accumulation (Vamvatsikos and Cornell 2002). Condition (1) and (4) are

relatively straightforward and is not discussed further here. Condition (3) showing in Figure 4.22 represents a possible case caused by the weaving. By updating the next higher boundary b_{i+1} with the lower intermediate point $x_{2,i}$, it is ensured that the search space will always enclose the actual lowest IM value reaching the DS. Assuming the section converging tolerance f_{tol} is adequately small to avoid skipping any major local weaving behavior in the IDA curve, condition (2) is then possible to appear at a lower and a higher location within a local weaving portion for the final IM interpolation. In this case, the lower section is the one to keep as search space. However, it is not guaranteed that the convergence will always occur at the lower section. To address this issue, the section evaluation and target IM interpolation is conducted for all 12 DS when performing searching process for one DS and the corresponding target IM is updated when a lower value is found.

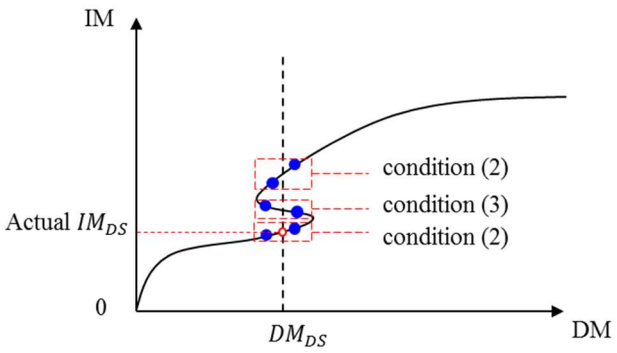

Figure 4.22 MGSS-IDA conditions when there is a local weaving behavior

The search space of each DS needs to be pre-defined with an initial guess. The searching boundary are set to be enlarged by ± 0.5 intensity scale if the intermediate section range has been reduced to less than 0.05 intensity scale and the target IM still has not been found. This condition indicates that the target IM may be out of the initial assigned search space or the search may be trapped by local weaving behavior.

To further reduce the computational demand, the searching process starts with the lowest DS and all the searched points are evaluated and used to narrow the searching boundary of higher DS. Figure 4.23 shows an example of the searching boundary of a higher DS narrowed and updated from the searched points of a lower DS. Note that the section between intermediate points and the updated boundary points is evaluated for target IM interpolation as well to improve searching efficiency and avoid missing lower IM values. Also, the searching for a higher DS is skipped if its target IM value is found during the searching process of a previous lower DS, which further improves the efficiency of MGSS-IDA.

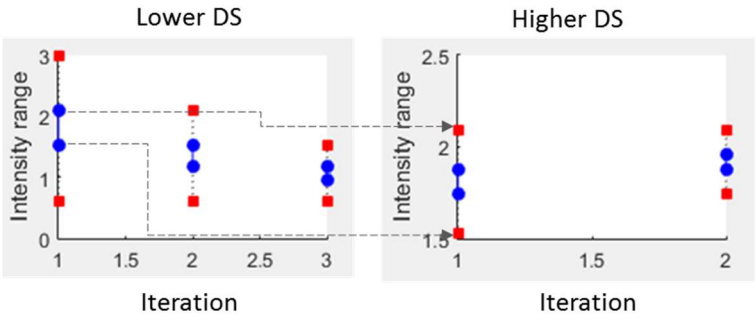

Figure 4.23 Example of searching boundary update during MGSS-IDA process

4.4.2 Efficient seismic resilience evaluation with MGSS-IDA

The proposed MGSS-IDA algorithm is implemented for the same case study under 10%/50years hazard level conducted with IDA in Section 4.3, for the case with MR damper in semi-active mode. The IDA process shown in Figure 4.2 is replaced with MGSS-IDA as Figure 4.24 illustrates. Note that the RTHS component can be replaced with numerical simulation for a fully numerical analysis. Considering the velocity limit of the actuator for future RTHS validation if needed, the input displacement/velocity to the MR damper is scaled to 1% so that the IDA analysis can reach all 12 DS under all 20 ground motions. The gain factor to scale up the damping

force before feedback to the numerical substructure is selected as 50. The MR damper is connected between base and top story, creating a super-brace, to provide better energy dissipation for the fundamental mode of the structure. For the MGSS-IDA search space initialization, the initial lower boundary a_1 is set to zero for all 12 DS, while the initial higher boundary b_1 is set to intensity scale of 1, 2, 4, and 8 for structural (S) SD, MD, ED, and CD, respectively; 1, 1.5, 3, and 6 for drift-sensitive nonstructural (NSD) SD, MD, ED, and CD, respectively; 1, 1.5, 4, and 18 for acceleration-sensitive nonstructural (NSA) SD, MD, ED, and CD, respectively. Note that the intensity scale has to be increased to 18 to achieve acceleration-sensitive nonstructural CD for all 20 ground motions, which will have little impact on losses because due to the low probability of occurrence. These higher intensities may be avoided with a pre-defined maximum intensity scale and MLE for truncated lognormal distribution discussed in Section 4.3.5. Here, the extreme IM scales are included for a full comparison of the target IMs found using IDA and MGSS-IDA.

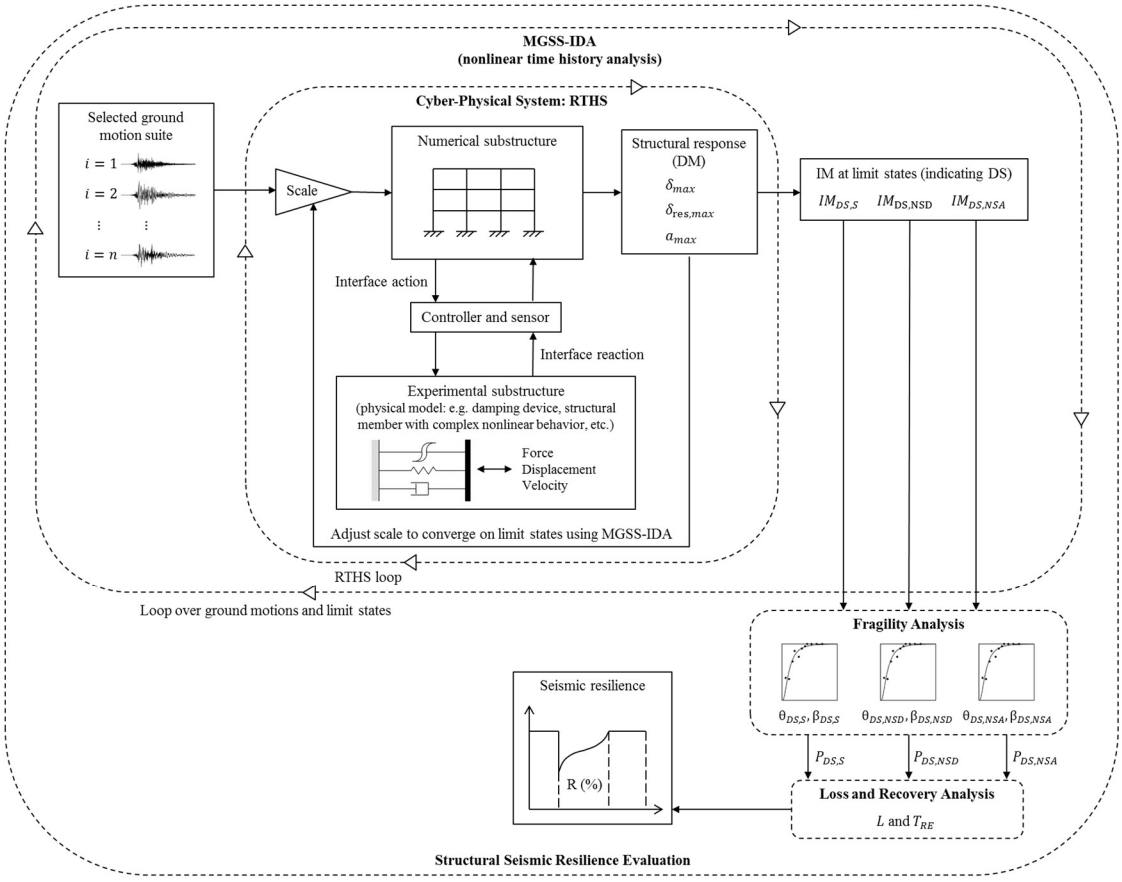

Figure 4.24 Schematic diagram of structural seismic resilience cyber-physical evaluation framework using MGSS-IDA

Here, the performance of MGSS-IDA compared with IDA is conducted through simulation with full numerical model for efficiency. Figure 4.25 shows the comparison between the MGSS-IDA searched and IDA interpolated target IM values for each DS. Most of the MGSS-IDA searched target IMs are the similar as IDA interpolated results. Less than five IM found using MGSS-IDA converged to a significantly higher value than that found through IDA. Some IM values found using MGSS-IDA are at lower levels than those found through IDA, which reveals that IDA with fixed incremental steps could possibly skip some small local weaving behavior that reaches the considered DS at lower IM level. The seismic resilience evaluations based on MGSS-IDA and IDA are compared in Figure 4.26, showing a more

conservative assessment on seismic resilience using MGSS-IDA. The detailed seismic resilience evaluation results based on IDA and MGSS-IDA are listed in Table 4.4. The detailed results based on MGSS-IDA and IDA illustrates that IDA provides an underestimation on seismic loss, recovery time, and the resulting seismic resilience index due to the miss on several lower IMs that reaches the considered DS (Figure 4.25).

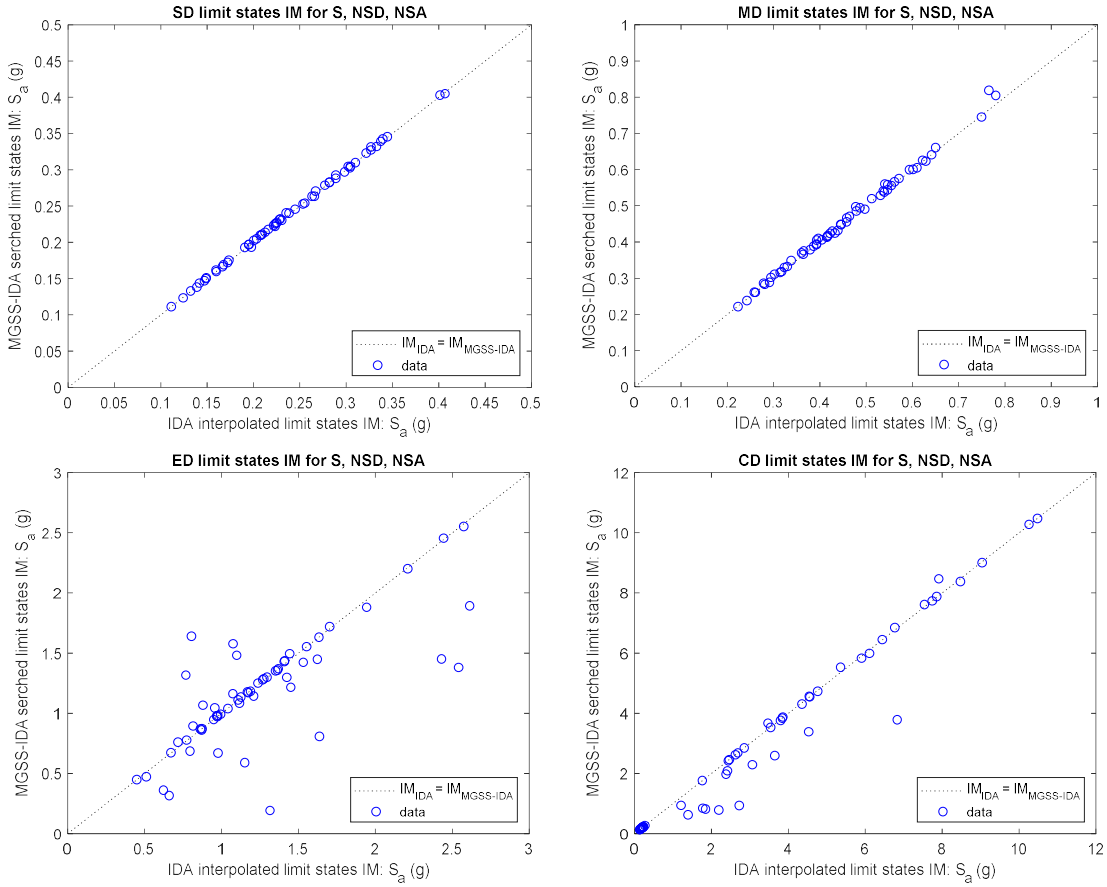

Figure 4.25 Comparison of IDA interpolated and MGSS-IDA found limit state IMs

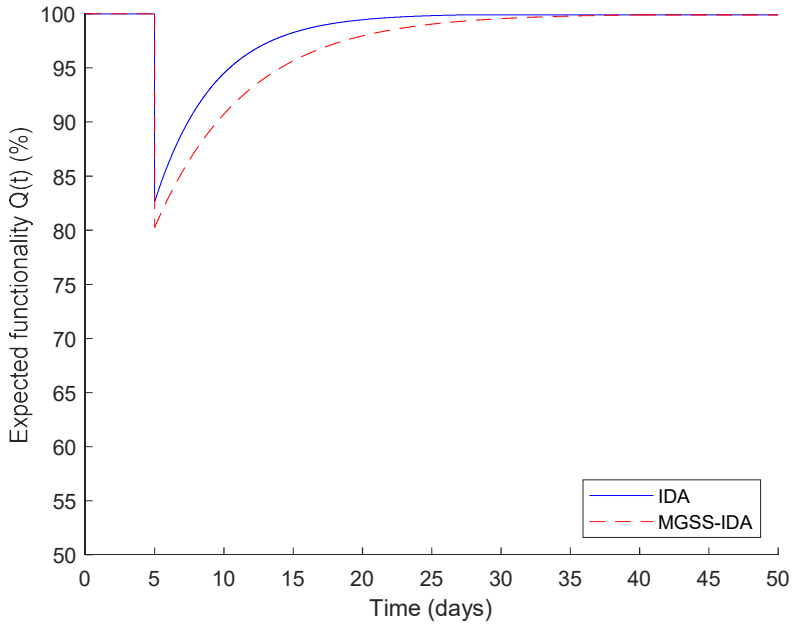

Figure 4.26 Seismic resilience evaluations for semi-active (simulation) case based on IDA and MGSS-IDA

Table 4.4 Seismic resilience evaluation results based on IDA and MGSS-IDA for the 3-story moment frame with additional MR damper in semi-active mode under 10%/50 years hazard level

Case	IDA	MGSS-IDA
Seismic loss (L)	17.38%	19.75%
Recovery time (T_{RE})	23 days	35 days
Seismic resilience index (R)	96.74%	96.29%

For the computational demand, MGSS-IDA takes 626 analyses to find the full target IMs for all 12 DS under 20 ground motion excitations, while IDA requires 1800 analyses with an incremental step of 0.2 intensity scale. Table 4.5 presents the improvement on computational efficiency of MGSS-IDA compared to IDA. Overall, MGSS-IDA demonstrated comparable or even increased accuracy in detecting limit states IM levels with considerably improved efficiency compared to IDA. Therefore,

further studies requiring seismic resilience evaluation in this dissertation will adopt MGSS-IDA instead of the traditional IDA process.

Table 4.5 Computational demand of the seismic resilience evaluation based on IDA and MGSS-IDA for the case study

Case	IDA	MGSS-IDA
Number of analysis performed	1800	626
Normalized computational time	100%	35%

4.5 Summary

This chapter proposed a cyber-physical structural seismic resilience evaluation framework by integrating RTHS. This framework is developed based IDA, fragility analysis, loss, and recovery analysis. A case study of a 3-story steel moment frame with MR dampers providing supplemental control is conducted to illustrate the proposed framework. The evaluation is performed with both the RTHS integrated framework and with a fully numerical model. The structural seismic resilience evaluation with RTHS exhibits improved accuracy compared to that with fully numerical model. This proposed framework provide an effective tool to evaluate the seismic resilience of structural systems with highly nonlinear or rate dependent components that may rise concerns to model numerically.

Furthermore, this chapter developed a MGSS-IDA algorithm to augment the traditional IDA process with improved efficiency. Through comparison MGSS-IDA and IDA performance on the case study, MGSS-IDA demonstrates comparable or even increased accuracy and considerably reduced computational demand compared to IDA. The developed MGSS-IDA enables a much faster seismic resilience

evaluation, and sets the stage for more efficient structural optimization on seismic resilience which will be discussed in Chapter 6.

CHAPTER 5 STRUCTURAL OPTIMIZATION OF SEISMIC RESILIENCE USING NEURAL NETWORKS

In this chapter, a novel structural seismic resilience optimization approach is proposed based on the framework proposed in Chapter 4. Multi-layer feedforward neural networks are introduced for the metamodeling of the IDA-based fragility analysis to enable a computationally-efficient optimization process. The heuristic PSO algorithm is adopted for the optimization problem, suitable for systems with complex non-deterministic behavior. A case study is conducted on the BMJ bracing system proposed in Chapter 3, under a 10%/50 years seismic hazard level for optimization of seismic resilience. The case study demonstrates the potential for fragility metamodeling using deep neural networks to improve the efficiency of structural seismic resilience design and optimization.

5.1 Background

Structural optimization can be used to automate a complex design process to reach an optimal design through mathematical programming, instead of a traditional design approach with trial and error methods. This is especially valuable for the design problem subjected to complex conditions that requires leveraging multiple design variables and performance trade-offs. With the development of performance-based design and reliability-based design, the structural design problem becomes even more complex, combining multiple performance objectives under large uncertainties. Here, the seismic resilience index provides a lumped measure on the structural and nonstructural seismic performance, post-event recovery, and economic

losses. Maximizing seismic resilience as the optimization objective naturally incorporates multiple design objectives into a single index with intrinsic weights based on probabilities and losses.

One of the major challenges in structural optimization of nonlinear structures is the high computational cost due to the large number of iterations required. The computational cost is further increased when the optimization objective is seismic resilience, which requires a considerable amount of nonlinear analyses at each iteration (e.g., IDA) during the optimization process. To address this challenge, this study proposed an efficient structural optimization approach based on the seismic resilience evaluation framework introduced in Chapter 4. Metamodeling of the computationally intensive IDA-based fragility analysis using deep neural networks is developed here to overcome the barriers of the large computational demand and enable a rapid optimization approach for seismic resilience.

5.2 Methodology

The optimization of seismic resilience is a complex non-deterministic problem due to the large uncertainties included. Therefore, the heuristic PSO algorithm is selected for the optimization algorithm and is discussed in this Section. A flowchart illustrating the overall procedure is given in Figure 5.1. It starts with identifying the design variables under optimization, following two major groups of process: fragility metamodeling with neural networks and PSO using the NN fragility metamodel (NN-PSO). The PSO process with possible integration of cyber-physical systems is first introduced. Furthermore, fragility metamodeling with neural networks is explored to

provide rapid IDA/MGSS-IDA analysis enabling a much more efficient optimization on structural seismic resilience.

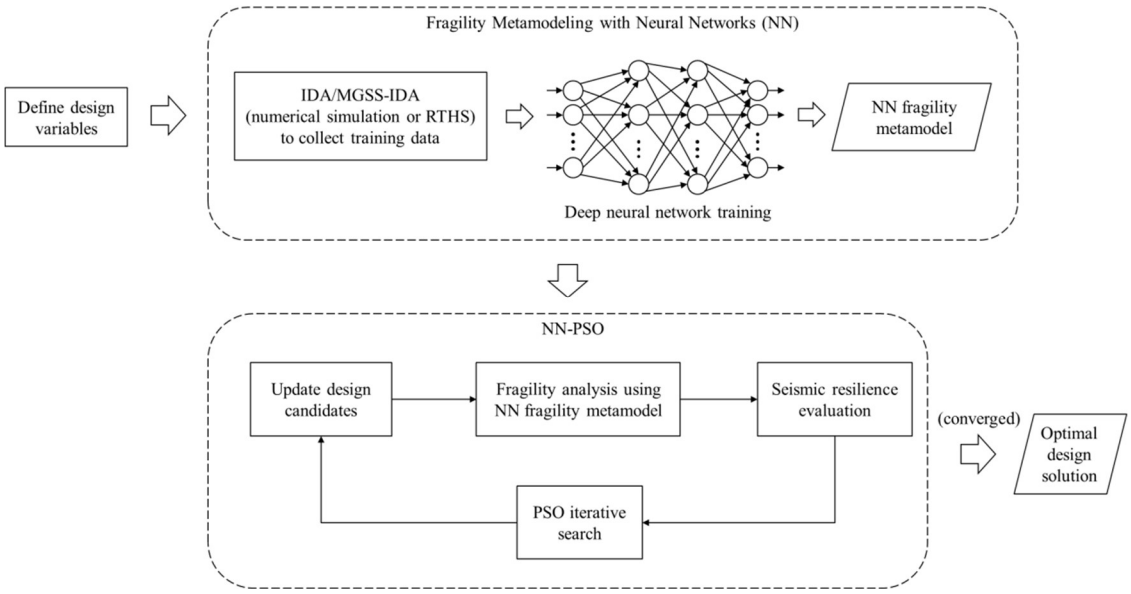

Figure 5.1 High-level flowchart of the optimization procedure

5.2.1 Seismic resilience optimization using PSO

The optimization process on structural seismic resilience is developed based on the PSO algorithm and the structural seismic resilience framework (with or without RTHS integrated) proposed in Chapter 4. The details of the PSO algorithm can be found in Section 2.4.1 with basic equations given in Eqs. 2.11-2.12. The optimization objective is to maximize the resilience index R. The PSO process is set to converge and stop when the normalized absolute gradient of the objective function within last 5 iterations is reduced below the pre-defined tolerance. Note that the converging gradient can be defined with flexible number of iterations depending on the problem (i.e., the objective function may stay stagnant and hard to converge). The convergence tolerance is set as 1×10^{-4} here. Also, the number of iterations is set to

be bounded by a pre-defined maximum iteration number in case there is a convergence problem.

The flowchart given in Figure 5.2 illustrates the structural seismic resilience optimization procedures using PSO. It starts with defining the design variables under optimization and the swarm size for solution searching, of which the search space of the design variables needs to be properly constrained when the structural seismic resilience evaluation framework has RTHS integrated to avoid RTHS instability. The initialization of the particle positions can be random, equally spaced, or following other sampling method over the search space. Here, the initial velocities of the particles and the initial global best are set to be zero and are updated based on the evaluation results at each iteration step. The inertia weight w which influenced the tradeoff between global and local exploration is determined empirically based on the convergence performance regarding the problem; while the acceleration coefficients c_1 and c_2 are empirically set to be 2 (Kennedy 2006).

The optimization objective function (resilience index R) is evaluated at each iteration with the framework (could be pure simulation or integrated with RTHS) proposed in Chapter 5, which is showed as a dashed block in Figure 5.2 and is the essential part that increase the computational cost geometrically. Based on the evaluation results of the particles, a local best L_{best} with the largest R index is updated as the global best G_{best} at each iteration and the movement of the particles for solution searching can be guided (updating their positions and velocities accordingly). After the iterative process converged, the final G_{best} is output as the final solution found by PSO. Note that as a heuristic algorithm, this final solution is

the approximation of the optimal solution in the defined search space and is denoted as the optimal solution here.

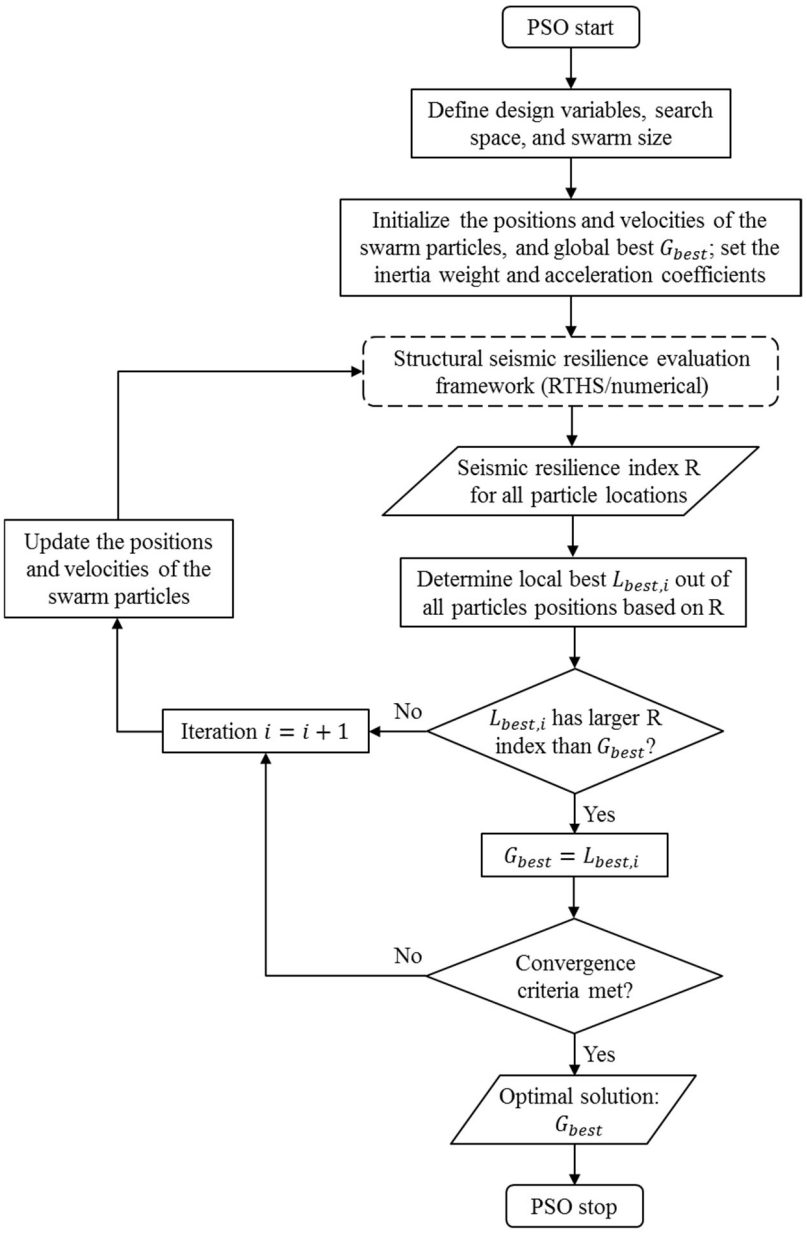

Figure 5.2 Flowchart of structural seismic resilience optimization based on PSO

5.2.2 Fragility metamodeling with neural networks

As discussed above, the structural seismic resilience process shown as the dashed block in Figure 5.2 essentially increase the computational demand

geometrically in the PSO process (i.e. the number of analysis needed will depend on the number of PSO searches times the number of nonlinear time history analysis needed in each seismic resilience evaluation at a single search). To overcome the obstacle of huge computational demand from both the PSO process and the seismic resilience evaluation (i.e., IDA or MGSS-IDA process), a metamodel for the computationally intensive fragility analysis through IDA/MGSS-IDA is developed using deep neural networks in this study. A metamodel is the mapping between inputs and outputs in terms of a closed-form function which can be used to replace the complex and computationally intensive processes or numerical simulations and enable rapid analyses. In this study, the metamodel is intended to replace the structural seismic resilience evaluation (the dashed block shown in Figure 5.2). Therefore, the inputs are considered as the characteristics of the selected ground motion suite (e.g. spectral accelerations at structural natural period) and the design variables; the outputs are considered as the moments of the lognormal distribution used for the fragility curve construction to perform loss/recovery analysis and evaluate the seismic resilience as discussed in Section 4.1. With metamodels mapping between these inputs and outputs, the computationally expensive fragility analysis based on IDA/MGSS-IDA can be avoided and a rapid process for the optimization on seismic resilience can be enabled.

As a powerful tool for input-output nonlinear mapping introduced in Section 2.4.2, deep multi-layer feedforward neural networks are adopted here for the metamodeling that allows rapid optimization. A neural network can be trained with properly sampled data pairs (training set) of inputs and outputs over the PSO searching space to empirically learn the approximated fragility metamodel. The Latin

Hypercube Sampling (LHS) technique (Olsson, Sandberg et al. 2003) is adopted here for its sampling efficiency, especially for a multi-dimensional sampling space. The samples can be collected through the structural seismic resilience evaluation framework based on MGSS-IDA proposed in Chapter 4. For this study, the backpropagation (BP) NN training method is adopted as introduced in Section 2.4.2, which is favorable for function approximation problems. The training is performed using MATLAB. The Levenberg-Marquardt training algorithm is selected for its faster and better performance on function approximation (nonlinear regression) problems (Beale, Hagan et al. 1992). The log-sigmiod transfer function is used for the hidden layers and the linear transfer function is set for the output layer. The specific layer configuration is determined based on the approximation performance of the specific problem.

One of the common problems during neural network training is overfitting, which is due to the trade-off between the goodness of fitting on the seen data set (i.e., the data set used for training) and the prediction error on any unseen data set. The overfitting problem can be mitigated through generalization approaches. The early stopping method is included to avoid overfitting on training set by monitoring the error on a validation set and stop the training iterations when the error on validation set increases for a pre-defined number of iterations. Here, the full data set is randomly divided for training set, validation set, and test set, with the percentage of each data set decided based on the learning task conditions. The test set is used to evaluate the training performance in terms of the mean squared error. In addition, a retraining process is implemented to find a trained network with relatively better generalization, considering that the random data division and random initial weights and biases of the

BP training process leading to different solutions each time. The selection of the trained network with the best generalization is based on the prediction error on the test data set.

5.3 Numerical Case Study

A numerical case study is conducted to demonstrate the proposed NN-PSO approach. The BMJ bracing system proposed in Chapter 3 is considered here for a design optimization on seismic resilience, under a 10%/50 years seismic hazard level.

5.3.1 Structural model and selection of earthquake records

The same structural model of the 3-story steel braced frame (Figure 5.3) considered for the design of BMJ bracing system in Section 3.4 is selected here for the BMJ design optimization on seismic resilience. Details of the structural properties can be found in Section 3.4. Here, the frame is modeled with nonlinear beam-column elements and a gravity column to account for the P-Delta effect. The seismic masses are lumped to the gravity column at each floor. Same as Section 4.3, the real-time nonlinear 2D dynamic analysis platform under MATLAB/Simulink environment termed RT-Frame2D is adopted (Castaneda Aguilar 2012, Castaneda, Gao et al. 2013) for the numerical substructure in RTHS. The explicit unconditionally-stable CR integration scheme (Chen and Ricles 2008) is adopted. The frame model has a total of 48 degrees of freedoms (DOFs), with each node of 3 DOFs (i.e. horizontal, vertical, and rotational DOF). With the rigid floor assumption and the base boundary conditions shown in Figure 5.3, the structural model for nonlinear time history analysis is reduced to 28 DOFs.

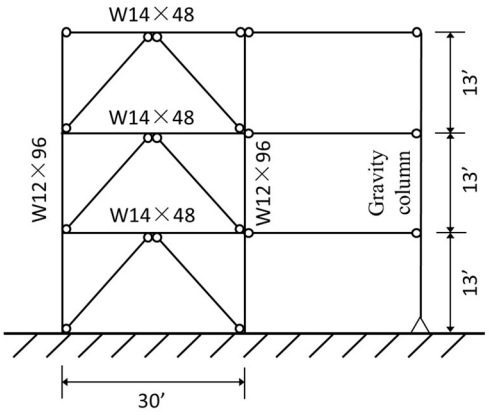

Figure 5.3 3-story braced frame model

For the modeling of the BMJ braces in RT-Frame2D, the 2D BMJ analytical model derived in Section 3.2.2 is used to determine an axial displacement-force model. Note that similarly as the implementation in Chapter 3 with OpenSees, the all 6 BMJ phases are linearized to construct a multilinear material model for faster computation under MATLAB-Simulink environment. The total BMJ brace behavior is modeled using a superposition of multiple axial brace elements with the multilinear material model of different settings corresponding to the different sizes of each column set. A 5000 Hz sampling frequency is selected for the numerical integration to allow adequate simulation performance on the BMJ behavior. A concentrated plasticity model is adopted for the nonlinear beam-column elements in RT-Frame2D, assuming that the yielding occurs at the element ends. A bilinear moment-curvature hysteresis material model with kinematic hardening and a post yielding ratio of 2.5% is applied. The detailed element properties of the frame can be found in Section 3.4. The values of the seismic mass lumped to the gravity column are 1.46×10^5 kg and 1.49×10^5 kg at the $1^{st}/2^{nd}$ and 3^{rd} floor, respectively. Rayleigh damping is assigned with 5% for the first and second modes.

A suite of 10 ground motions corresponding to 10%/50 years seismic hazard level are selected as design scenarios, which satisfies the requirement of a minimum of 7 ground motions considered (ASCE 2010). These 10 ground motions are selected from a group of 20 ground motions (LA1-20), which is developed with a variation of amplitude and frequency content by Somerville (1997) from fault-parallel and fault-normal orientations of 10 earthquake records corresponding to a seismic hazard level with 10% probability of exceedance in 50 years for Los Angeles, California. The selection is based on that the mean spectrum of the selected ground motion suite overall matches the design spectrum of the building around its natural period T_1 ($0.2T_1 - 1.5T_1$) (ASCE 2010). Note that the design of BMJ bracing system would change the natural period. Therefore, the selection of ground motion is following a wider range of period to be overall match and above the design spectrum, where the range is expected to cover the range of 0.2 to 1.5 times the possible natural period range. Figure 5.4 presents the 5% damped spectral accelerations ($Sa(T_1, 5\%)$) of the selected 10 ground motions with their mean spectrum compared to the design spectrum for the seismic hazard level at probability of exceedance 10%/50 years at LA. The design spectrum is obtained based on the ground motion parameters from the unified hazard tool (v 4.1.1) of USGS (USGS 2014), under the assumption of site class D. Note that the design spectral acceleration at the structural natural period varies with the BMJ design and therefore needs to be updated accordingly during the design optimization iterations.

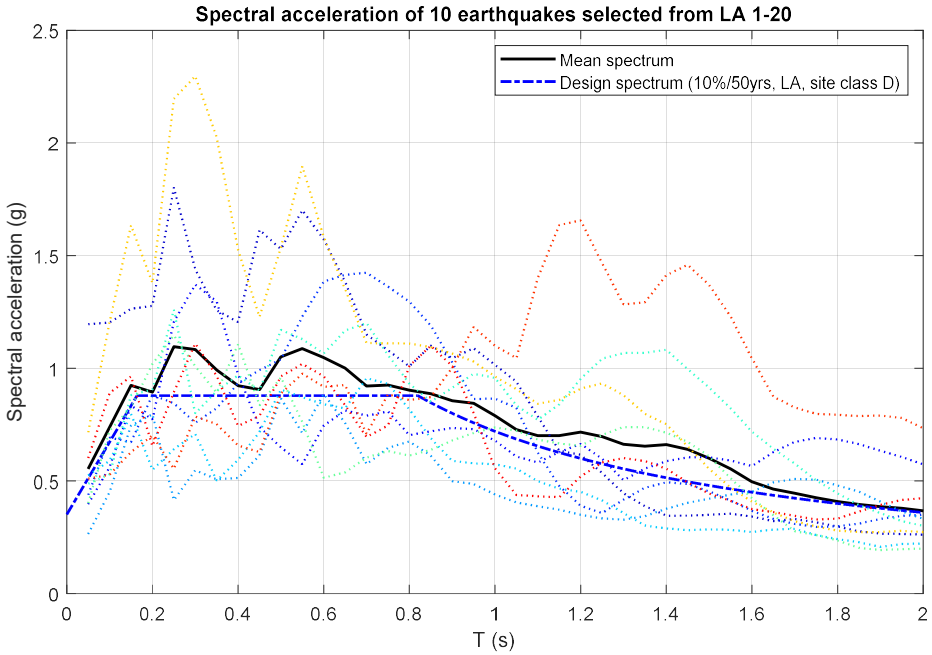

Figure 5.4 Spectrum accelerations of 10 selected ground motions and design spectrum corresponding to 10% exceedance in 50 years in LA (site class D)

5.3.2 Seismic resilience optimization with NN fragility metamodel

The optimization of seismic resilience is conducted for the design of the BMJ brace configuration proposed in Section 3.4 for the same 3-story braced frame. As Figure 3.13 shows, one BMJ brace is consisted with 4 sets of BMJ columns with different geometry settings. The BMJ column is consisted with the PMMA column and steel cap as it discussed in Section 3.2.1. The material properties can be found in Table 3.2. There are 9 optimizable design variables selected for a single BMJ brace and the BMJ brace design is assumed the same for each story. The initial eccentricity to trigger buckling is assigned with 0.7 mm for all the BMJ columns. The 9 optimizable design variables are summarized in Table 5.1 with the corresponding search space; where $L_{t,max}$ is the length of the longest column set of the BMJ brace, the gap is the same between column sets, L_t is the total column length including the

cap thickness, L_c is the PMMA column length, b_c is the column width, t_{cp} is the cap thickness, b_{cp} is the cap width, $d_{tot,i}$ is the total width of column set *i.* The detailed definition of these geometric variables can be found in Section 3.2 (Figure 3.1). Note that the search spaces of the design variables are defined based on the desired region identified (Figure 3.11) in Section 3.3 for desirable linear buckling behavior without material yielding, and based on geometric limitations considering the frame geometries.

Table 5.1 BMJ brace design variable and optimization search space

Design variable	$L_{t,max}$ (m)	gap (cm)	$\frac{L_c}{b_c}$	$\frac{t_{cp}}{L_t}$	$\frac{b_{cp}}{b_c}$	$\frac{d_{tot,1}}{b_c}$	$\frac{d_{tot,2}}{b_c}$	$\frac{d_{tot,3}}{b_c}$	$\frac{d_{tot,4}}{b_c}$
Search space	[1, 5]	[2, 10]	[20, 30]	[0.01, 0.1]	(1, 1.4]	(2, 15]	(2, 15]	(2, 15]	(2, 15]

For the collection of the training samples, 30 sets of the 9 design variables are sampled based on LHS over the search spaces as the design samples to provide the inputs/outputs data set for the NN fragility metamodel training process. LHS is adopted here to obtain random samples with relatively uniform spacing, avoiding undesirable clustering samples that may occur under a general random sampling. In addition, to improve the coverage on extreme boundary scenarios, 4 additional sets with design variables at extreme boundaries are added. The total 34 sampled sets of design variables are summarized with a series of plots in Figure 5.5, showing a good coverage of the design variable space.

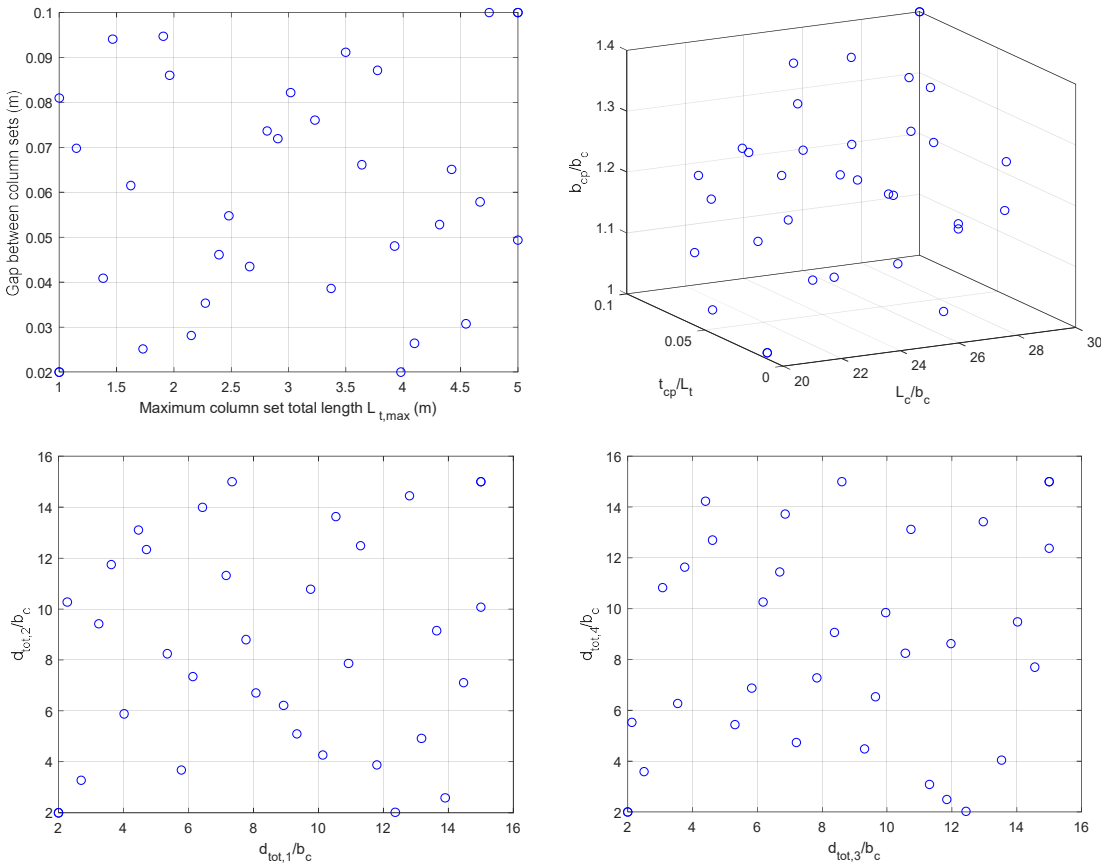

Figure 5.5 Collected samples on the 9 design variables of a BMJ brace over design variable space

The 9 design variables and the 5% damped spectral accelerations ($Sa(T_1, 5\%)$) of the selected 10 ground motions at structural nature period are set as the NN inputs. Note that $Sa(T_1, 5\%)$ of the ground motions are determined according to different BMJ designs that lead to different natural period of the braced frame. The natural period of the braced frame is determined based on modal analysis assuming the BMJ brace with columns within linear phase. The NN outputs are set as the lognormal distribution moments (θ and β) that determines the fragility functions for the 12 DS considered. The outputs are collected through the MGSS-IDA algorithm developed in Section 4.4 and the fragility analysis described in Section 4.1.2, for different settings of design variables from the input sample set. Similar as section

4.3.1 discussed, the damage states thresholds adopted for the steel braced frame are given in Figure 5.6 following HAZUS and ASCE/SEI 41-13 (Engineers and Institute 2014). With lower boundary of the search spaces for 12 DS set to be 0, their higher boundaries are initialized with: intensity scale of 1, 1, 2.5, and 5 for structural (S) SD, MD, ED, and CD; 0.5, 1, 2.5, and 3 for drift-sensitive nonstructural (NSD) SD, MD, ED, and CD; and 0.5, 1.5, 2, and 3 for acceleration-sensitive nonstructural (NSA) SD, MD, ED, and CD. Note that these boundaries are set empirically, and the MGSS-IDA algorithm introduced in Section 4.4.1 is able to enlarge the search boundary if convergence cannot be reached. Two networks are trained, one for each output, θ and β. Both the networks use a 19-12-12-12-12-12-12-12 NN configuration (i.e. 19 inputs, 12 outputs, with 12 neurons for each of the six hidden layers) for its overall good observed performance. To support training regularization and avoid overfitting, the full data set is randomly divided into 70% for training set, 20% for validation set, and 10% for test set. For better generalization, the early stopping criteria is set with 100 iterations and 50 retraining cycles are conducted to find the trained network with best generalization.

Damage States				No damage	SD	MD	ED	CD
Limit Sates Criteria	Structural		θ_{max}	0.5%	1%	3%	8%	
			$\theta_{\mathrm{res},max}$			0.5%	2%	
	Non-structural	Drift-sensitive	θ_{max}	0.4%	0.8%	2.5%	5%	
		Acceleration-sensitive	a_{max}	$0.3g$	$0.6g$	$1.2g$	$2.4g$	

Figure 5.6 Damage states thresholds for the 3-story steel braced frame

Figure 5.7 shows the predicted θ and β for all 12 DS with the trained NN fragility metamodel comparing to that obtained from MLE based on the searched IMs using MGSS-IDA (i.e., the actual values). The data shown in the comparison include

the training set, validation set, and test set, therefore includes not only seen data but also unseen data. The correlation coefficient (R_{NN}) between the NN prediction and the MGSS-IDA actual values shows the goodness of the prediction, with the perfect prediction having $R_{NN} = 1$. The line of perfect prediction (MGSS-IDA = NN prediction) is also plotted for reference. The trained NN fragility metamodel illustrates a good regularization and prediction performance on the full data set.

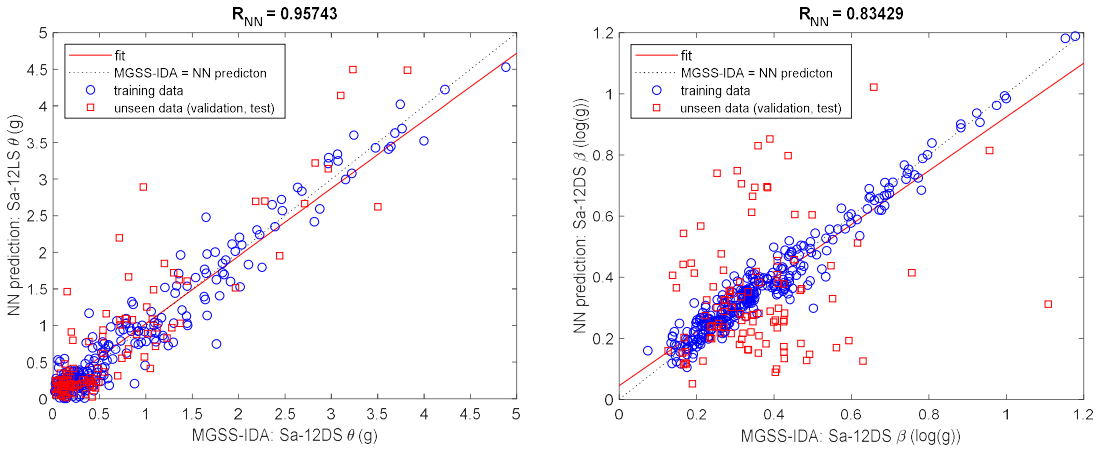

Figure 5.7 Trained NN fragility metamodel prediction performance on lognormal distribution moments

Based on the trained NN fragility metamodel, fragility curves are also predicted and validated with that constructed from the MGSS-IDA results at random unseen scenarios. Figure 5.8 presents one of the validations under an unseen design scenario. Compared to the actual fragility curves obtained through MGSS-IDA, it can be seen that the NN fragility metamodel provides an overall good prediction. It is observed that although the prediction for some damage states are less accurate, the errors are regularized among different damage states and an overall agreement between predicted and actual fragility curves is confirmed. Also, the final prediction performance on structural seismic resilience demonstrates a good agreement with the

actual results based on MGSS-IDA (Table 5.3). Therefore, the NN fragility metamodel is considered to be applicable to support the optimization on seismic resilience. The comparison on seismic resilience is plotted in Figure 5.9 and summarized in Table 5.3 for two randomly selected unseen design scenarios. The design variables of the two unseen scenarios are summarized in Table 5.2.

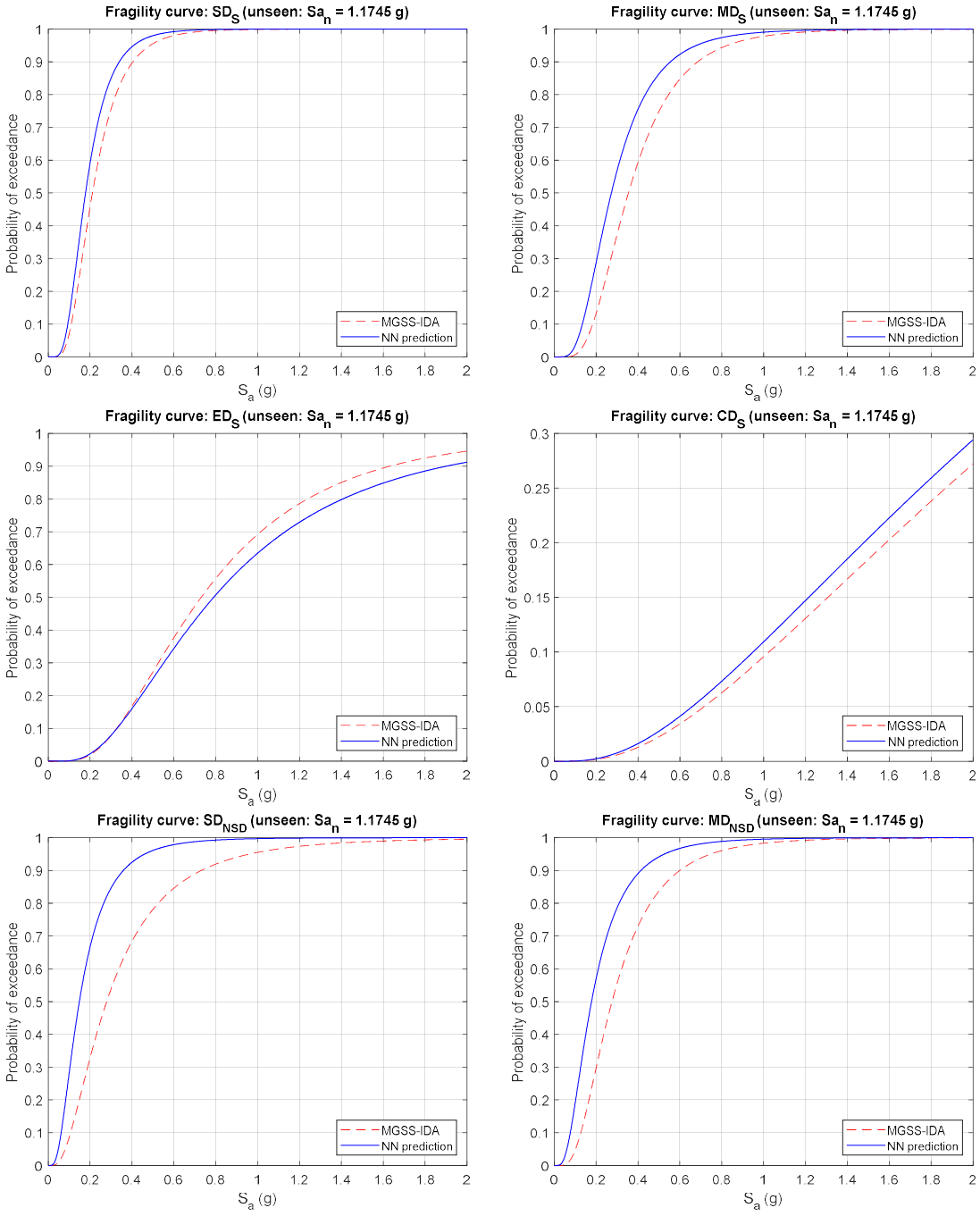

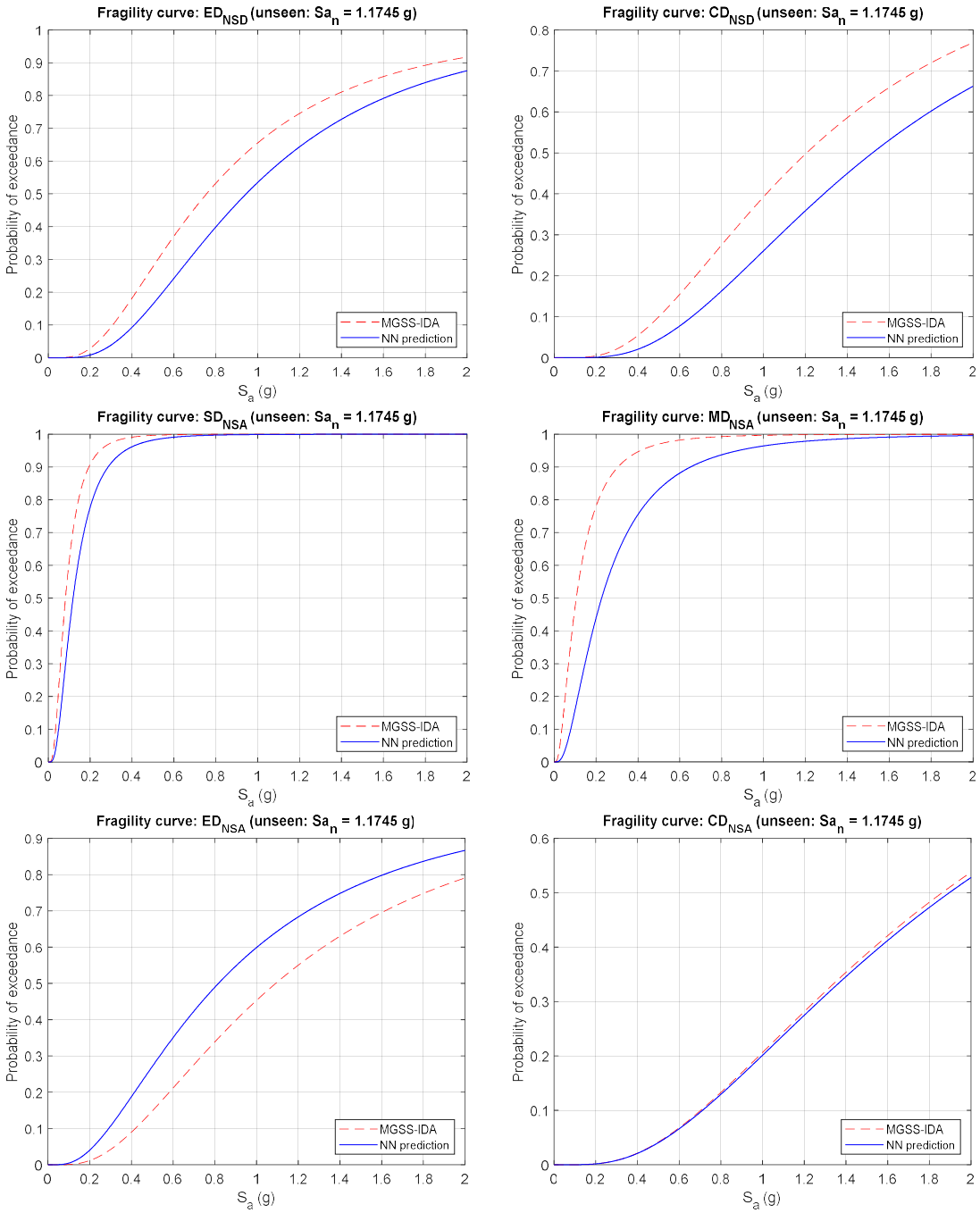

Figure 5.8 Trained NN metamodel prediction performance on fragility curves of 12 DS under a random unseen design scenario

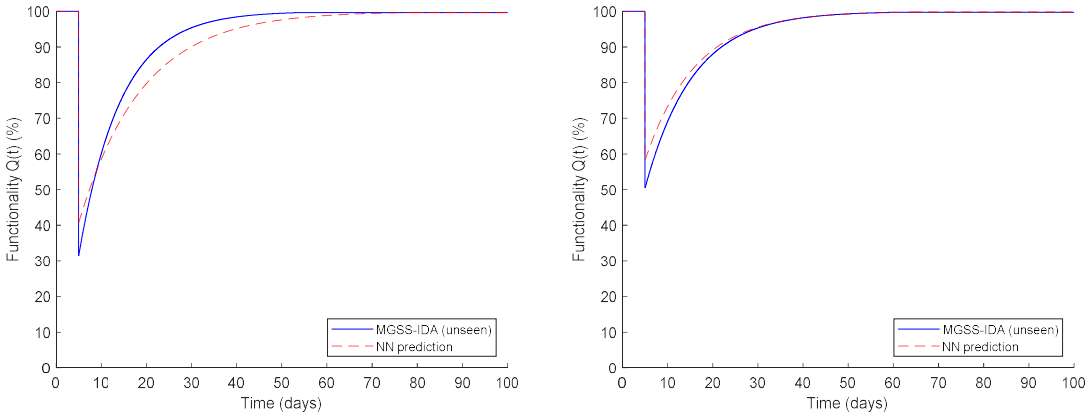

Figure 5.9 Trained NN fragility metamodel prediction performance on structural seismic resilience under couple unseen design scenarios

Furthermore, the trained NN fragility metamodel is implemented in replacement of the IDA/MGSS-IDA and MLE process for fragility analysis and used to optimize the nine selected design variables of the BMJ bracing system for seismic resilience. The PSO process based on the NN fragility metamodel is termed as NN-PSO here. The weight inertia of the PSO process is selected as 1 for a good balance between global and local exploration. The search space is constrained by the range of the design variables covered by the NN training set. The initial particle positions are sampled over the search space using LHS for a good global exploration. The NN-PSO process to converge on particle positions (i.e., design variables' values) is illustrated with Figure 5.10. The optimal solution found by NN-PSO for the nine design variables of the BMJ brace is given in Table 5.2. Note that the design variables *gap* converged to the upper boundary and cap thickness ratio (t_{cp}/L_t) converged to the lower boundary. This is potentially due to that larger gap allows a more gradual overall stiffness variation of the BMJ brace, and smaller cap thickness ratio (t_{cp}/L_t) provides more energy dissipation per cycle according to the parametric study shown in Figure 3.10. Converting the design ratios to actual dimensions, the NN-PSO

solution suggests that column length $L_c = 2.88$ m, width $b_c = 11.44$ cm, cap thickness $t_{cp} = 2.94\ cm$, total depth $d_{tot} = 24.14\ cm$, for the shortest set of BMJ columns with the minimum dimensions in the BMJ brace. These dimensions of the NN-PSO solution are considered to be practically achievable. The NN-PSO searched optimal solution provides a predicted resilience index R = 94.26%, seismic loss L = 30.56%, and recovery time $T_{RE} = 38$ days.

Table 5.2 NN-PSO optimal solution and NN unseen design scenarios on BMJ brace design variables

Design candidates	$L_{t,max}$ (m)	gap (cm)	$\frac{L_c}{b_c}$	$\frac{t_{cp}}{L_t}$	$\frac{b_{cp}}{b_c}$	$\frac{d_{tot,1}}{b_c}$	$\frac{d_{tot,2}}{b_c}$	$\frac{d_{tot,3}}{b_c}$	$\frac{d_{tot,4}}{b_c}$
NN-PSO solution	3.24	10	25.18	0.01	1.25	8.78	7.54	2.12	2.11
Unseen scenario 1	4.42	6.51	26.78	0.08	1.37	8.08	6.70	9.65	6.54
Unseen scenario 2	2.15	2.81	25.63	0.1	1.28	8.93	6.21	2.13	5.53

The iteration history of the seismic resilience index R (i.e., the objective function) and the corresponding seismic loss L and recovery time T_{RE} are provided in Figure 5.11-12. It can be seen that the objective function R keeps increasing during the iteration and converging process. For the seismic loss and recovery time, the iterative behavior is not necessarily monotonic. The seismic loss decreases with each iteration, while the recovery time does not. This reveals that while optimizing for improved seismic resilience, there may be tradeoffs between seismic loss and recovery time. This is because the seismic loss depends on the fragilities of all the damage states, while recovery time as defined here only depends on the fragilities of

the structural damage states. However, the recovery time is reduced from the initial design candidates (i.e. initial particle positions).

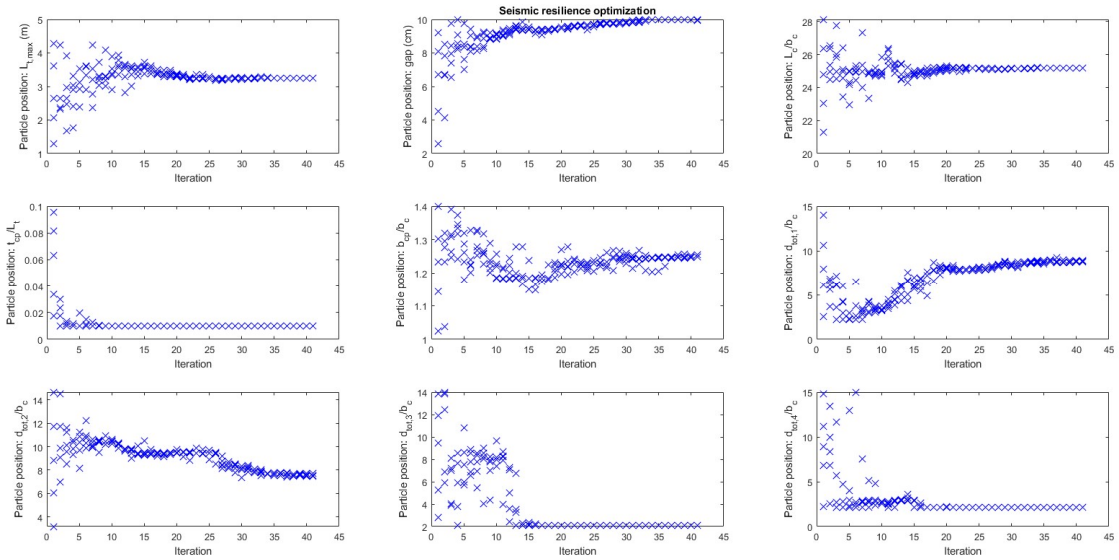

Figure 5.10 NN-PSO converging process of 9 design variables of a BMJ brace for optimization on structural seismic resilience

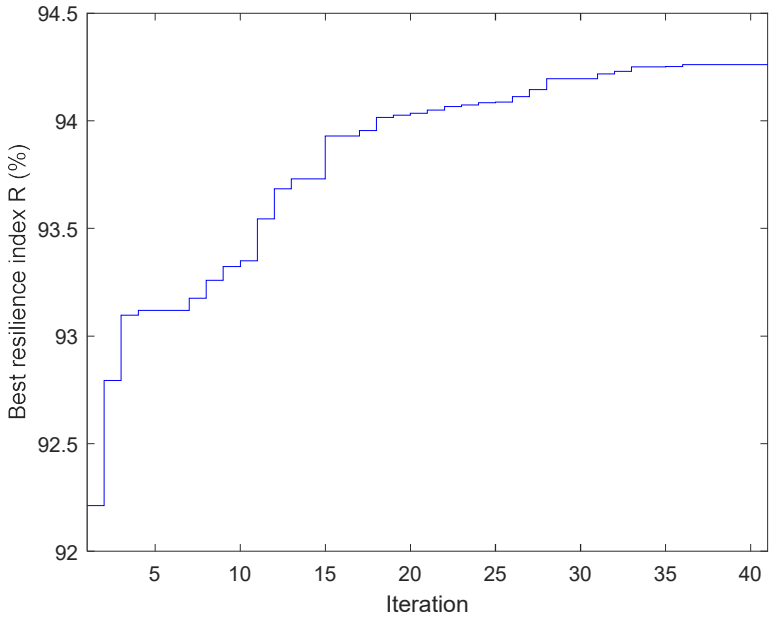

Figure 5.11 NN-PSO iteration history on structural resilience index R

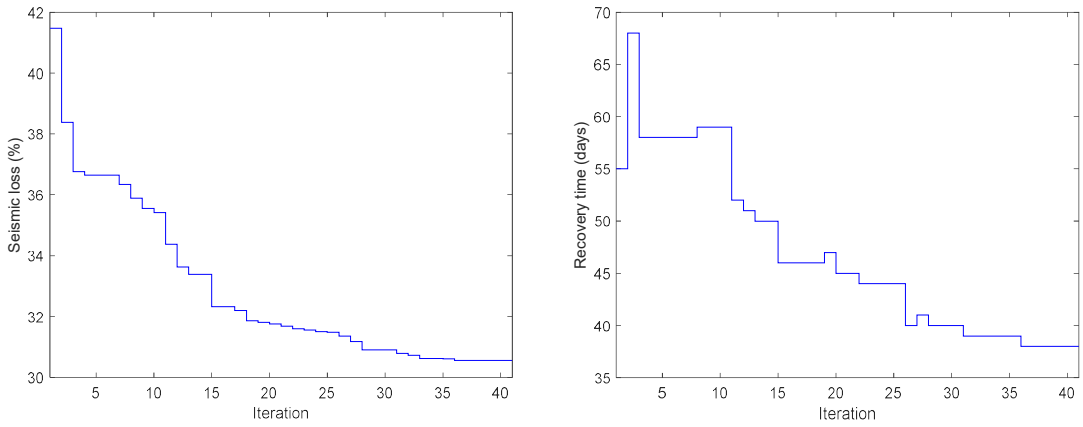

Figure 5.12 NN-PSO iteration history on seismic loss and recovery time

Comparing the NN-PSO found optimal design to the previously validated unseen design candidates shown in Figure 5.9, an improvement in seismic resilience is observed, in terms of reductions in both seismic loss and recovery time. Detailed comparison is given in Table 5.3. The design variables of the design candidate under comparison are summarized in Table 5.2. The NN-PSO optimal solution, which is an unseen design case for the NN training, is validated with the seismic resilience evaluation result based on MGSS-IDA, shown in Figure 5.13 and Table 5.3. Although the validation accuracy on the NN-PSO solution as an unseen scenario has some discrepancies, the overall agreement of the improved seismic resilience suggests the applicability of the NN-PSO approach to support design optimization. These observed discrepancies are potentially due to some local overfitting issues and the complex optimization problem. It is worth noting that the NN-PSO accuracy could be improved through further fine tuning the NN configuration and hyper parameters and training the NN fragility metamodel with larger data set depending on the complexity of the problem and the needed prediction accuracy.

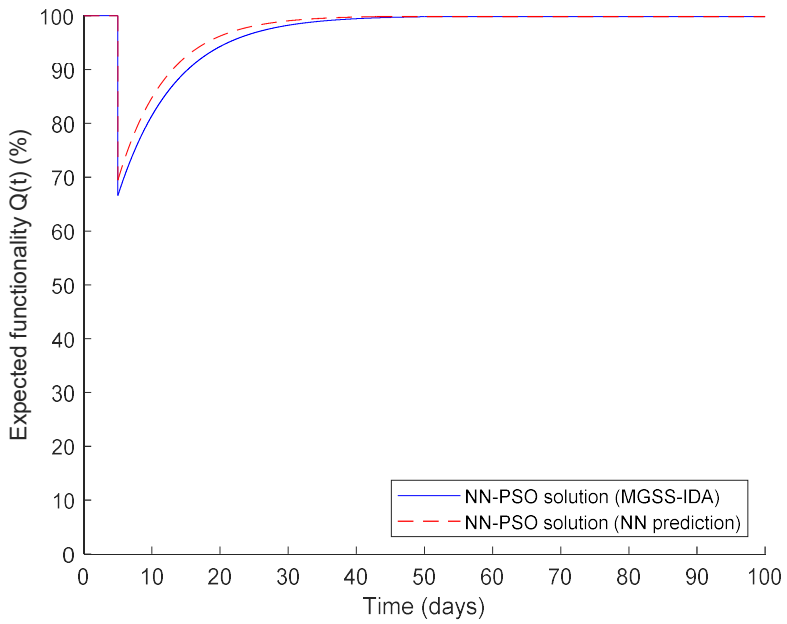

Figure 5.13 Validation on the seismic resilience of the NN-PSO found optimal design

Table 5.3 Validation of NN metamodel predicted and NN-PSO found optimal design on seismic resilience with results based on MGSS-IDA

Design candidate	Unseen scenario 1 (NN)	Unseen scenario 1 (MGSS-IDA)	Unseen scenario 2 (NN)	Unseen scenario 2 (MGSS-IDA)	Optimal solution (NN-PSO)	Optimal solution (MGSS-IDA)
Seismic loss (L)	59.37%	68.62%	41.78%	49.58%	30.56%	33.41%
Recovery time (T_{RE})	74 days	49 days	59 days	56 days	38 days	45 days
Seismic resilience index (R)	88.85%	87.11%	92.15%	90.69%	94.26%	93.73%

The above discussed results demonstrate the accuracy of the NN fragility metamodel and its applicability to support a rapid optimization on structural seismic resilience. Table 5.4 further evaluates the efficiency of the NN-PSO approach compared to direct PSO based on MGSS-IDA and IDA. NN-PSO trained with MGSS-IDA method demonstrates great efficiency and significant reduction in

computational cost, with 14.8% computational time needed comparing to PSO based on IDA in this case. With the observed computational cost of PSO with IDA/MGSS-IDA, it would be much more costly to implement PSO with the RTHS integrated framework proposed in Chapter 4. However, the NN-PSO approach proposed here not only provides a much more efficient approach to conduct PSO on seismic resilience numerically, but also demonstrates great potential to support the realization of RTHS integrates PSO on seismic resilience.

Table 5.4 Computational cost comparison between direct PSO based on IDA or MGSS-IDA, and NN-PSO

Seismic resilience optimization approach	PSO (IDA base)	PSO (MGSS-IDA base)	NN-PSO (training based on MGSS-IDA)
Number of analysis needed	51250	45715	7582
Normalized computational time	100%	89.2%	14.8%

Note that the comparison above is based on this specific numerical case study; the actual computational cost may vary depending on different optimization problem and conditions. In this case, due to the highly nonlinear behavior of the BMJ braces (i.e. stiffness variations), there may be a lot of local weaving behavior that lead to larger number of analysis during the MGSS-IDA search process comparing to the implementation in Section 4.4.2. As a result, the reduction in computational demand using MGSS-IDA as compared to IDA is not as large as it discussed in Section 4.4.2. However, it is worth noting that the number of analysis needed for one structural seismic resilience evaluation based on MGSS-IDA varies depending on different conditions (e.g., ground motion and structural characteristics.). An average number of analysis needed for one structural seismic resilience evaluation based on MGSS-IDA

is observed to be about 223 in this case, for the selected 10 ground motions suite under the 10%/10 years seismic hazard level. The estimation on the number of analysis needed for IDA based PSO assumes that the IDA has a fixed incremental step of 0.2 intensity scale and the same maximum scaling as MGSS-IDA. The PSO process used for comparison here has 5 particles and 41 iteration steps as Figure 5.10 shows. The NN-PSO computational time is considered only based on the time needed for collecting training data set, due to that the time of the PSO process using the NN fragility metamodel is negligible, though there is some additional time required for updating the spectral acceleration at structural natural period during the PSO process.

5.4 Summary

This chapter proposed a novel optimization approach for seismic resilience based on fragility metamodeling using deep neural networks, MGSS-IDA and PSO, denoted as NN-PSO here. With a numerical case study on optimization of multiple design variables of the BMJ bracing system proposed in Chapter 3 for a 3 story braces frame, the proposed NN-PSO approach demonstrates the capability to support automated design optimization on seismic resilience, with a significant reduction in computational cost compared to direct PSO based on IDA/MGSS-IDA. This provides great potential to enable a rapid optimization on structural seismic resilience and overcome the obstacle in the realization of a cyber-physical (e.g. RTHS integrated) seismic resilience optimization framework.

CHAPTER 6 CYBER-PHYSICAL STRUCTURAL OPTIMIZATION OF SEISMIC RESILIENCE WITH ONLINE LEARNING NEURAL NETWORKS

In this chapter, the structural seismic resilience optimization approach proposed in Chapter 5 is combined with the cyber-physical structural analysis approaches proposed in Chapter 4. In addition to the fragility metamodel developed through feedforward neural networks (Chapter 5), long-short term memory (LSTM) neural networks are introduced to enable an online-learning process for the metamodeling of the RTHS physical component. The developed LSTM component metamodel and NN fragility metamodel are combined with the heuristic PSO algorithm for the optimization of structural design for seismic resilience. A case study is conducted for structural retrofit with inter-story isolation under a 2%/50 years seismic hazard level to improve the structural seismic resilience through the optimal design of the isolation layer and supplemental damper control algorithm. The case study demonstrates the potential of the proposed CPS-NN-PSO approach to significantly reduce the experimental and computational cost for the structural seismic resilience-based design and optimization process.

6.1 Background

As discussed in Section 5.1, the high computational cost is one of the major challenges for the optimization of seismic resilience. This challenge is greater when critical substructures physically tested. In cases where large errors may exist between the numerical model and the physical structure for complex structural systems or under complex design scenarios, techniques such as RTHS can be integrated into the

optimization process. This is especially valuable when designing for seismic resilience with large uncertainties in earthquake magnitudes and frequency content. Therefore, this Chapter proposes an online learning approach using LSTM neural networks for the metamodeling of the RTHS physical component. With the combination of the LSTM component metamodel and the NN fragility metamodel, a rapid optimization process for seismic resilience-based structural design is enabled which integrates the contribution of RTHS (e.g., cyber-physical testing).

6.2 Methodology

The metamodeling of the RTHS physical substructure is integrated into the optimization process to improve both the realism and efficiency of the optimization on seismic resilience for structural design. This metamodel for the physical substructure is then used to develop the NN fragility metamodel, which is then used for optimization as proposed in Section 5.2.

6.2.1 RTHS online learning with long-short term memory neural network

The optimization approach with NN fragility metamodel proposed in Section 5.2 provides an efficient tool for structural design optimization for seismic resilience through numerical simulation, but obstacles remain if the IDA/MGSS-IDA directly uses RTHS as in Chapter 4. To improve the efficiency of the NN-PSO optimization approach with physical modeling through RTHS, a metamodeling approach of the physical specimen is proposed here to achieve a combined CPS-NN-PSO approach. Instead of collecting the training data for the NN fragility metamodeling directly using RTHS integrated IDA/MGSS-IDA discussed in Section 5.2 (Figure 5.1), the behavior of the RTHS physical substructure is iteratively learned online with RTHS

tests until a predefined convergence criteria is met. As it discussed in Section 2.4.3, the time history response of the RTHS physical substructure can be considered as sequential data with time dependency. Considering that the physical substructure in RTHS is usually highly nonlinear and the wide amplitude/frequency range needed to cover for the fragility analysis, LSTM neural network is adopted here for the online learning task due to its benefit of avoiding the gradient vanishing/exploding problem during training and strong capability in learning sequential data with time dependency.

As Figure 6.1 illustrates, metamodeling of RTHS physical component, termed LSTM online learning, starts with the definition of learning space. The learning space is bounded by the considered design scenarios for design optimization. Learning scenarios are sampled using LHS over all variables (i.e., ground motion, intensity scale, and design variables) to ensure adequate coverage of the design space. Using LHS, n learning scenarios are initially created, where n is determined as the maximum affordable number of experiments. Then, an initial m RTHS tests are collected as test data set, where $m < n$. After the test data set is ready, the later on accumulated training data set is fed into the LSTM neural network training. Note that the accumulated input (i.e., training data set) for the LSTM training is updated every Δi steps for efficiency, where Δi can be determined with smaller or larger number as needed. After each LSTM training, the prediction error of the trained LSTM component metamodel is evaluated with the test data set, in terms of the root mean squared error (RMSE) between the prediction and actual time history responses. Based on the error evaluation, the online learning and the RTHS testing can be terminated once the pre-defined convergence criteria is met or when the maximum

affordable number of experiments is reached (i.e. $i = n$). The converged LSTM component metamodel can then be used for the data collection through IDA/MGSS-IDA for the training of the NN fragility metamodel following the approach proposed in Section 5.2.

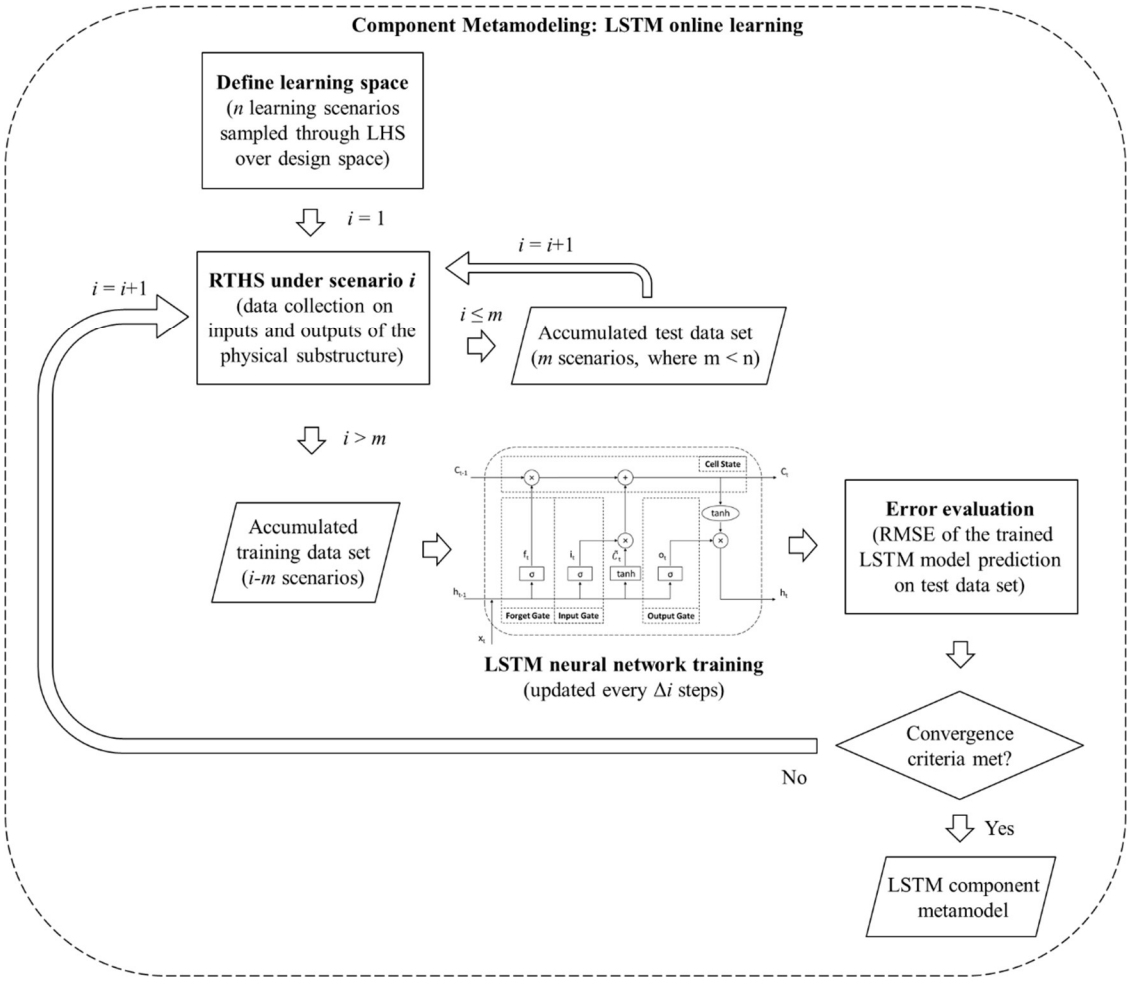

Figure 6.1 LSTM online learning procedure

For the specific learning task on the time history response of the RTHS physical substructure, the full LSTM neural network under training is constructed as Figure 6.2 shows, including a sequence input layer, a LSTM layer, a dropout layer, a fully connected layer, and a regression layer. The sequence input layer feeds the input data (i.e., inputs to the RTHS physical substructure) sequentially into the full neural

network. Note that training data is standardized with zero mean and unit variance for the ease of training. For the LSTM layer, details are discussed in Section 2.4.3. To prevent overfitting during training, a dropout layer works efficiently and is included after the LSTM layer. The dropout layer randomly disconnects a certain amount of neuron nodes during training iterations, and therefore reduces the sensitivity to some less important information in the training data set to avoid overfitting. The fully connect layer transforms the features (not yet comparable with the output training data) learned in previous layers with its own weights and bias to enable the comparison with output training data. The final regression compares the mean-squared-error between the prediction values and the output training data for the optimization on network weights and bias.

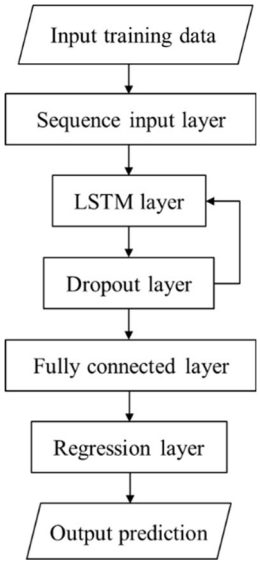

Figure 6.2 Full LSTM neural network under training

6.3 RTHS Case Study

To demonstrate the proposed LSTM component metamodeling for a combined CPS-NN-PSO, a case study is conducted and discussed in this section.

6.3.1 Structural model and selection of earthquake records

A retrofit design with inter-story isolation for a prototype 3-story office building assumed with stiff soil condition located in Pomona, California (Dong, Sause et al. 2016), is considered for the case study here. Figure 6.3 shows the plan of the original prototype building. The structural system of the building can be divided into a gravity load system, a lateral resisting system, and a damping system. The gravity load system are the uniformly distributed gravity frames in plan. The lateral resisting system consists of 8 identical single-bay moment resisting frames (MRFs). The damping system consists of 8 single-bay frames with viscous dampers and associated bracing, termed as damped braced frames (DBFs). Each MRF are paired with one DBF in one direction. Due to symmetry, a quarter of the total floor area is considered for the seismic tributary area associated with a pair of MRF and DBF in each direction. The horizontal displacement at the ground level is restrained, with the columns fixed at the basement level. The design details of the building can be found in the reference (Dong, Sause et al. 2016).

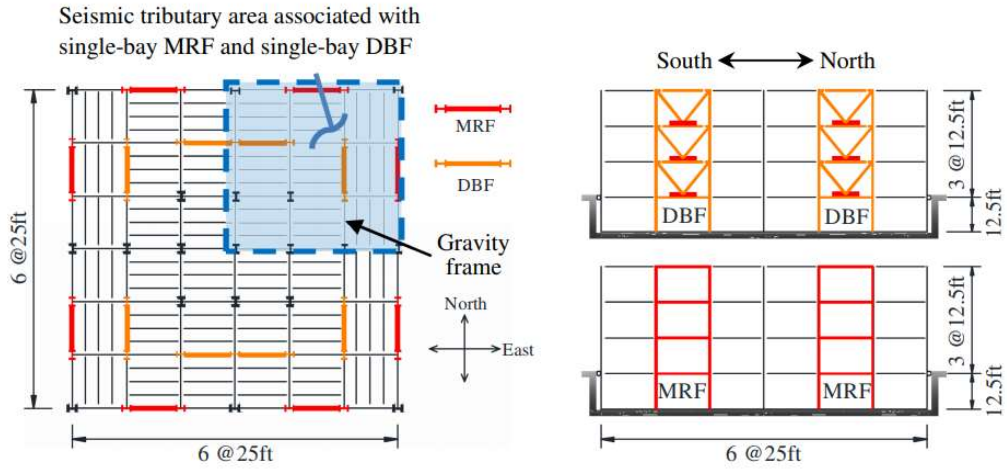

Figure 6.3 Plan and section view of the original 3-story office building (Dong, Sause et al. 2016)

The considered direction of earthquake excitation is north-south direction. For the DBFs, viscous dampers providing 10% damping for the original structure at the first mode are assumed to be installed at each floor. For the retrofit case study, it is assumed that an additional three stories are needed to meet increased occupancy demand. Assuming the additional three stories contribute the same amount of mass, the gravity load capacity of the columns are verified for the retrofit. Here, the major considered retrofit strategy is inter-story isolation, which has been increasingly applied in practical retrofit designs (Zhou, Yang et al. 2004, Dutta, Sumnicht et al. 2008) for its ease of construction and low increase in base shear demand due from the additional stories. The design of the isolation layer is considered for optimization. The additional three stories for retrofit is assumed with the same design of the MRFs and gravity load system as the original structure, however, the DBFs are replaced with gravity load columns, considering that the inter-story isolation protects the upper stories and supplemental damping is not needed.

Figure 6.4 shows the structural model of the full-scale building with the additional stories of retrofit for the case study. Due to symmetry of the floor plan (Figure 6.3), only a quarter of the structure is considered for modeling. Therefore, there is one MRF and one DBF included in the structural model for the original structure in the north-south direction. Following the assumptions for the additional three stories, the lateral resisting system is modeled as one MRF. The MRF and DBF are modeled with nonlinear beam-column elements. The gravity load systems for both the original structure and the retrofit structure are modeled as gravity column to account for the P-Delta effect. The seismic masses are lumped to the gravity columns at each floor. The inter-story isolation layer is modeled with high damping laminated

rubber bearings and an MR damper to control the response at the isolation level. The structural model has a total of 108 degrees of freedoms (DOFs), with each node of 3 DOFs (i.e. horizontal, vertical and rotational DOF). For simplicity, only the horizontal DOF is considered at the isolation layer. Furthermore, with the rigid floor assumption and the base boundary conditions shown in Figure 6.4, the structural model for nonlinear time history analysis is reduced to 75 DOFs.

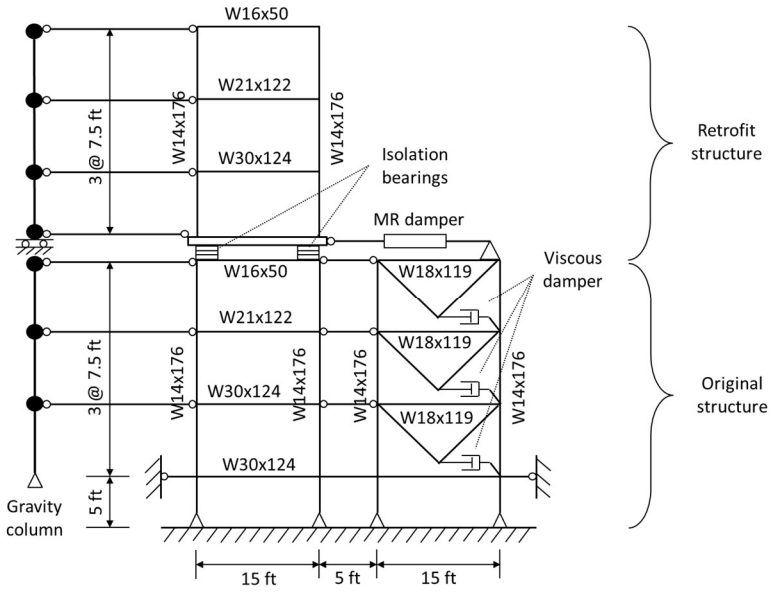

Figure 6.4 Structural model of the full-scale retrofit building

For RTHS, the MR damper is considered for the physical substructure and the rest of the structure is modeled numerically. Note that the structural elements to be tested in RTHS as physical substructure can be determined based on different needs and experimental resources. As with Section 4.3, the real-time nonlinear 2D dynamic analysis platform under MATLAB/Simulink environment termed RT-Frame2D is adopted (Castaneda Aguilar 2012, Castaneda, Gao et al. 2013) for the numerical substructure in RTHS. The explicit unconditionally-stable CR integration scheme (Chen and Ricles 2008) is adopted. A 500 Hz sampling frequency is selected for the

numerical integration to enable a real-time implementation. A concentrated plasticity model is adopted for the nonlinear beam-column elements in RT-Frame2D, assuming that the yielding occurs at the element ends. A bilinear moment-curvature hysteresis material model with kinematic hardening and a post yielding ratio of 2.5% is applied. The element properties including linear flexural rigidity (EI), axial rigidity (EA), shear rigidity (GA) and yield curvature κ are given in Table 6.1. In addition to the self-weight distributed over the beam elements as distributed mass, the values of the seismic mass lumped to the gravity column are 2.78×10^5 kg and 2.04×10^5 kg at the $1^{st}/2^{nd}/4^{th}/5^{th}$ and $3^{rd}/6^{th}$ floor, respectively. For the lumped mass of the isolation layer, 5.00×10^5 kg is assumed considering a realistic proportion relative to the floors. Rayleigh damping is assigned with 2% for the first and second modes of the total structure.

Table 6.1 Element properties of the structural model

Member section	W14x176 (strong axis)	W14x176 (weak axis)	W30x124	W21x122	W16x50	W18x119
EI ($N\cdot m^2$)	1.78×10^8	6.98×10^7	4.40×10^8	2.46×10^8	5.49×10^7	1.82×10^8
EA (N)	6.68×10^9	6.68×10^9	4.71×10^9	4.63×10^9	1.90×10^9	4.53×10^9
GA (N)	2.51×10^9	2.51×10^9	1.77×10^9	1.74×10^9	7.11×10^8	1.70×10^9
κ (m^{-1})	8.90×10^{-3}	8.70×10^{-3}	4.50×10^{-3}	6.30×10^{-3}	8.30×10^{-3}	7.20×10^{-3}

For the isolation layer, the bearings are considered as high damping laminated rubber bearings (HDLRB). Wen's model (Malangone and Ferraioli 1998) is adopted for the numerical modeling of the HDLRB. The hysteretic restoring force of the HDLRB is approximated with Eq. (6.1), with the dimensionless hysteretic displacement $z(t)$ governed by Eq. (6.2).

$$F_0(x_0, \dot{x}_0) = \alpha(D) \cdot \frac{F_y(D)}{d_y(D)} \cdot x_0(t) + [1 - \alpha(D)] \cdot F_y(D) \cdot z(t) \tag{6.1}$$

$$\dot{z}(t) \cdot d_y = -\gamma \cdot |\dot{x}_0(t)| \cdot z(t) \cdot |z(t)|^{\eta-1} - \beta \cdot \dot{x}_0(t) \cdot |z(t)|^{\eta} + \theta \cdot \dot{x}_0(t) \quad (6.2)$$

Where $F_y(D)$ and $d_y(D)$ are the yielding force and displacement; $\alpha(D)$ is the ratio between post- and pre-yielding stress; η is a parameter determines the transition between elastic and plastic response; θ and $\gamma/\beta = \psi$ control the loading/unloading phases; $[\theta/(\gamma+\beta)]^{1/\eta}$ decides the maximum restoring force. The values of the isolator parameters are from the reference (Malangone and Ferraioli 1998), which is fitted from experimental results. The values used here are $d_y = 1.715\ cm$, $F_y = 41.93\ kN$, $\alpha = 0.369$, $\eta = 0.15$, $\theta = 2.0$, and $\psi = -1.5$. The size of the HDLRB is assumed with 200 mm total thickness, based on laminated rubber bearings with similar load capacity (Malek and Basir 2001).

A suite of 10 ground motions corresponding to 2%/50 years seismic hazard level are selected as design scenarios for less computational demand in collecting training data set through RTHS, which satisfies the requirement of a minimum of 7 ground motions considered (ASCE 2010). These 10 ground motions are selected from a group of 20 ground motions (LA21-40), which is developed with a variation of amplitude and frequency content by Somerville (1997) from fault-parallel and fault-normal orientations of 10 earthquake records corresponding to a seismic hazard level with 2% probability of exceedance in 50 years for Los Angeles, California. The selection is based on that the mean spectrum of the selected ground motion suite overall matches and above the design spectrum of the building around its natural period T_1 ($0.2T_1 - 1.5T_1$) (ASCE 2010). Figure 6.5 presents the 5% damped spectral accelerations ($Sa(T_1, 5\%)$) of the selected 10 ground motions with their mean spectrum compared to the design spectrum for the seismic hazard level at probability

of exceedance 2%/50 years at LA. The design spectrum is obtained based on the ground motion parameters from the unified hazard tool (v 4.1.1) of USGS (USGS 2014), under the assumption of site class D. The design spectral acceleration at the structural natural period of the original structure ($T_n = 0.97\ s$) obtained from the design spectrum is $1.5157g$ for the considered hazard level of 2% probability of exceedance in 50 years. Note that the natural period of the total structure after retrofit would change based on the design on the isolation layer.

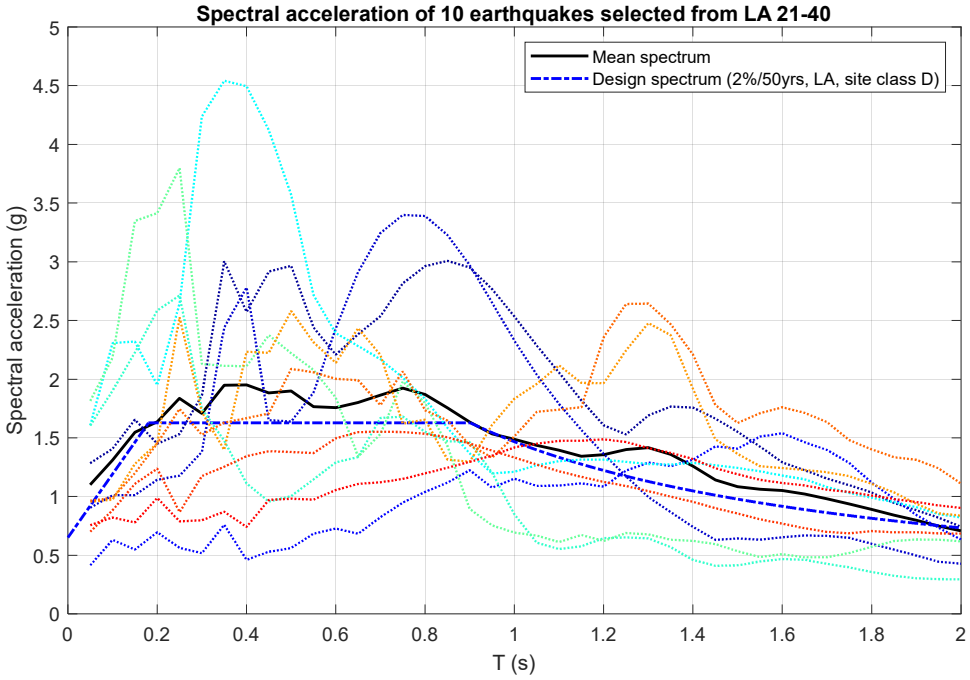

Figure 6.5 Spectrum accelerations of 10 selected ground motions and design spectrum corresponding to 2% exceedance in 50 years in LA (site class D)

6.3.2 RTHS setup for LSTM online learning

Based on the methodology proposed in Section 6.2, the LSTM online learning is implemented with AutomationDesk and ControlDesk under MATLAB/Simulink environment, similarly as it discussed in Section 4.3.1. The same RTHS framework and setup introduced in Section 4.3.1 and Figure 4.6 is adopted with the MR damper

physical substructure. The same actuator control algorithm is used here as Section 4.3.3 discussed. Due to the actuator limit discussed in Section 4.3.5, the input displacement to the actuator is scaled down to 2% of full scale for safety considerations over the large range of ground motion intensities and frequency contents that need to be covered during the LSTM online learning process. The MR damper reaction force is then scaled back to full scale by 50 and fed back to the numerical substructure. The ground motion intensities tested are capped at 5 to ensure safety and adequate level of scaled intensity for the fragility analysis later. As it discussed in Section 4.3.2, the semi-active control for the MR damper is designed with RILD as the primary controller for its benefits in controlling low-frequency structures with large displacement response (e.g., isolated structures). ODBDCO is adopted as the secondary controller for its accurate force tracking performance. Details of the semi-active control is discussed in Section 4.3.2.

The overall flowchart of the automatic process to implement the LSTM online learning procedure (Figure 6.1) under AutomationDesk environment is illustrated in Figure 6.5. The looping of RTHS tests under sampled learning scenarios are bounded by the total number of scenarios (n) defined through sampling using LHS on ground motions, intensities, and design variables. With the online calibration of RTHS setting in ControlDesk from AutomationDesk, every Δi tests are accumulated for the LSTM neural network training in MATLAB and the error comparing to the saved test data set is monitored. For this case study, n is defined as 50 candidate learning scenarios and Δi is selected as 3 RTHS tests. Note that the scenarios located close to the boundaries of the learning space are tested and fed into the LSTM neural network for training at first to ensure adequate early coverage of the learning space. The error

evaluation is conducted on RMSE comparing to the collected test data set with m scenarios, where m is selected as 5 in the case study. Once the pre-defined convergence criterion error is met, the looping of RTHS test can be terminated. Through this converging online learning approach, the RTHS experimental cost/time can be lowered for an integrated CPS-NN-PSO approach to optimize structural seismic resilience.

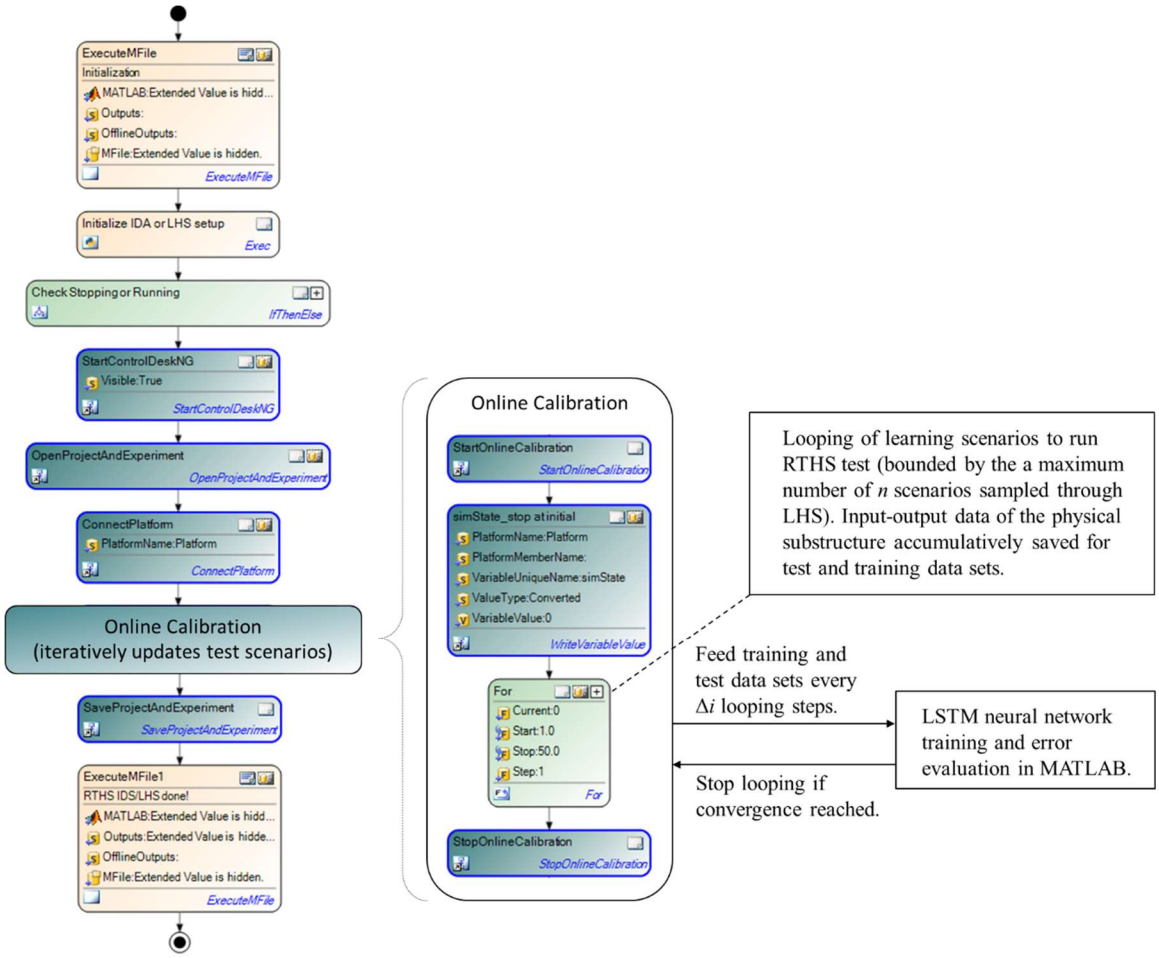

Figure 6.6 Automatic LSTM online learning process under AutomationDesk environment

As it discussed in section 6.2, the construction of the LSTM neural network follows Figure 6.2. For the number of hidden units for the memory cell of the LSTM layer, 100 and 50 are selected for learning the semi-active mode and the passive-

off/on mode respectively, for desirable training performance in terms of both training accuracy and time. For the dropout layer, a probability of 50% is selected for the random disconnection of neurons for regularization. A maximum number of 100 epochs are set for each training of the LSTM neural network. Each epoch completes one forward pass and one backpropagation of error flow to update all the weights and bias. The training data are divided into minibatches of 50 sec data (i.e. a full time-history response under one design scenario) to feed iteratively in each training epoch for the gradient decent of error. Note that the measured force of the training data is cleaned through a low-pass filter with a cut-off frequency of 20 Hz to filter out any high-frequency noise. The minibatches are shuffled every epoch to avoid any potential bias introduced by the initial minibatches fed into the neural network for better regularization. The stochastic gradient descent algorithm Adam (Kingma and Ba 2014) is adopted for the optimization of the weights and bias of the networks for its computational efficiency on non-convex optimization problem (i.e. problem with multiple local optimum and therefore not only one optimal solution). The initial learning rate for gradient descent is defined as 0.1 with a decay by half at every 10 epochs to ensure adequate global and local exploration for the optimization of the weights and bias.

6.3.3 LSTM online learning of MR damper metamodel

The LSTM online learning is conducted for the three modes of the MR damper, including semi-active, passive-off, and passive-on modes. The learning space is defined based on the ground motions (i.e., selected 10 ground motions) and intensity scale range (i.e., caped at intensity scale of 5) considered for the fragility analysis the range of design variables considered for optimization. The design

variables considered under optimization are the number of HDLRB (nRB) for the isolation layer, and the loss factor η and filter frequency ω_f of the RILD controller under the semi-active mode of the MR damper. Note that passive MR damper control modes will only have the number of HDLRB as the design variable. The boundary of nRB is [3, 25], with the lower boundary satisfying the gravity load capacity demand and the upper boundary approaching negligible isolation effect. The boundaries of the RILD controller design variables for semi-active control are (0, 20) for ω_f and (0, 1) for η. The candidate learning scenarios to conduct RTHS test are sampled over the learning space. The Latin Hypercube Sampling (LHS) technique (Olsson, Sandberg et al. 2003) is adopted here for its sampling efficiency, especially for a multi-dimensional sampling space. To illustrate the learning convergence on RMSE of the time history response prediction of the MR damper substructure, the function to terminate the looping of RTHS tests is disabled in the actual RTHS tests to collect all the candidate learning scenario data.

For the input data considered for training the LSTM metamodel, 4 inputs (i.e., input displacement, velocity, current, and desired force from the primary semi-active controller) are considered for the semi-active mode; while 2 inputs (i.e., input displacement and velocity) are considered for passive-on and passive-off modes. Note that since the primary controller affecting the MR damper performance is the RILD controller and can be replaced with any other semi-active controllers based on needs, the desired force of the primary semi-active controller for the MR damper is included (rather than the controller parameters) as input data for improved training accuracy. Based on the complexity of the learning task, the semi-active mode with more input

control variables is expected to be more difficult to train comparing to the passive modes. For the learning convergence criteria, a RMSE absolute gradient normalized over every 2 learning accumulation steps (i.e., $2 \cdot \Delta i$ RTHS tests) and a negative RMSE gradient of the current step are adopted. The convergence criterion on the normalized RMSE absolute gradient is set as 1%. Figure 6.7-6.8 presents the RTHS collected total candidate learning scenarios and the training scenarios when learning convergence is reached, for semi-active, and passive-off/on modes. As observed, more scenarios are needed for the training of the LSTM metamodel on semi-active mode than passive-off/on modes due to its complexity.

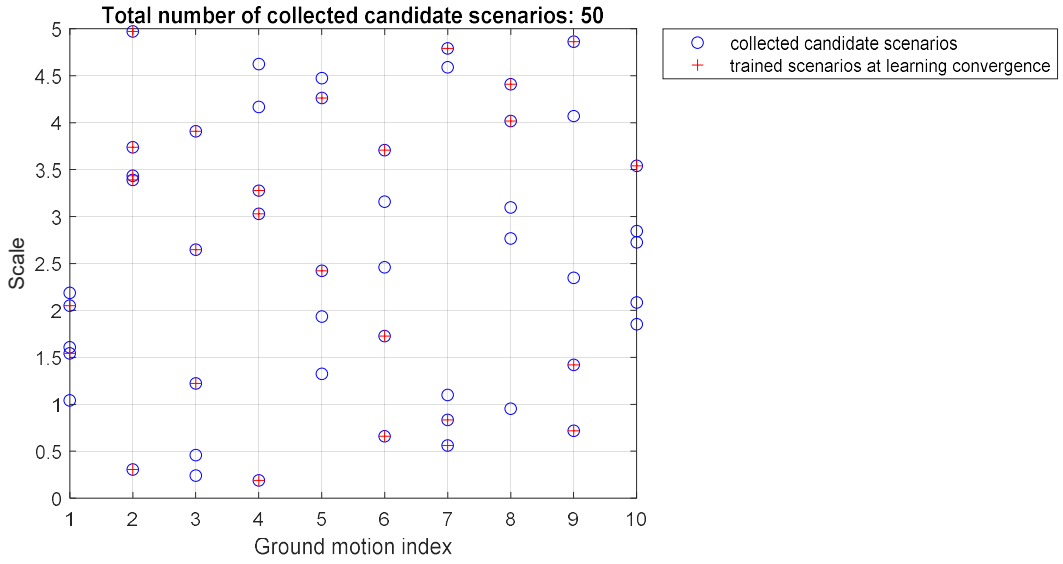

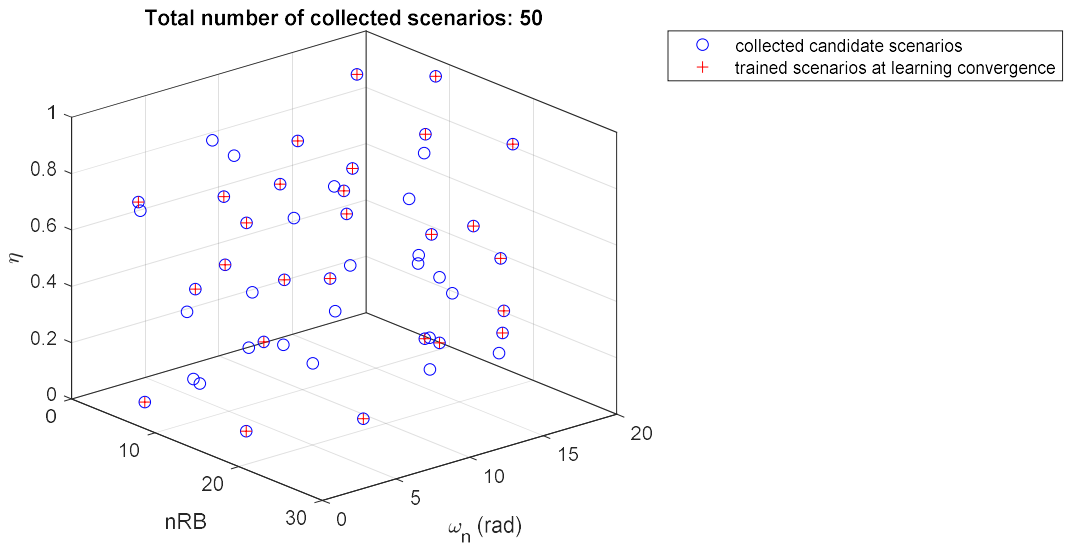

Figure 6.7 Collected candidate learning scenarios and trained scenarios on learning convergence for semi-active mode of the MR damper

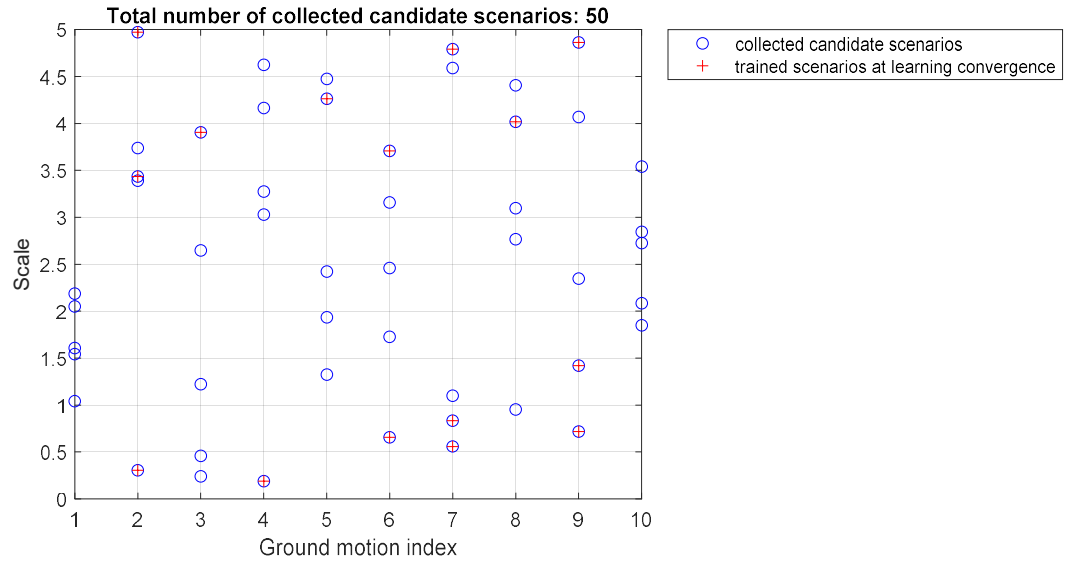

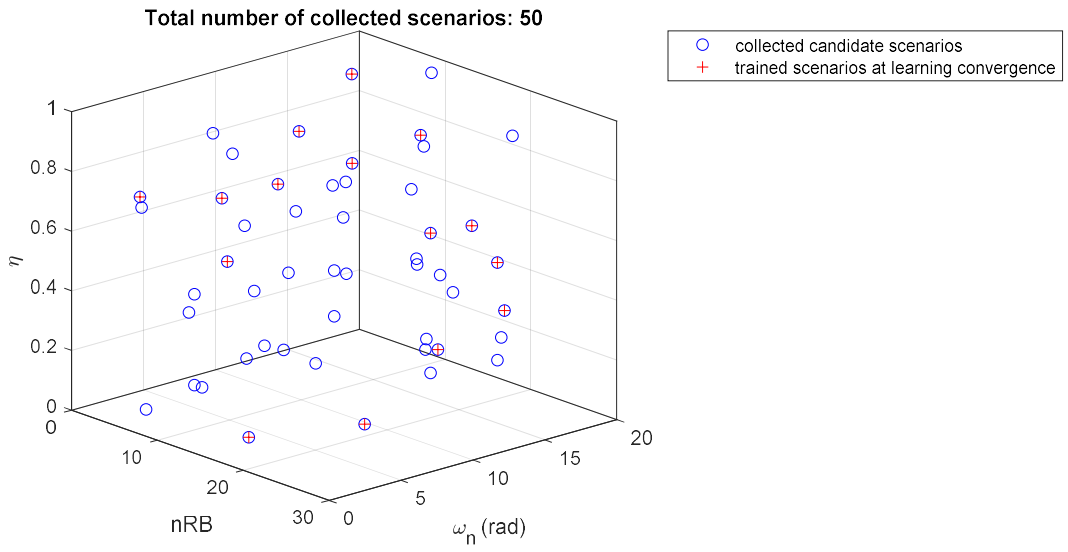

Figure 6.8 Collected candidate learning scenarios and trained scenarios on learning convergence for passive-off/on modes of the MR damper

Figures 6.9-6.11 summarize the LSTM online learning convergence for the three modes of the MR damper physical substructure. It can be seen that the semi-active mode takes more accumulation steps (9 steps) to reach learning convergence comparing to that (5 steps) of the passive off/on modes. The converged LSTM component metamodel shows an adequate prediction accuracy on the test data set considering the restoring force range, with the RMSE of the time history response prediction within 4 kN for all three modes. The RMSE at converged step is the smallest for passive-off mode and the largest for passive-on mode, with semi-active mode in between. This is possibly due to the increasing range of MR damper restoring force from passive-off to semi-active to passive-on modes. Note that the MR damper capacity is nominally 200 kN under passive-on mode, while the observed range of MR damper restoring force under the learning scenarios are within 100 kN for the passive-on mode. This is due to the downscaling of the MR damper inputs to

ensure safety (i.e., actuator stroke and velocity limits) as discussed in Section 4.3.5 and 6.3.2.

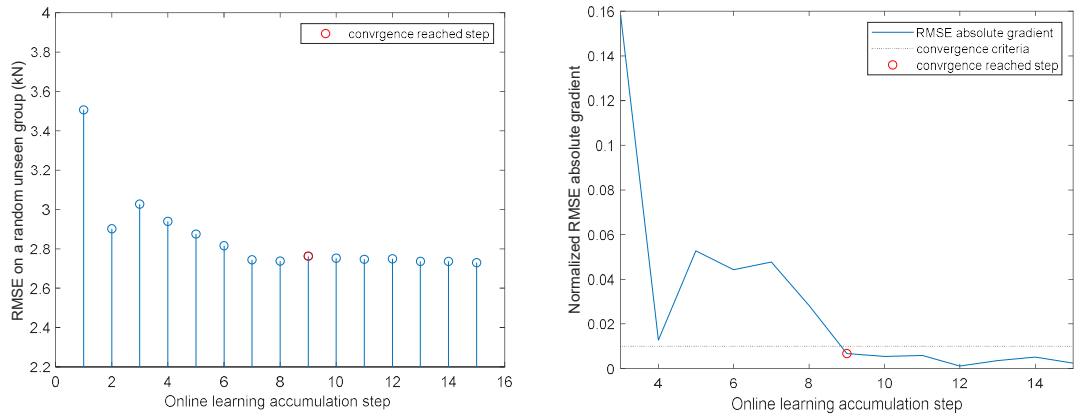

Figure 6.9 LSTM online learning convergence on RMSE for the semi-active mode of MR damper

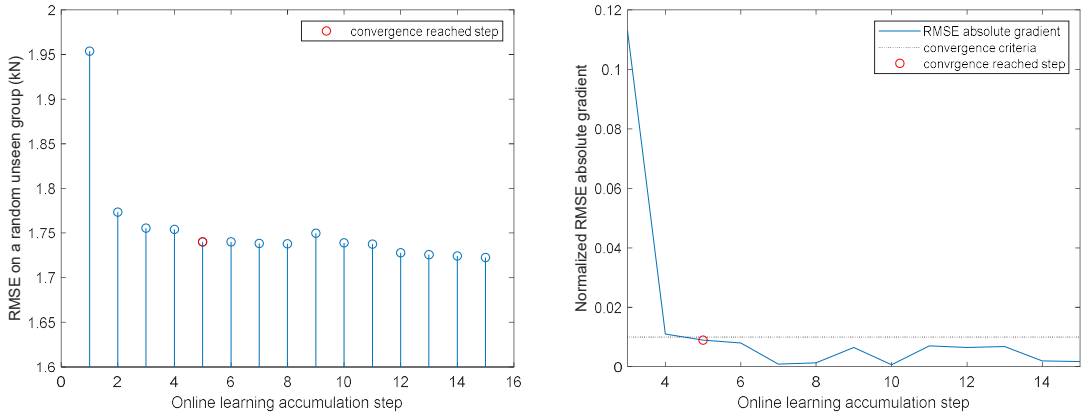

Figure 6.10 LSTM online learning convergence on RMSE for the passive-off mode of MR damper

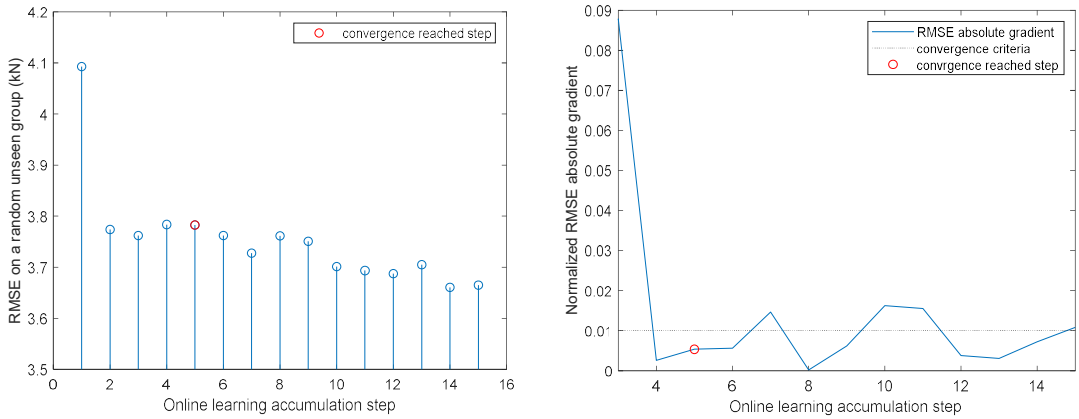

Figure 6.11 LSTM online learning convergence on RMSE for the passive-on mode of MR damper

To demonstrate the improvement during online learning steps of the LSTM component metamodel, Figures 6.12-6.14 present the time history response prediction on the MR damper restoring force over learning accumulation steps, under semi-active, passive-off, and passive-on modes for randomly selected unseen scenarios (i.e., scenarios that are not fed for the training of the LSTM neural network). The converged step is boxed for the learning accumulation of each MR damper mode. It can be seen that larger improvements on prediction are observed in the initial learning accumulation steps, while the later steps have relatively minor improvements, which is more measurable through the RMSE reduction (Figure 6.9-6.11). In addition, Figure 6.15-6.17 provides the MR damper restoring force prediction of the LSTM component metamodel, with respect to the MR damper inputs (i.e. displacement, velocity, and command current) for the semi-active mode under a random unseen scenario. This serves as an example to evaluate the input-output predictive mapping of the LSTM component metamodel. Similarly, the improvements on prediction performance are larger in the initial learning accumulation steps then the later steps.

The prediction evaluated at each input variable to output is observed with some discrepancies at the converged step, which is potentially due to the regularization of the LSTM component metamodel over the learning space of a large range of magnitude and frequency contents. However, the overall behavior for each input to output is captured and the final output restoring force prediction still holds a good agreement with the actual measured force (Figure 6.12).

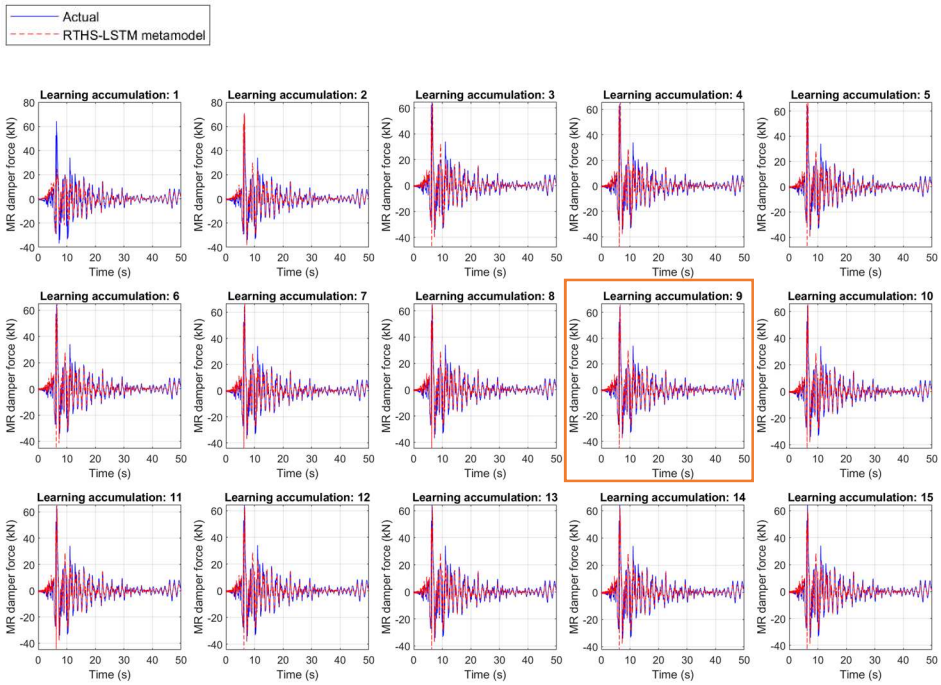

Figure 6.12 LSTM component metamodel prediction over learning accumulation steps on a random unseen scenario for the MR damper under semi-active mode

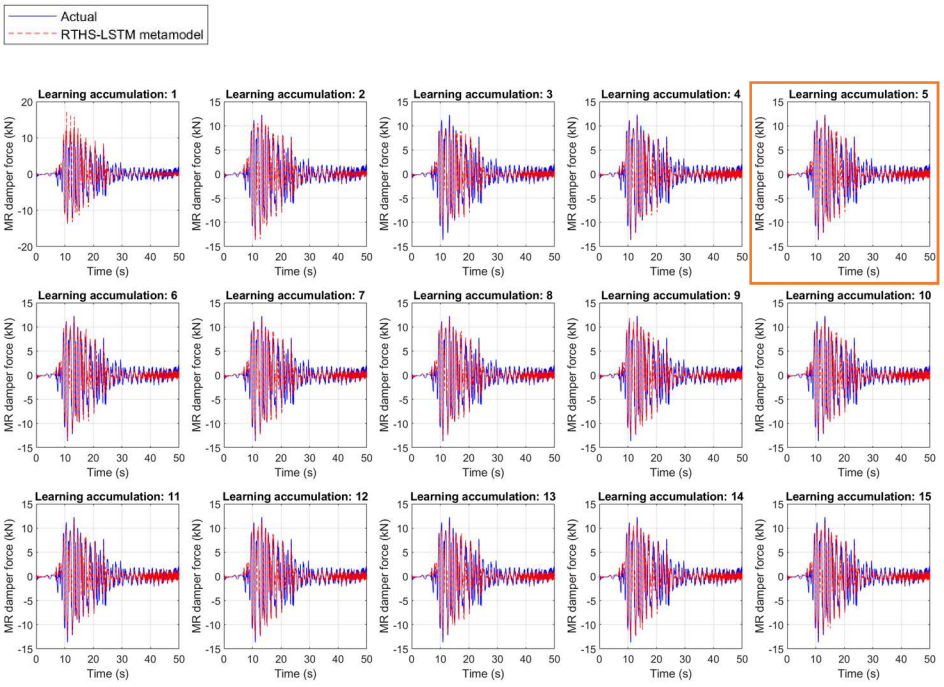

Figure 6.13 LSTM component metamodel prediction over learning accumulation steps on a random unseen scenario for the MR damper under passive-off mode

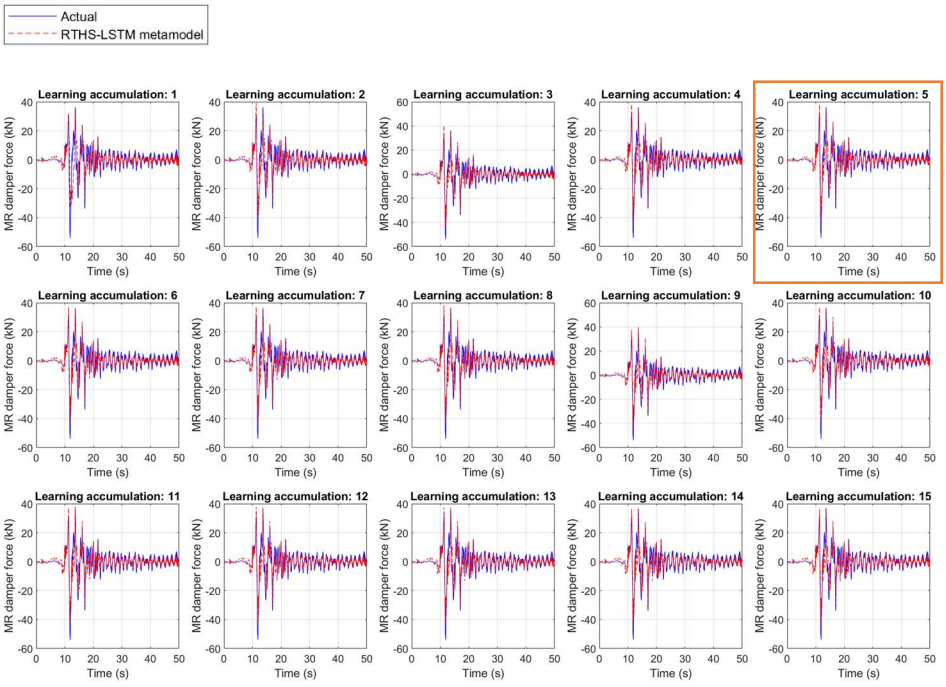

Figure 6.14 LSTM component metamodel prediction over learning accumulation steps on a random unseen scenario for the MR damper under passive-on mode

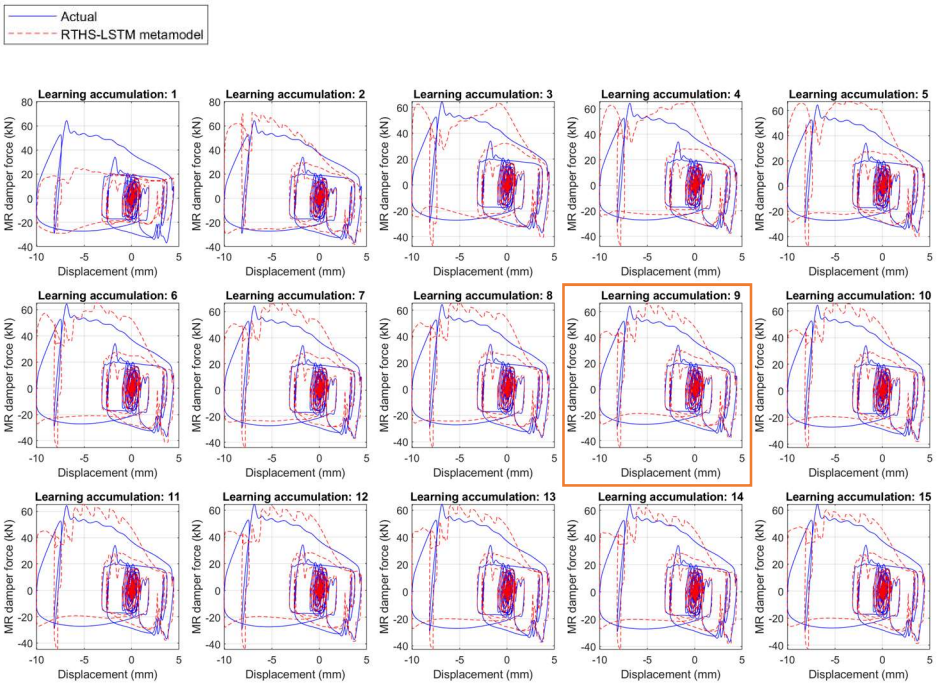

Figure 6.15 LSTM component metamodel prediction versus input displacement over learning accumulation steps on a random unseen scenario for the MR damper under semi-active mode

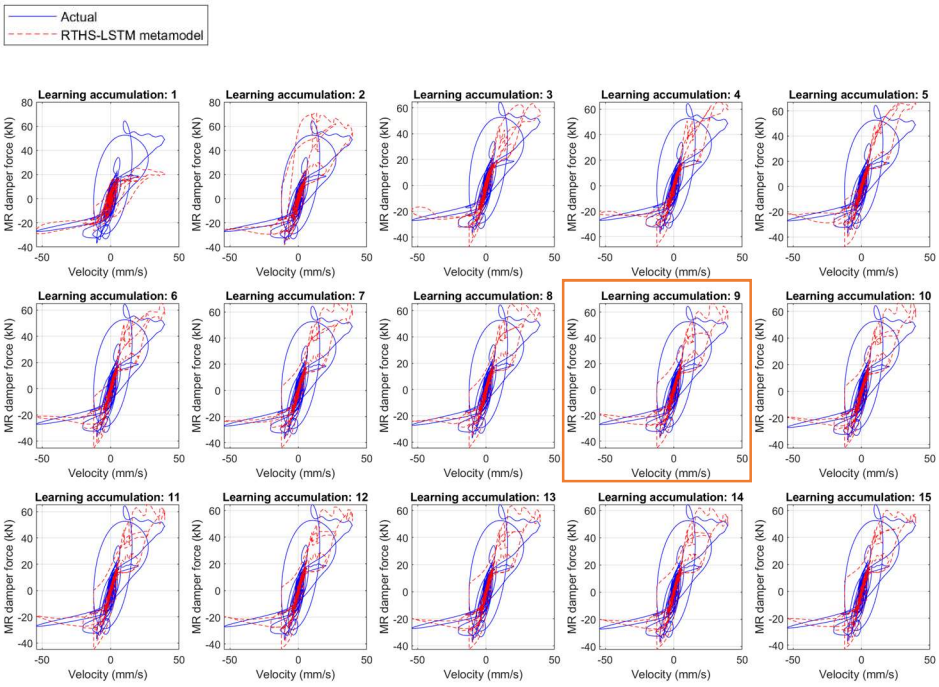

Figure 6.16 LSTM component metamodel prediction versus input velocity over learning accumulation steps on a random unseen scenario for the MR damper under semi-active mode

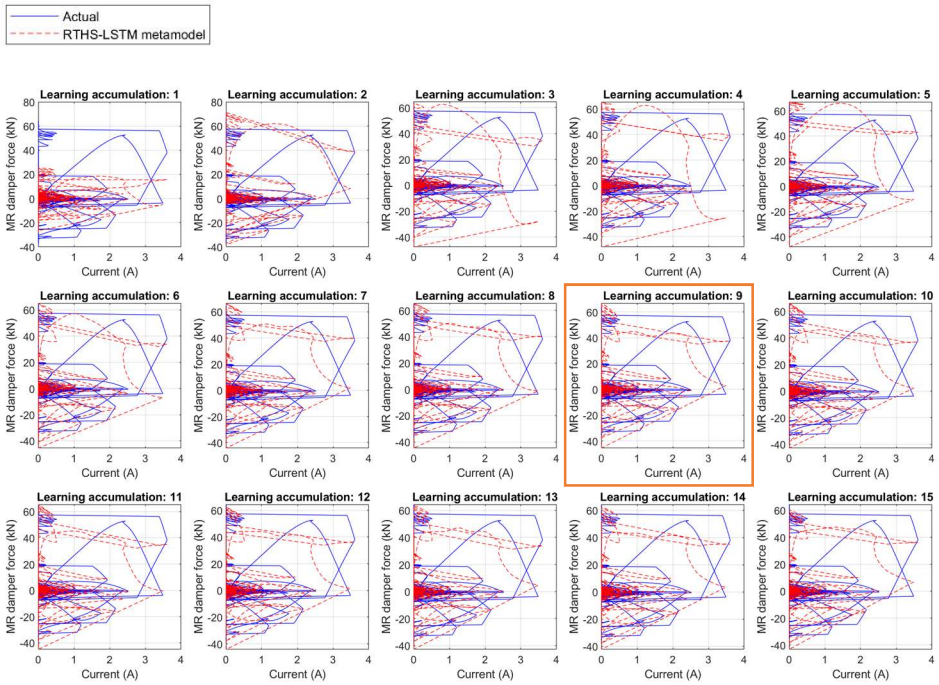

Figure 6.17 LSTM component metamodel prediction versus input command current over learning accumulation steps on a random unseen scenario for the MR damper under semi-active mode

To further verify the robustness of the LSTM component metamodel, the prediction performance of the metamodel is also compared with the phenomenological model of the MR damper discussed in Section 4.3.2, with the MR damper inputs of the RTHS tests. Figure 6.14 compares the performance of the LSTM component metamodel with the phenomenological model on couple randomly selected unseen scenarios for the semi-active mode, where they are both compared with the actual time history response of the MR damper measured in RTHS test. These comparisons demonstrate an overall good performance of the LSTM component metamodel in capturing the MR damper behavior. Comparing to the

phenomenological model, the LSTM component metamodel prediction shows an improved performance for scenarios with characteristics (e.g., frequency contents) that may not be covered for the calibration of the phenomenological model (Figure 6.18, left). At the higher bound of the force range (Figure 6.18, right), although it is observed with slightly more discrepancies comparing to the phenomenological model, the overall prediction performance still sufficiently captures the MR damper behavior. This slight discrepancy at higher bound is potentially due to the downscale of the inputs into the MR damper for safety concerns, which led to less samples reaching the higher bound. This could be improved by allowing more samples to cover the higher bound with a larger capacity actuator that allows less downscale governed by safety limits. In this case study, the converged LSTM component metamodel for the three modes of the MR damper substructure demonstrate adequate prediction accuracy and are used in the following fragility analysis as an approach to integrate the contribution of RTHS.

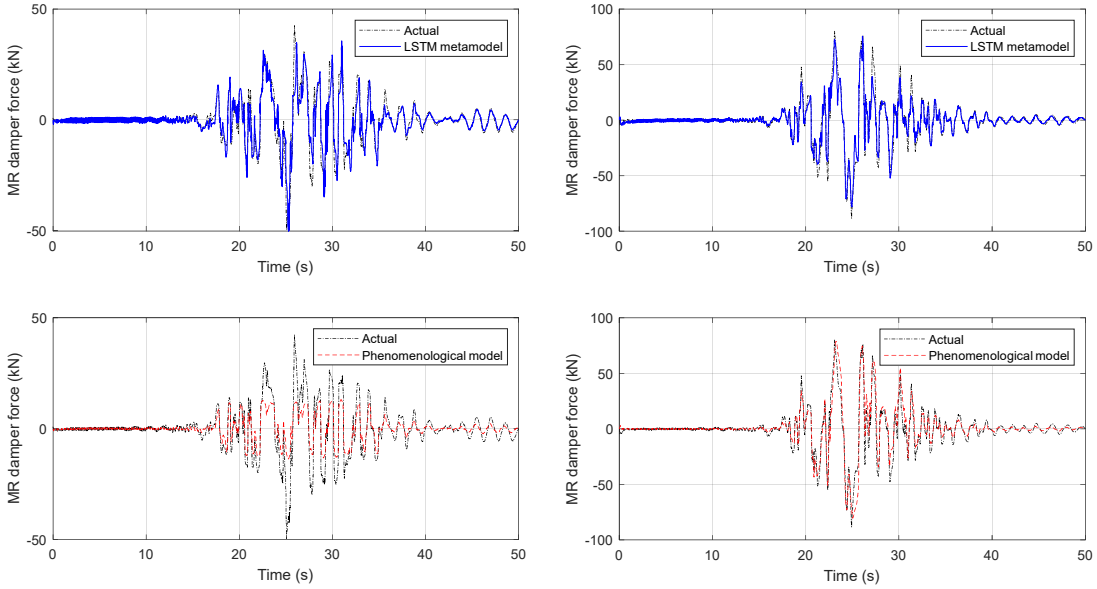

Figure 6.18 Performance of LSTM component metamodel compared to the phenomenological model of the MR damper in semi-active mode on two random unseen scenarios (left and right)

A final point to note for the proposed LSTM online learning approach is its significantly reduced experimental cost/time. Table 6.2 compares the number of experiments needed for the LSTM online learning approach for NN-PSO, and IDA directly using RTHS for NN-PSO. Note that it only evaluates the experimental cost without accounting the following computational cost in the NN-PSO process. Another thing to note is that the estimation on the number of experiments needed for the LSTM online learning approach is based on the semi-active mode of the case study. Table 6.2 clearly suggests that using LSTM online learning approach could provide a significant reduction on the needed experimental cost/time, with only 0.54% of the experimental cost/time needed to conduct RTHS integrated IDA as Section 4.2 discussed for the training data collection of the CPS-NN-PSO seismic resilience optimization approach.

Table 6.2 Comparison on RTHS experimental cost/time

CPS approach for NN fragility metamodeling	Direct use of RTHS in IDA	LSTM online learning
Number of experiments estimated	5000	27
Normalized experimental cost/time	100%	0.54%

6.3.4 NN training of fragility metamodel

Following the methodology introduced in Section 5.2 and Figure 5.1, RTHS is integrated into the NN fragility metamodeling by conducting IDA/MGSS-IDA with the trained LSTM component metamodel. To obtain the moments of the lognormal

distribution used for the fragility curve construction for the later loss/recovery analysis and optimization on the seismic resilience, the considered damage states with corresponding limit state thresholds of the retrofitted building with inter-story isolation are summarized in Figure 6.19. The limit states of the substructure (i.e., the structure below the isolation layer) and the superstructure (i.e., the structure above the isolation layer) are defined similarly as Section 4.1.3 discussed, through the combination of limit states on maximum inter-story drift and floor acceleration response from HAZUS (MRl 2003) and the residual inter-story drift for life safety and collapse prevention limit states from ASCE/SEI 41-13 (Engineers and Institute 2014). Note that the threshold being exceeded first during IDA will be the governing criteria of the corresponding limit state. In this study, limit states for the substructure, superstructure, and isolation later are considered separately due to their fundamentally different dynamic behavior. The substructure and superstructure are categorized as MRF for selecting the limit state values. For the isolation layer, maximum shear strain is considered as the measure for limit states (Zhang and Huo 2009). For the loss analysis to evaluate seismic resilience, the construction cost of the isolation layer is assumed to be 5% of the total building replacement cost (Padgett, Dennemann et al. 2010, Kelly and Konstantinidis 2011), and the superstructure and substructure are assumed to equally share the rest of the 95% of the total building replacement cost. For the cost ratio associated with different DS for the isolation layer, similarly as the proportions between its limit state thresholds, the cost ratio is assumed with 10% for SD, 40% for MD, 70% for ED, and 100% for CD, with respect to the construction cost of the isolation layer.

Damage States				No damage	SD	MD	ED	CD
Limit Sates Criteria	Structural		θ_{max}	0.6%	1.2%	3%	8%	
			$\theta_{res,max}$			1%	5%	
	Non-structural	Drift-sensitive	θ_{max}	0.4%	0.8%	2.5%	5%	
		Acceleration-sensitive	a_{max}	$0.3g$	$0.6g$	$1.2g$	$2.4g$	
	Isolation bearing		γ_{max}	100%	150%	200%	250%	

Figure 6.19 Damage states and corresponding limit states criteria for the retrofit building with inter-story isolation

For the training data collection, considering the large number of structure components (substructure, superstructure, and the isolation layer) with increased number of limit states (28 limit states in total), the IDA is adopted instead of the MGSS-IDA to interpolate the limit state values with better computational efficiency when associated with larger number of limit states. The incremental step of IDA is selected as 0.2 intensity scale with cap intensity scale at 5, which follows the same space defined for the LSTM component metamodel learning space. The moments (θ and β) of the lognormal distribution of the fragility curves for the 28 DS considered are collected using MLE (when all the limit states are exceeded under all scenarios) or truncated MLE (when the limit states are partially exceeded under all scenarios) as the output training data from IDA. Note that since the inter-story isolation layer is expected to provide a good protection for the superstructure, some severe limit states are not exceeded at all or only exceeded under couple scenarios. In this case, the fragility functions cannot be accurately fit using truncated MLE and it is assumed that these limit states have zero probability of exceedance considering that the probability is very low at the spectral acceleration at structural fundamental natural period. The inputs of the training data include the 5% damped spectral accelerations ($Sa(T_1, 5\%)$) of the considered ground motion suite at the structural natural periods and the design

variables (nRB, ω_f, and η). Note that $Sa(T_1, 5\%)$ is considered for the substructure and the superstructure at their fundamental natural periods separately. Additionally, the fundamental natural period of the superstructure varies depending on the design of the isolation layer. The training scenarios are sampled using LHS over the same learning space for the design variables as defined in section 6.3.2 (nRB within [3, 25], ω_f within (0, 20), and η within (0, 1).). Note that for the passive-off/on modes of the MR damper, the only design variable is nRB. The ground motion suite and intensities scales are covered during the IDA process and therefore no need for sampling. For this case study, samples of 20 design scenarios (Figure 6.20) are sampled for the NN fragility metamodeling. Each sample is evaluated under using the IDA approach.

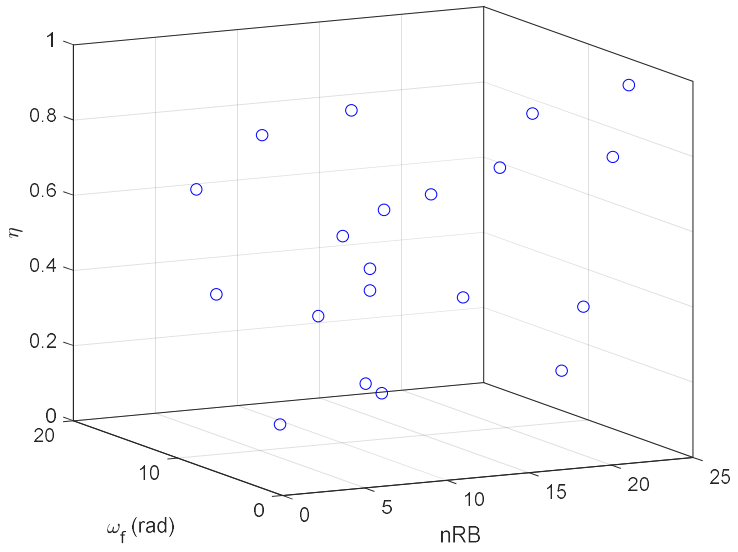

Figure 6.20 Sampled design scenarios using LHS for the NN fragility metamodeling

For the setting of the NN fragility metamodel, similar as Section 5.2.2 discussed, the backpropagation (BP) NN with Levenberg-Marquardt training algorithm is adopted to train the NN fragility metamodel. The log-sigmoid transfer function is used for the hidden layers and the linear transfer function is set for the

output layer. A random division of 80% of the full collected data set is used as training set, while the other 10% for validation set and 10% for test set. The early stopping criteria is set with 500 iterations and 50 retraining cycles are conducted to find the trained network with best generalization. Two networks are trained for the output of θ and β separately. Both networks use a 23-20-20-28 NN configuration (i.e. 23 inputs, 28 outputs, with 20 neurons for both the first and second hidden layer, respectively) for its good performance.

Hybrid isolation (i.e., isolation bearings with supplemental damping device) with MR damper in semi-active mode is the main retrofit strategy considered for optimization and illustrated here. The NN fragility metamodeling is conducted for the passive-off/on modes similarly as the semi-active mode, and evaluated for optimal seismic resilience in the following section in parallel for comparison purpose. Figure 6.21 shows the predicted θ and β for all 28 DS with the trained NN fragility metamodel comparing to that obtained from MLE or truncated MLE based on IDA results, for hybrid isolation layer in semi-active mode. The data shown in the comparison include the training set, validation set and test set, therefore includes not only seen data but also unseen data. Note that the most severe limit states for the isolated superstructure are rarely exceeded and assigned with zero probability, which is not included in the figures. The correlation coefficient (R_{NN}) between the NN prediction and the IDA obtained values shows the goodness of the prediction, with the perfect prediction having $R_{NN} = 1$. The perfect prediction is also plotted as "IDA = NN prediction" in the figure for reference. The trained NN fragility metamodel illustrates a good prediction performance on the full data set. Further, the performance of the NN fragility metamodel is evaluated on the final resilience curve

prediction under couple randomly selected unseen design scenarios (Figure 6.22 and Table 6.3), through comparison with the resilience curve obtained directly from IDA. The final obtained resilience curve further confirms a reliable prediction accuracy of the NN fragility metamodel.

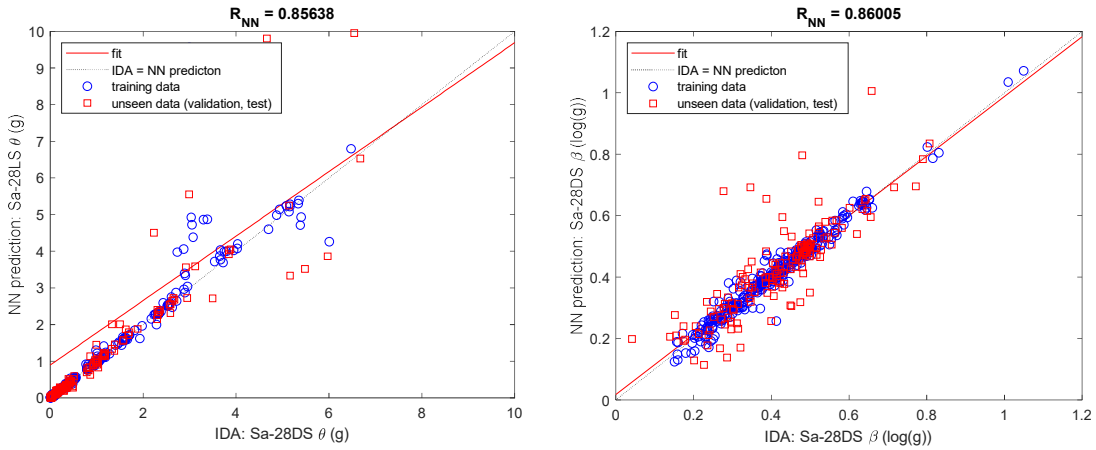

Figure 6.21 Trained NN fragility metamodel prediction performance on lognormal distribution moments for the hybrid isolation layer in semi-active mode

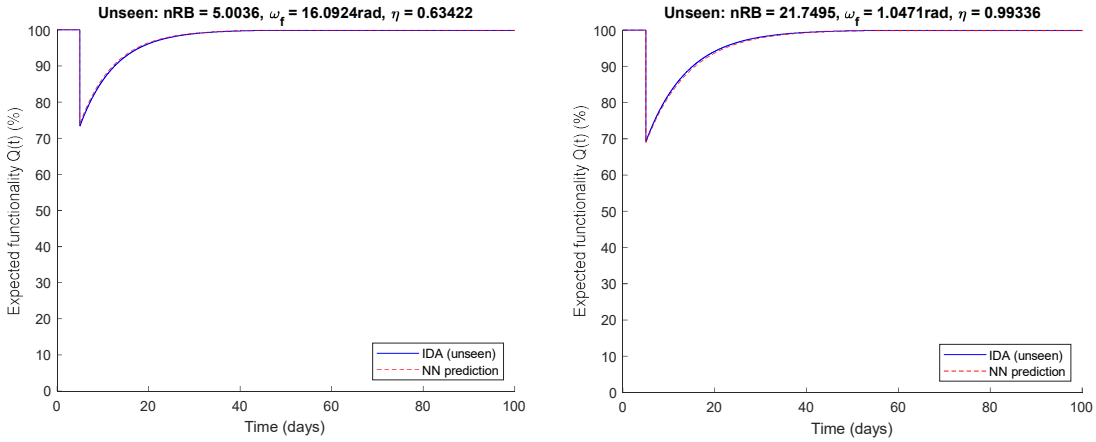

Figure 6.22 NN fragility metamodel prediction performance on structural seismic resilience curve under two random unseen design scenarios

6.3.5 Seismic resilience optimization with NN metamodels

With the trained NN fragility metamodel, the optimization of design variables for seismic resilience index are then enabled using PSO as discussed in Section 5.2.1. The inertia weight of the PSO process is selected as 1 for a good balance between

global and local exploration. The search space of the design variables is constrained by the learning space covered by the NN training set. Five particles are selected for the population with initial particle positions are determined using LHS over the search space for an adequate global exploration. The PSO iterations are set to terminate at 100 iterations if convergence cannot be reached before that. The convergence criterion is set through the absolute gradient normalized over every 5 iterations to be smaller or equal to 10^{-12}, due to the relatively smaller change of value in terms of the lumped resilience index. Note that the natural period and the corresponding spectral acceleration are updated during the optimization process based on the changing design of the isolation layer. For the semi-active mode of the MR damper, the CPS-NN-PSO process to converge on the optimal particle positions (i.e., the design parameter values) is given in Figure 6.23. The design variables for the inter-story isolation with MR damper in semi-active mode converged at 3 for *nRB*, 13.85 rad for ω_f, and 0.37 for η. The resulting optimal solution for the MR damper in semi-active mode is assessed through the NN fragility metamodel, with resilience index $\mathrm{R} = 95.28\%$, seismic loss $\mathrm{L} = 25.15\%$, and recovery time $T_{RE} = 40$ days. Figure 6.24-25 summarizes the corresponding iteration history of the seismic loss L and recovery time T_{RE}. It can be seen that with the increasing R index during the optimization process, the seismic loss L and recovery time T_{RE} are both reduced. Note that the iteration history is plotted for the global best design candidate at each iteration, therefore the improvement from the initial iteration step to the converged step is not shown as significant in Figure 6.24-25.

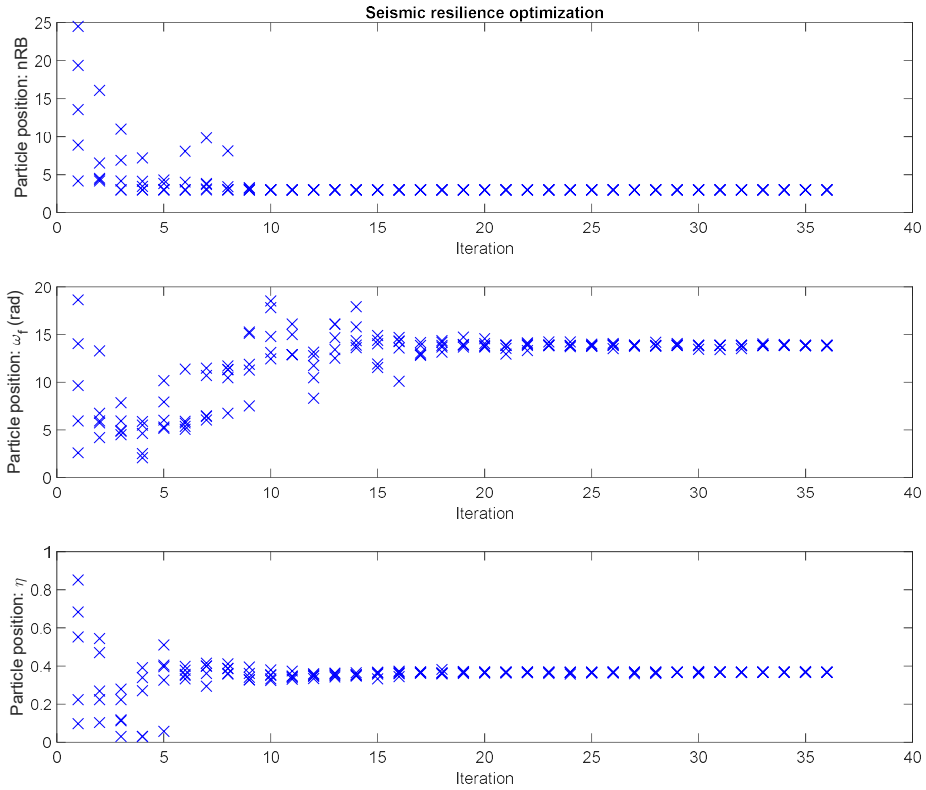

Figure 6.23 NN-PSO converging process for optimization on structural seismic resilience for the design of the inter-story isolation with MR damper in semi-active mode

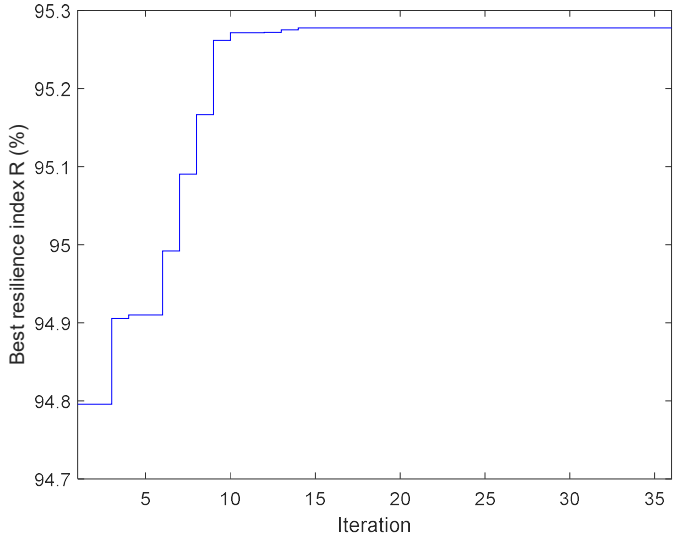

Figure 6.24 NN-PSO iteration history on structural resilience index R for the design optimization of the inter-story isolation with MR damper in semi-active mode

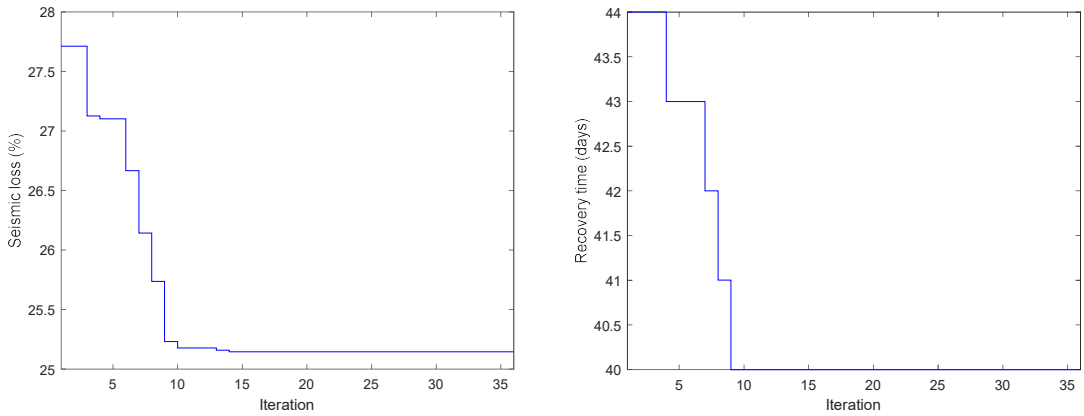

Figure 6.25 NN-PSO iteration history on seismic loss and recovery time for the design optimization of the inter-story isolation with MR damper in semi-active mode

The NN-PSO optimal design solution, which is an unseen design scenario for the training of the NN fragility metamodel, is validated with the seismic resilience evaluation result based on IDA as Figure 6.26 and Table 6.3 shows. The good agreement between the seismic resilience of the NN-PSO optimized solution and that of the optimal design evaluated based on IDA further confirms the accuracy of the NN fragility metamodel. Comparing the NN-PSO found optimal design to the previously validated random unseen design scenario given in Figure 6.22, an obvious improvement in seismic resilience is observed, in terms of both reduced seismic loss and recovery time. Detailed comparison is given in Table 6.3.

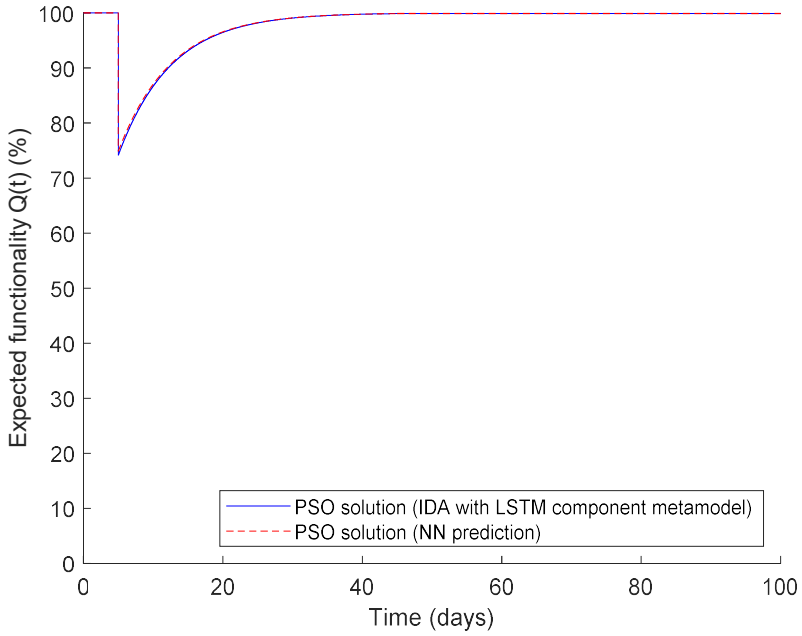

Figure 6.26 Validation on the seismic resilience of the NN-PSO found optimal design

Table 6.3 Validation of NN fragility metamodel predicted and NN-PSO found optimal design on seismic resilience with results based on IDA

Design scenario (MR damper in semi-active mode)	Random unseen scenario 1		Random unseen scenario 2		NN-PSO optimal solution	
	$nRB = 5$ $\omega_f = 16.09$ rad $\eta = 0.63$		$nRB = 21.75$ $\omega_f = 1.05$ rad $\eta = 0.99$		$nRB = 3$ $\omega_f = 13.85$ rad $\eta = 0.37$	
	NN fragility metamodel	IDA	NN fragility metamodel	IDA	NN fragility metamodel	IDA
Seismic loss (L)	25.92%	26.65%	30.66%	30.86%	25.15%	25.86%
Recovery time (T_{RE})	40 days	41 days	47 days	48 days	40 days	40 days
Seismic resilience index (R)	95.13%	95.00%	94.24%	94.20%	95.28%	95.14%

For comparison purpose, the same CPS-NN-PSO process is performed for the inter-story isolation design with MR damper in passive-off/on modes with the single

design variable *nRB* converged at the same optimal solution, which is the lower boundary of the search space (*nRB* = 3). This also provides a fair comparison between the isolation design with MR damper in semi-active mode and the passive-off/on modes. For comparison, the original structure and another retrofit scenario without inter-story isolation are considered. In the case of retrofit without inter-story isolation, the upper stories duplicate the MRF-DBF lateral system of the lower stories with or without addition viscous dampers. In the case of with additional viscous dampers installed for the upper three stories, it is tuned to provide 10% damping in the first mode of the total structure. In the case of without additional viscous dampers installed, the original 3-story structure with 10% damping at its first mode (natural period at 0.97s) changes to 4.4% damping at the first mode (natural period at 2.26s) for the total retrofitted 6 story structure without inter-story isolation.

To evaluate the optimized design for seismic resilience (i.e. the CPS-NN-PSO solution), the comparisons are extended with a design candidate using traditional optimization approach through PSO with a typical objective function and constraint. The traditional optimization of structural control is based on deterministic analyses for the considered ground motion suite at the original scale. The objective is defined as minimizing the acceleration response of the isolation layer, with the constraint on the drift response of the isolation layer to be not beyond moderate damage state (i.e. shear strain lower than 200% as given in Figure 6.19) satisfying a life safety performance. The convergence criterion is set as the absolute gradient of the isolation layer acceleration response within the last five iterations is below 1×10^{-4}. The PSO iterations on the design variables of the hybrid isolation layer are plotted in Figure

6.27. It can be seen that the converged solution (nRB = 5.25, ω_f = 1.64 rad, η = 0.68) is different from the NN-PSO solution showing in Figure 6.23.

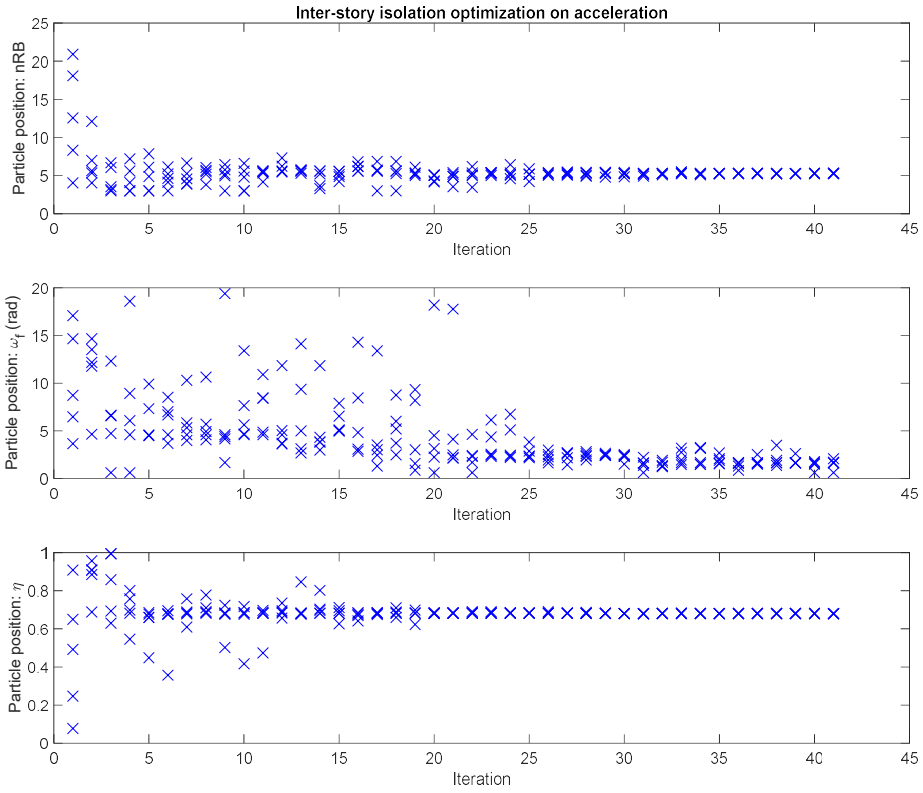

Figure 6.27 PSO converging process for optimization on isolation layer acceleration response for the design of the inter-story isolation with MR damper in semi-active

Figure 6.28 shows the comparison on actual IDA results between different retrofit designs. The figure suggests that the solution found using NN-PSO of the hybrid isolation with MR damper in semi-active mode provides the best seismic resilience for the retrofitted building. It is noted that the major contribution to the improvement of seismic resilience is from the inter-story isolation. The installation of MR damper could further improve the seismic resilience in both passive-off (i.e., providing low damping) and semi-active mode, where the semi-active mode performs slightly better than the passive-off mode. The improvement from passive-off mode to

semi-active mode is limited in this case, which is likely due to the supplemental control variables under optimization are only for the MR damper with limited influence to the seismic resilience of the total structure. With that being said, the proposed CPS-NN-PSO approach is still able to efficiently achieve improvement on seismic resilience, and more significant improvement may be observed for a different case with more design variables under optimization. The MR damper in passive-on mode slightly reduces the seismic resilience of the inter-story isolated retrofit building, potentially due to larger acceleration response of the isolated superstructure and therefore larger story shear generated. Another thing to notice is that if the structure was retrofit without isolation, the seismic resilience would be reduced from the original structure even with additional viscous dampers installed for the added three stories to provide 10% damping in the first mode. This is likely because the lateral system of the substructure was not reinforced to account for the larger seismic mass. However, with inter-story isolation, the seismic resilience of the retrofitted structure is improved from the original structure even without supplemental damping from the MR damper. In addition, it is worth noting that the optimized design using a typical traditional optimization approach (i.e. minimizing acceleration response of the isolation layer with constraint on its drift response) provides a seismic resilience index lower (with higher seismic loss and longer recovery time) than NN-PSO solution for the semi-active mode, as well as that for the passive-off mode. This further reinforced the importance of the proposed approach for optimization on seismic resilience. The detailed comparison is summarized in Table 6.4.

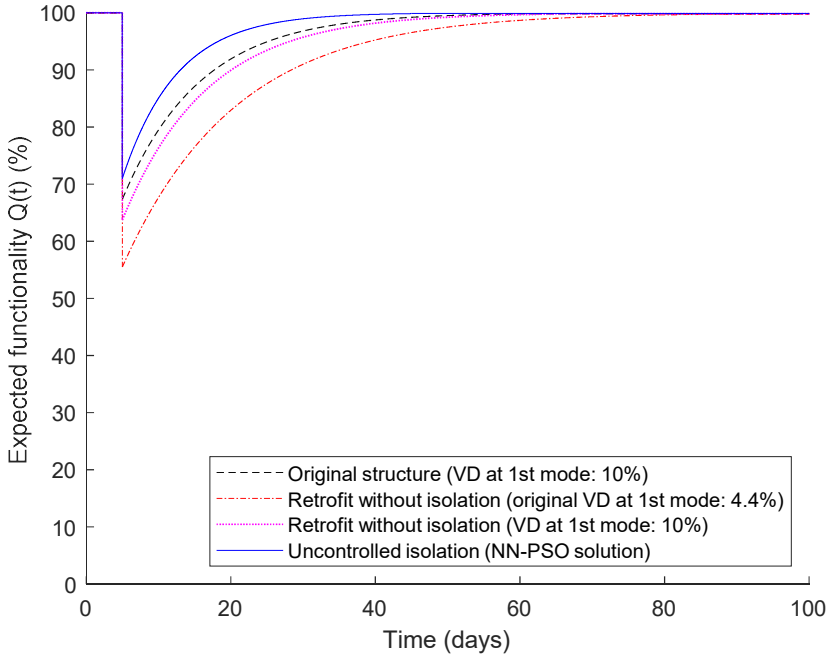

(a)

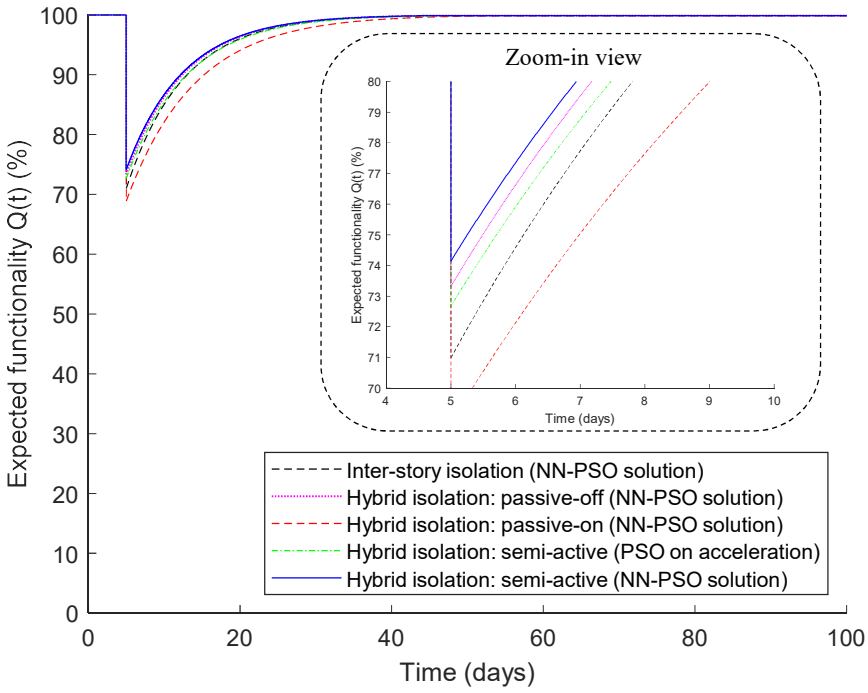

(b)

Figure 6.28 Comparison on seismic resilience between different designs

Table 6.4 Detailed comparison on seismic resilience between different designs

Design scenario	Original structure	Retrofit without	Retrofit without	Uncontrolled isolation	Hybrid isolation:	Hybrid isolation:	Hybrid isolation:	Hybrid isolation:

	(10% VD)	isolation (original VD, 4.4%)	isolation (10% VD)	(nRB = 3)	passive-off (nRB = 3)	passive-on (nRB = 3)	semi-active, PSO on acceleration (nRB = 5.25, ω_f = 1.64 rad, η = 0.68)	semi-active, NN-PSO (nRB = 3, ω_f = 13.85 rad, η = 0.37)
Seismic loss (L)	32.67%	44.51%	36.30%	29.02%	26.69%	31.12%	27.33%	25.86%
Recovery time (T_{RE})	57 days	83 days	62 days	40 days	40 days	48 days	42 days	40 days
Seismic resilience index (R)	93.86%	91.64%	93.18%	94.55%	94.99%	94.16%	94.87%	95.14%

The results demonstrate the accuracy of the NN fragility metamodel and its applicability for the optimization of structural seismic resilience. Including the experimental cost from the LSTM online learning process discussed in Section 6.3.3, Table 6.5 shows the efficiency of the combined CPS-NN-PSO approach compared to direct PSO based IDA with RTHS integrated (termed as CPS-PSO here). Note that the comparison is based on this case study; the specific computational/experimental cost may vary depending on different optimization problem and conditions. The PSO process used for comparison here has 5 particles and 36 iteration steps as Figure 6.23 shows. The CPS-NN-PSO computational/experimental time is considered only based on the computational/experimental time needed for collecting training data set, due to that the actual time of the PSO process using the trained NN metamodel is relatively very small. CPS-NN-PSO approach demonstrates great efficiency and significant reduction in computational/experimental cost, with only 11.17% computational time needed comparing to CPS-PSO based on IDA for this case study.

Table 6.5 Computational/experimental cost comparison between IDA-based CPS-PSO and CPS-NN-PSO

Seismic resilience optimization approach	CPS-PSO (IDA based)	CPS-NN-PSO (training based on IDA)
Number of analysis/experiment estimated	45000	5027
Normalized computational/experimental time	100%	11.17%

6.4 Summary

This chapter proposed an efficient cyber-physical structural seismic resilience optimization approach enabled by online learning neural networks. The online learning neural network is constructed using an LSTM neural network to efficiently integrate RTHS into the optimization approach proposed in Chapter 5. With the online learning LSTM neural network, a LSTM component metamodel can be obtained for the RTHS physical substructure to be used when creating the NN fragility metamodeling, requiring only a limited number of RTHS tests to be conducted. The proposed online learning approach significantly reduced the experimental cost/time needed to conduct RTHS integrated IDA for a cyber-physical fragility analysis and seismic resilience optimization.

A case study of a retrofit design to construct an additional three stories on top of a 3-story MRF-DBF structure is conducted to demonstrate the proposed LSTM component online learning approach and the CPS-NN-PSO optimization of seismic resilience. An inter-story isolation retrofit strategy is considered with supplemental damping provided by an MR damper. The design parameters of the retrofit are considered in the optimization process. The MR damper is evaluated in RTHS as physical substructure while the remainder of the structure is modeled numerically. The LSTM component metamodel is trained for the MR damper under these realistic

load and boundary conditions. The learned LSTM component metamodel demonstrated good performance in the prediction of the time history response of the MR damper restoring force over a large range of magnitude and frequency content. With the LSTM component metamodel integrated into the NN-PSO approach, combining a CPS-NN-PSO approach, the optimal design for the inter-story isolation with MR damper in semi-active mode is found with the best seismic resilience compared to other design candidates and retrofit strategies, including a candidate design optimized with a traditional optimization objective. A significant reduction in computational/experimental time is also observed for the CPS-NN-PSO in the case study. Through the case study, the effectiveness and efficiency of the proposed CPS-NN-PSO approach through LSTM online learning combined with the NN-PSO for seismic resilience optimization is demonstrated.

CHAPTER 7 CONCLUSION AND FUTURE STUDY

7.1 Conclusions

This dissertation leverages structural design decisions to improve the seismic resilience of civil infrastructure. To achieve resilient design, the dissertation proposes an efficient evaluation and optimization approach using deep neural networks. Moreover, the integration of cyber-physical systems to model structural components is proposed, improving the accuracy of the analysis by avoiding numerical errors of highly nonlinear components under complex design scenarios with large uncertainties. Time-saving methods are proposed to integrate physical testing into the evaluation and optimization process through additional component level metamodeling. The major conclusions and contributions are summarized in this section.

7.1.1 BMJ brace – reusable protection for aftershocks and quicker post-earthquake recovery

- A passive self-centering hysteretic damping brace is proposed to introduce the buckling mode jump (BMJ) mechanism, providing an alternative source of flag-shaped hysteresis damping that both avoids material yielding and is self-centering. Its damage-free and reusable feature could provide more seismic resilient design for steel braced structures, with reduced seismic vulnerability, redundant source of protection during aftershocks and less post-earthquake repair effort needed.
- An analytical model is derived and verified with finite element analysis to characterize the BMJ behavior for the capped column geometry and provide design guidance.

- The proposed BMJ brace is demonstrated to significantly reduce the residual inter-story drifts compared to conventional brace (CB) and provide a comparable reduction in peak responses with the buckling restrained brace (BRB), with a minor tradeoff on acceleration responses. The numerical study is based on a 3-story braced frame under a suite of 20 earthquake ground motions corresponding to the seismic hazard level of 10% exceedance in 50 years.

7.1.2 Cyber-physical structural seismic resilience evaluation framework

- A cyber-physical framework is proposed as a cost-effective tool to evaluate the seismic resilience of structural systems with highly nonlinear or rate dependent components that are difficult to model under complex design scenarios with large uncertainties. This approach integrates RTHS, IDA, fragility analysis, loss analysis, and recovery analysis.
- The proposed framework is demonstrated with improved accuracy compared to full numerical model through a case study of a 3-story steel moment frame with additional MR dampers as a retrofit option.
- A MGSS-IDA algorithm is developed with improved accuracy and considerably reduced computational cost comparing to IDA.

7.1.3 Structural optimization of seismic resilience with neural networks

- An approach is developed for seismic resilience optimization based on fragility metamodeling using deep NN, IDA/MGSS-IDA, and PSO algorithms, denoted as NN-PSO. The deep NN replaces the computationally (or experimentally) demanding IDA analysis in the optimization process.

- The proposed NN-PSO approach demonstrates a significant reduction in computational cost as compared to PSO based on IDA/MGSS-IDA for a numerical case study optimizing the proposed BMJ bracing system.

7.1.4 Efficient cyber-physical structural optimization of seismic resilience with online learning neural networks

- An online learning approach is developed using LSTM neural networks for the metamodeling of RTHS physical component. This metamodel is integrated into the NN-PSO approach, creating a combined as a CPS-NN-PSO approach. This approach reduces the number of experiments required when combining cyber-physical systems with optimization.
- The efficiency of the CPS-NN-PSO approach to perform optimization for seismic resilience is validated through a case study of the structural retrofit of a 6-story steel frame structure with inter-story isolation and supplemental MR damper control.
- The proposed CPS-NN-PSO approach leverages the deep learning capability of deep neural networks and the accuracy of cyber-physical systems to improve both efficiency and accuracy for optimization of seismic resilience.

7.2 Future Study

This dissertation presents a series of proof-of-concept studies on leveraging deep learning techniques and cyber-physical systems for more efficient and reliable evaluation and optimization of structural design for seismic resilience. Several exciting potential future studies are proposed as listed below.

- **LSTM metamodeling for RTHS physical component**: In this research, the LSTM metamodeling is conducted for MR damper, which is a nonlinear device but with repeatable behavior. This means that no residual plastic deformations are involved in the metamodeling using the proposed online learning LSTM neural networks. With the strong deep learning capability of the LSTM neural networks and the efficiency of the proposed online learning approach, it is promising to consider other type of nonlinearity for the physical substructure in RTHS with limited experimental cost under the large uncertainties associated with the risk-based context. For example, the time history response of nonlinear structural components with plastic residuals can be considered as sequential data with long-term dependences. In other words, when the behavior depends on the occurrence of plastic deformation in terms of time, location and extent, the resulted time history response may present a long-term dependency between the current behavior and the occurrence and extent of plastic deformation. LSTM neural networks are especially strong in learning such long-term dependencies and have a great potential for the metamodeling of this type of RTHS substructure under large uncertainties.
- **Cyber-physical evaluation and optimization for seismic resilience**: With the CPS-NN-PSO approach proposed in this research enabling a promising tool to perform efficient and reliable evaluation and optimization for structural seismic resilience, the integration of cyber-physical systems need not be limited to laboratory-scale RTHS. Actual structural response data collected from structural health monitoring sensors installed in structures could also be considered for the construction of a cyber-physical systems, which could contribute to a cyber-

physical metamodeling in the context of seismic resilience in the long-term. Additionally, existing experimental databases can be mined for the creation and calibration of neural network metamodels.

- **Deep learning for seismic resilience**: The research summarized herein mainly explored two types of deep neural networks, the multi-layer feedforward neural networks and the LSTM neural networks. Also, the training of these deep neural networks is conducted for specific regression type learning tasks with limited learning space. Some limitations on learning complex tasks with limited training data are observed in this research, which invites potential future study on optimizing deep neural networks training for complex tasks. On the one hand, other types of deep neural networks and the construction of optimal NN configuration can be further explored in the future for different learning tasks and needs (regression/classification), such as the convolutional neural networks (CNN) with strong capabilities in learning information from images. On the other hand, to further leverage the deep learning capability of deep neural networks, more complex learning tasks with large learning spaces can be considered for a better understanding on seismic resilience of different type of structures under different uncertain scenarios.
- **Seismic resilience evaluation and optimization for infrastructure systems**: The research presented in this dissertation focuses on the explicit quantitative evaluation and optimization of seismic resilience for individual building structures. This can be considered as a starting point to contribute to the seismic resilience through structural design for the system and community level. To further consider the seismic resilience at the level of infrastructure systems, future

studies are needed to better understand and model the interconnections between individual structural seismic performance and probabilistic losses with different functionalities.

REFERENCE

Adeli, H. (2001). "Neural networks in civil engineering: 1989–2000." Computer-Aided Civil and Infrastructure Engineering **16**(2): 126-142.

Adeli, H. and S.-L. Hung (1994). Machine learning: neural networks, genetic algorithms, and fuzzy systems, John Wiley & Sons, Inc.

Andradóttir, S. (1998). A review of simulation optimization techniques. Proceedings of the 30th conference on Winter simulation, IEEE Computer Society Press.

ANSYS, I. ANSYS® Academic Research.

Aoues, Y. and A. Chateauneuf (2010). "Benchmark study of numerical methods for reliability-based design optimization." Structural and Multidisciplinary Optimization **41**(2): 277-294.

ASCE (2010). Minimum design loads for buildings and other structures, Amer Society of Civil Engineers.

Ayyub, B. M. (2014). "Systems resilience for multihazard environments: Definition, metrics, and valuation for decision making." Risk Analysis **34**(2): 340-355.

Azuhata, T., et al. (2008). Earthquake damage reduction of buildings by self-centering systems using rocking mechanism. The 14th World Conference on Earthquake Engineering.

Baber, T. T. and Y.-K. Wen (1981). "Random vibration hysteretic, degrading systems." Journal of the Engineering Mechanics Division **107**(6): 1069-1087.

Baker, J. W. (2015). "Efficient analytical fragility function fitting using dynamic structural analysis." Earthquake spectra **31**(1): 579-599.

Beale, M. H., et al. (1992). "Neural Network Toolbox™ User's Guide." The Mathworks Inc.

Bendsøe, M. P. and N. Kikuchi (1988). "Generating optimal topologies in structural design using a homogenization method." Computer methods in applied mechanics and engineering **71**(2): 197-224.

Benjamin, J. and C. Cornell (1975). Probability, statistics, and decision for civil engineers. 1970, New York: McGraw-Hill.

Bertero, R. and V. V. Bertero (2000). Application of a comprehensive approach for the performance based earthquake resistant design buildings. 12th World Conference on Earthquake Engineering, Auckland.

Bertero, R. D. and V. V. Bertero (2002). "Performance-based seismic engineering: the need for a reliable conceptual comprehensive approach." Earthquake Engineering & Structural Dynamics **31**(3): 627-652.

Bertero, R. D., et al. (1996). Performance-based earthquake-resistant design based on comprehensive design philosophy and energy concepts. Proceedings of 11th World Conference on Earthquake Engineering.

Bertero, V. V. (1996). State of the art report on: design criteria. Proceedings of 11th world conference on earthquake engineering, Acapulco, Mexico, Oxford, Pergamon.

Bruneau, M., et al. (2003). "A framework to quantitatively assess and enhance the seismic resilience of communities." Earthquake spectra **19**(4): 733-752.

Bruneau, M., et al. (2006). White paper on the SDR grand challenges for disaster reduction, Multidisciplinary Center for Earthquake Engineering Research.

Bruneau, M. and A. Reinhorn (2006). Overview of the resilience concept. Proceedings of the 8th US national conference on earthquake engineering.

Bruneau, M. and A. Reinhorn (2007). "Exploring the concept of seismic resilience for acute care facilities." Earthquake spectra **23**(1): 41-62.

Bucher, C. and T. Most (2008). "A comparison of approximate response functions in structural reliability analysis." Probabilistic Engineering Mechanics **23**(2-3): 154-163.

Budiansky, B. (1973). Theory of buckling and post-buckling behavior of elastic structures, DTIC Document.

Carrion, J. E., et al. (2009). "Real-time hybrid simulation for structural control performance assessment." Earthquake Engineering and Engineering Vibration **8**(4): 481-492.

Castaneda Aguilar, N. E. (2012). "Development and validation of a real-time computational framework for hybrid simulation of dynamically-excited steel frame structures."

Castaneda, N., et al. (2013). "Computational tool for real-time hybrid simulation of seismically excited steel frame structures." Journal of Computing in Civil Engineering **29**(3): 04014049.

Chambers, M. and C. Mount-Campbell (2002). "Process optimization via neural network metamodeling." International Journal of Production Economics **79**(2): 93-100.

Chandrasekaran, S. and S. Banerjee (2015). "Retrofit optimization for resilience enhancement of bridges under multihazard scenario." Journal of Structural Engineering **142**(8): C4015012.

Chang, C.-C. and P. Roschke (1998). "Neural network modeling of a magnetorheological damper." Journal of intelligent material systems and structures **9**(9): 755-764.

Chang, S. E. and M. Shinozuka (2004). "Measuring improvements in the disaster resilience of communities." Earthquake spectra **20**(3): 739-755.

Chatterjee, S., et al. (2017). "Particle swarm optimization trained neural network for structural failure prediction of multistoried RC buildings." Neural Computing and Applications **28**(8): 2005-2016.

Chen, C. and J. M. Ricles (2008). "Development of direct integration algorithms for structural dynamics using discrete control theory." Journal of engineering mechanics **134**(8): 676-683.

Christopoulos, C., et al. (2002). "Seismic response of self-centring hysteretic SDOF systems." Earthquake engineering & structural dynamics **31**(5): 1131-1150.

Christopoulos, C. and S. Pampanin (2004). "Towards performance-based design of MDOF structures with explicit consideration of residual deformations."

Christopoulos, C., et al. (2008). "Self-centering energy dissipative bracing system for the seismic resistance of structures: development and validation." Journal of Structural Engineering **134**(1): 96-107.

Chung, Y. S., et al. (1990). "Automatic seismic design of reinforced concrete building frames." Structural Journal **87**(3): 326-340.

Cimellaro, G. P., et al. (2005). Seismic resilience of a health care facility. Proceedings of the 2005 ANCER Annual Meeting, Session III, November 10–13, Jeju, Korea.

Cimellaro, G. P., et al. (2010). "Framework for analytical quantification of disaster resilience." Engineering Structures **32**(11): 3639-3649.

Council, B. S. S. (2000). "Prestandard and commentary for the seismic rehabilitation of buildings, FEMA-356." Federal Emergency Management Agency, Washington, DC.

Der Kiureghian, A. and O. Ditlevsen (2009). "Aleatory or epistemic? Does it matter?" Structural safety **31**(2): 105-112.

DesRoches, R., et al. (2004). "Cyclic properties of superelastic shape memory alloy wires and bars." Journal of Structural Engineering **130**(1): 38-46.

Dolce, M., et al. (2000). "Implementation and testing of passive control devices based on shape memory alloys." Earthquake engineering & structural dynamics **29**(7): 945-968.

Dolce, M., et al. (2005). "Shaking table tests on reinforced concrete frames without and with passive control systems." Earthquake engineering & structural dynamics **34**(14): 1687-1717.

Dong, B., et al. (2016). "Seismic response and performance of a steel MRF building with nonlinear viscous dampers under DBE and MCE." Journal of Structural Engineering **142**(6): 04016023.

Dong, L. and R. Lakes (2013). "Advanced damper with high stiffness and high hysteresis damping based on negative structural stiffness." International Journal of Solids and Structures **50**(14): 2416-2423.

Dong, L. and R. S. Lakes (2012). "Advanced damper with negative structural stiffness elements." Smart Materials and Structures **21**(7): 075026.

Dutta, A., et al. (2008). An innovative application of base isolation technology. Structures Congress 2008: 18th Analysis and Computation Specialty Conference.

Dyke, S., et al. (1996). "Modeling and control of magnetorheological dampers for seismic response reduction." Smart materials and structures **5**(5): 565.

Ellingwood, B. R., et al. (2007). "Fragility assessment of building structural systems in Mid-America." Earthquake Engineering & Structural Dynamics **36**(13): 1935-1952.

Enevoldsen, I. and J. D. Sørensen (1994). "Reliability-based optimization in structural engineering." Structural safety **15**(3): 169-196.

Engineers, A. S. o. C. and S. E. Institute (2014). Seismic Evaluation and Retrofit of Existing Buildings, American Society of Civil Engineers.

Erochko, J., et al. (2010). "Residual drift response of SMRFs and BRB frames in steel buildings designed according to ASCE 7-05." Journal of Structural Engineering **137**(5): 589-599.

Fajfar, P. (1999). Trends in seismic design and performance evaluation approaches. Earthquake Engineering-Invited Papers: Proceedings of the eleventh European conference, Paris, France, 6-11 September 1998, CRC Press.

Fragiadakis, M. and M. Papadrakakis (2008). "Performance-based optimum seismic design of reinforced concrete structures." Earthquake Engineering & Structural Dynamics **37**(6): 825-844.

Frangopol, D. M. and P. Bocchini (2011). Resilience as optimization criterion for the rehabilitation of bridges belonging to a transportation network subject to earthquake. Structures Congress 2011.

Frank McKenna, G. L. F., Michael H. Scott, Boris Jeremic Open System for Earthquake Engineering Simulation (OpenSees). Berkeley, CA, Pacific Earthquake Engineering Research Center.

Ganzerli, S., et al. (2000). "Performance-based design using structural optimization." Earthquake Engineering & Structural Dynamics **29**(11): 1677-1690.

Gasser, M. and G. I. Schuëller (1997). "Reliability-based optimization of structural systems." Mathematical Methods of Operations Research **46**(3): 287-307.

Ghobarah, A. (2001). "Performance-based design in earthquake engineering: state of development." Engineering Structures **23**(8): 878-884.

Gholizadeh, S. (2015). "Performance-based optimum seismic design of steel structures by a modified firefly algorithm and a new neural network." Advances in Engineering Software **81**: 50-65.

Gholizadeh, S. and M. Mohammadi (2016). "Reliability-based seismic optimization of steel frames by metaheuristics and neural networks." ASCE-ASME Journal of Risk and Uncertainty in Engineering Systems, Part A: Civil Engineering **3**(1): 04016013.

Gilbert, S. W. (2016). Disaster resilience: A guide to the literature, CreateSpace Independent Publishing Platrorm.

Golden, R. M. (1996). Mathematical methods for neural network analysis and design, MIT Press.

Gomes, H. M. and A. M. Awruch (2004). "Comparison of response surface and neural network with other methods for structural reliability analysis." Structural safety **26**(1): 49-67.

Hackmann, G., et al. (2014). "Cyber-physical codesign of distributed structural health monitoring with wireless sensor networks." IEEE Transactions on Parallel and Distributed Systems **25**(1): 63-72.

Hajela, P. and L. Berke (1991). "Neurobiological computational models in structural analysis and design." Computers & Structures **41**(4): 657-667.

Hochreiter, S. (1998). "The vanishing gradient problem during learning recurrent neural nets and problem solutions." International Journal of Uncertainty, Fuzziness and Knowledge-Based Systems **6**(02): 107-116.

Hochreiter, S. and J. Schmidhuber (1997). "Long short-term memory." Neural computation **9**(8): 1735-1780.

Holling, C. S. (1973). "Resilience and stability of ecological systems." Annual review of ecology and systematics **4**(1): 1-23.

Horiuchi, T., et al. (1996). Development of a real-time hybrid experimental system with actuator delay compensation. Proc. 11th World Conf. Earthquake Engineering.

Kafali, C. and M. Grigoriu (2005). Rehabilitation decision analysis. ICOSSAR'05, Proceedings of the 9th international conference on structural safety and reliability.

Kalathur, H., et al. (2014). "Buckling Mode Jump at Very Close Load Values in Unattached Flat-End Columns: Theory and Experiment." Journal of Applied Mechanics **81**(4): 041010.

Kang, H. T. and C. J. Yoon (1994). "Neural network approaches to aid simple truss design problems." Computer-Aided Civil and Infrastructure Engineering **9**(3): 211-218.

Keivan, A., et al. (2017). "Causal Realization of Rate-Independent Linear Damping for the Protection of Low-Frequency Structures." Journal of engineering mechanics **143**(9): 04017058.

Kelly, J. M. and D. Konstantinidis (2011). Mechanics of rubber bearings for seismic and vibration isolation, John Wiley & Sons.

Kennedy, J. (2006). Swarm intelligence. Handbook of nature-inspired and innovative computing, Springer**:** 187-219.

Kim, S. B., et al. (2005). "Frequency domain identification of multi-input, multi-output systems considering physical relationships between measured variables." Journal of engineering mechanics **131**(5): 461-472.

Kingma, D. P. and J. Ba (2014). "Adam: A method for stochastic optimization." arXiv preprint arXiv:1412.6980.

Krawinkler, H. (1995). New trends in seismic design methodology, EUROPEAN CONFERENCE ON EARTHQUAKE ENGINEERING.

Krawinkler, H. (2000). "State of the art report on systems performance of steel moment frames subject to earthquake ground shaking." Report no. FEMA-355C, SAC Joint Venture.

Kurama, Y., et al. (1999). "Lateral load behavior and seismic design of unbonded post-tensioned precast concrete walls." ACI Structural Journal **96**(4).

Lazar, N. and M. Dolsek (2012). Risk-based seismic design-An alternative to current standards for earthquake-resistant design of buildings. Proceedings of the 15th World Conference on Earthquake Engineering.

Liel, A. B., et al. (2009). "Incorporating modeling uncertainties in the assessment of seismic collapse risk of buildings." Structural safety **31**(2): 197-211.

Lin, M.-H., et al. (2012). "A review of deterministic optimization methods in engineering and management." Mathematical Problems in Engineering **2012**.

Lin, S.-L., et al. (2012). "NEES integrated seismic risk assessment framework (NISRAF)." Soil Dynamics and Earthquake Engineering **42**: 219-228.

Lipton, Z. C., et al. (2015). "A critical review of recurrent neural networks for sequence learning." arXiv preprint arXiv:1506.00019.

Luenberger, D. G. and Y. Ye (1984). Linear and nonlinear programming, Springer.

Mahin, S., et al. (2006). Use of partially prestressed reinforced concrete columns to reduce post-earthquake residual displacements of bridges. Fifth National Seismic Conference on Bridges & Highways, San Francisco, California.

Malangone, P. and M. Ferraioli (1998). "A modal procedure for seismic analysis of non - linear base - isolated multistorey structures." Earthquake Engineering & Structural Dynamics **27**(4): 397-412.

Malek, K. A. and K. Basir (2001). "Design and characteristics of high damping natural rubber bearings for base isolation." WIT Transactions on The Built Environment **57**.

Mander, J. B., et al. (2007). "Incremental dynamic analysis applied to seismic financial risk assessment of bridges." Engineering Structures **29**(10): 2662-2672.

McAslan, A. (2010). "The concept of resilience: Understanding its origins, meaning and utility." Adelaide: Torrens Resilience Institute.

Mehrotra, K., et al. (1997). Elements of artificial neural networks, MIT press.

Microsoft Microsoft Visual C++. Redmond, WA.

Mitropoulou, C. C. and M. Papadrakakis (2011). "Developing fragility curves based on neural network IDA predictions." Engineering Structures **33**(12): 3409-3421.

MRl, H. (2003). "Multi-hazard loss estimation methodology: Earthquake model." Department of Homeland Security, FEMA, Washington, DC.

Olsson, A., et al. (2003). "On Latin hypercube sampling for structural reliability analysis." Structural safety **25**(1): 47-68.

Padgett, J. E., et al. (2010). "Risk-based seismic life-cycle cost–benefit (LCC-B) analysis for bridge retrofit assessment." Structural safety **32**(3): 165-173.

Pampanin, S., et al. (2003). "Performance-based seismic response of frame structures including residual deformations part II: multi-degree of freedom systems." Journal of Earthquake Engineering **7**(01): 119-147.

Papadrakakis, M., et al. (1998). "Structural optimization using evolution strategies and neural networks." Computer methods in applied mechanics and engineering **156**(1-4): 309-333.

Pascanu, R., et al. (2013). On the difficulty of training recurrent neural networks. International Conference on Machine Learning.

Phillips, B. M., et al. (2010). "Real-time hybrid simulation benchmark study with a large-scale MR damper." Proc. of the 5th WCSCM: 12-14.

Phillips, B. M. and B. F. Spencer Jr (2012). "Model-based feedforward-feedback actuator control for real-time hybrid simulation." Journal of Structural Engineering **139**(7): 1205-1214.

Phillips, B. M., et al. (2014). "Feedforward actuator controller development using the backward-difference method for real-time hybrid simulation." Smart Structures and Systems **14**(6): 1081-1103.

Phoon, K.-K., et al. (2003). "Development of a reliability-based design framework for transmission line structure foundations." Journal of Geotechnical and Geoenvironmental Engineering **129**(9): 798-806.

Porter, K. (2015). "Beginner's guide to fragility, vulnerability, and risk." Encyclopedia of Earthquake Engineering: 235-260.

Porter, K., et al. (2005). "Propagation of uncertainties from IM to DV." Van Nuys Hotel Building Testbed report: Exercising seismic performance assessment. Pacific Earthquake Engineering Research Center (PEER 2005/11).

Porter, K., et al. (2007). "Creating fragility functions for performance-based earthquake engineering." Earthquake spectra **23**(2): 471-489.

Prager, W. and G. I. Rozvany (1977). Optimization of structural geometry. Dynamical systems, Elsevier**:** 265-293.

Rajkumar, R. R., et al. (2010). Cyber-physical systems: the next computing revolution. Proceedings of the 47th design automation conference, ACM.

Ramirez, C. M. and E. Miranda (2012). "Significance of residual drifts in building earthquake loss estimation." Earthquake Engineering & Structural Dynamics **41**(11): 1477-1493.

Razi, M. A. and K. Athappilly (2005). "A comparative predictive analysis of neural networks (NNs), nonlinear regression and classification and regression tree (CART) models." Expert Systems with Applications **29**(1): 65-74.

Ricles, J. M., et al. (2001). "Posttensioned seismic-resistant connections for steel frames." Journal of Structural Engineering **127**(2): 113-121.

Rogers, J. L. (1994). "Simulating structural analysis with neural network." Journal of Computing in Civil Engineering **8**(2): 252-265.

Roh, H. and A. M. Reinhorn (2010). "Modeling and seismic response of structures with concrete rocking columns and viscous dampers." Engineering Structures **32**(8): 2096-2107.

Rojas, H. A., et al. (2011). "Risk-based seismic design for optimal structural and nonstructural system performance." Earthquake spectra **27**(3): 857-880.

Rozvany, G. (1972). "Grillages of maximum strength and maximum stiffness." International Journal of Mechanical Sciences **14**(10): 651-666.

Sabelli, R. (2001). Research on improving the design and analysis of earthquake-resistant steel-braced frames, EERI.

Sabelli, R., et al. (2003). "Seismic demands on steel braced frame buildings with buckling-restrained braces." Engineering Structures **25**(5): 655-666.

Saka, M. (2007). "Optimum design of steel frames using stochastic search techniques based on natural phenomena: a review." Civil engineering computations: tools and techniques **6**: 105-147.

Sawyer, H. (1964). "Comprehensive design of reinforced concrete frames by plasticity factors." Bull. d'Inform. CEB(53): 299-316.

Shi, Y. and R. Eberhart (1998). A modified particle swarm optimizer. Evolutionary Computation Proceedings, 1998. IEEE World Congress on Computational Intelligence., The 1998 IEEE International Conference on, IEEE.

Shing, P. B., et al. (1996). "Application of pseudodynamic test method to structural research." Earthquake spectra **12**(1): 29-56.

Shinozuka, M., et al. (2000). "Nonlinear static procedure for fragility curve development." Journal of engineering mechanics **126**(12): 1287-1295.

Shinozuka, M., et al. (2000). "Statistical analysis of fragility curves." Journal of engineering mechanics **126**(12): 1224-1231.

Sinković, N. L., et al. (2016). "Risk - based seismic design for collapse safety." Earthquake Engineering & Structural Dynamics **45**(9): 1451-1471.

Somerville, P. G. (1997). Development of ground motion time histories for phase 2 of the FEMA/SAC steel project, SAC Joint Venture.

Somerville, P. G. and S. J. Venture (1997). Development of ground motion time histories for phase 2 of the FEMA/SAC steel project, SAC Joint Venture.

Song, W. and S. Dyke (2013). "Development of a cyber-physical experimental platform for real-time dynamic model updating." Mechanical Systems and Signal Processing **37**(1-2): 388-402.

Spencer Jr, B., et al. (1997). "Phenomenological model for magnetorheological dampers." Journal of engineering mechanics **123**(3): 230-238.

Tassios, T. (1999). The seismic design: State of practice. Earthquake Engineering-Invited Papers: Proceedings of the eleventh European conference, Paris, France, 6-11 September 1998, CRC Press.

The MathWorks, I. MATLAB. Natick, MA.

Timoshenko, S. P. and J. M. Gere (1961). "Theory of elastic stability. 1961." McGrawHill-Kogakusha Ltd, Tokyo.

Tirca, L., et al. (2015). "Improving the seismic resilience of existing braced-frame office buildings." Journal of Structural Engineering **142**(8): C4015003.

Tremblay, R., et al. (2008). "Seismic response of multistory buildings with self-centering energy dissipative steel braces." Journal of Structural Engineering **134**(1): 108-120.

USGS (2014). Unified Hazard Tool, United States Geological Survey. **Earthquake Hazards Program**.

Valdebenito, M. A. and G. I. Schuëller (2010). "A survey on approaches for reliability-based optimization." Structural and Multidisciplinary Optimization **42**(5): 645-663.

Vamvatsikos, D. and C. A. Cornell (2002). "Incremental dynamic analysis." Earthquake Engineering & Structural Dynamics **31**(3): 491-514.

Vanderplaats, G. N. and H. Sugimoto (1986). "A general-purpose optimization program for engineering design." Computers & Structures **24**(1): 13-21.

Wang, D.-H. and W.-H. Liao (2001). Neural network modeling and controllers for magnetorheological fluid dampers. Fuzzy Systems, 2001. The 10th IEEE International Conference on, IEEE.

Wang, D. and W. Liao (2004). "Modeling and control of magnetorheological fluid dampers using neural networks." Smart materials and structures **14**(1): 111.

Warner, B. and M. Misra (1996). "Understanding neural networks as statistical tools." The american statistician **50**(4): 284-293.

Wen, Y. (2001). "Reliability and performance-based design." Structural safety **23**(4): 407-428.

Zapateiro, M., et al. (2010). "Real-time hybrid testing of semiactive control strategies for vibration reduction in a structure with MR damper." Structural Control and Health Monitoring **17**(4): 427-451.

Zaremba, W., et al. (2014). "Recurrent neural network regularization." arXiv preprint arXiv:1409.2329.

Zentner, I., et al. (2017). "Fragility analysis methods: Review of existing approaches and application." Nuclear Engineering and Design **323**: 245-258.

Zhang, J. and Y. Huo (2009). "Evaluating effectiveness and optimum design of isolation devices for highway bridges using the fragility function method." Engineering Structures **31**(8): 1648-1660.

Zhou, F. L., et al. (2004). New seismic isolation system for irregular structure with the largest isolaton building area in the world. 13th World Conference on Earthquake Engineering.

Zhu, S. and Y. Zhang (2007). "Seismic behaviour of self-centring braced frame buildings with reusable hysteretic damping brace." Earthquake engineering & structural dynamics **36**(10): 1329-1346.

Zhu, S. and Y. Zhang (2008). "Seismic analysis of concentrically braced frame systems with self-centering friction damping braces." Journal of Structural Engineering **134**(1): 121-131.

Zou, X.-K., et al. (2010). "Integrated reliability-based seismic drift design optimization of base-isolated concrete buildings." Journal of Structural Engineering **136**(10): 1282-1295.